UNIVERSITÄT PADERBORN
Die Universität der Informationsgesellschaft

DLR Deutsches Zentrum für Luft- und Raumfahrt
German Aerospace Center

Master Thesis

Analysis of temperature measurements on solar absorber coatings under concentrated solar flux

by

LARS BENEDIKT KRUSE

Course of studies: Mechanical engineering

Matriculation number: 7054156

submitted to

Paderborn University

First examiner: PROF. DR. HANS-JOACHIM SCHMID
Second examiner: DR. GERHARD HERRES

in cooperation with

DLR Institute of Solar Reasearch

Supervisor: DIPL.-ING. SIMON CARON

Paderborn, 02.05.2019

Declaration

I declare that I have authored this thesis independently, that I have not used other than the declared sources, and that I have explicitly indicated all material which has been quoted either literally or by content from the sources used.

Date	Signature

Contents

Nomenclature

Variable	Unit	Description
A	m^2	Area
Ab	W	Absorptance (absorbed radiation flux)
b	m	Detector length
C	$Jkg^{-1}K^{-1}$	Capacity
d	m	Detector to aperture distance
D	m	Object distance
E	J	Energy
Em	W	Emittance (emitted radiation flux)
f	s^{-1},m	Frequency, focal length
FOV	rad	Field of view
I	sr	Radiant intensity
J	Wm^{-2}	Irradiance
l	m	Length
L	$Wm^{-2}sr^{-1}$	Radiance
M	Wm^{-2}	Exitance
r	m	Radius
R	m	Roughness
Res		Response function of TMD
s		sensitivity
S		Signal
SSE		Size of source factor
T	K	Temperature
x	m	Object length, spatial coordinate
X	m	equivalent radiation source diameter at $D = 2.4\,m$
y, z	m	spatial coordinate

Greek variable	Unit	Description
α		absorptivity
β	rad	angle of refraction
δ	rad	Altitude angle
ϕ	rad	Azimuth angle
ε		emissivity
λ	m	Wavelength
ρ		reflectivity
τ		transmissivity
Φ	W	energy flux
ψ		Weighting factor of samples area to ceramic area
ζ		concentration factor
Ω	rad	solid angle

Abbreviations	Unit	Description
BP		BandPass
DNI		Direct Normal Irradiance
EXP		Exponent
FPA		Focal Plane Array
FTS		Fourier Transform Spectroscopy
HIFOV		Horizontal Instantaneous Field Of View
IR		InfraRed
LP		Long-Pass
RMSE		Root mean Squared Error
RH		Relative Humidity
NBP		Narrow BandPass
SH Pl		Sakuma-Hattori Planck
SP		Short-Pass
SSE		Size of Source Effect
TC		Thermocouple
TMD		Thermographic Measurement Device
VIFOV		Vertical Instantaneous Field Of View

Constant	Unit	Description
A, B, C, D		Parameters for calibration curve fitting
$A_B L$, $B_B L$, $C_B L$, $D_B L$		Parameters for SSE fitting (Bloemberg fit)
$b = 2.89777 \cdot 10^{-3}$	mK	Wien's displacement constant
c	ms^{-1}	Speed of light
$h = 6.62607 \cdot 10^{-34}$	Js	Planck constant
$k = 1.38065 \cdot 10^{-23}$	JK^{-1}	Boltzmann constant
n		Index of refraction
$\sigma = 5.67037 \cdot 10^{-8}$	$Wm^{-2}K^{-4}$	Stefan-Boltzmann constant

Subscript

a	Surface
atm	Atmosphere
A	Absorbed
Apt	Aperture
BB	Blackbody
det	Detector
E	Enclosure
f	Filter, focused
fit	fitted
I	Incident
IRcam	Infrared camera
l	Lens
meas	measured
min	Minimum
max	Maximum
O	Output
obj	Object
proc	electronic processing
sun	Sun and ambiance
ref	Reference
R, refl	Reflected
T	Transmitted
th	Thermal
W	Window
λ	m^{-1} Spectral unit (multiply with original unit)

List of Figures

List of Tables

1. Introduction

The worldwide population and economic growth is accompanied with a rise of energy consumption. Until 2030 an annual increase in energy consumption of 1.7 % is predicted in the World Energy Outlook of the International Energy Agency [1]. Currently the main energy source are fossil fuels, with 79.5 % in 2016 [2]. Due to their emission of greenhouse gases leading to climate changes and limited availability, other energy sources have to be reinforced. To estimate the competitiveness of different energy sources, the levelized cost of energy (LCOE) parameter describes the average total cost of a facility related to its average total energy output. Therefore, the LCOE of other energy sources has to be decreased to meet LCOE of fossil fuels, such as gas with 41...74$(MWh)^{-1}$ and coal with 60...143$(MWh)^{-1}$ [3]. While the nuclear power generation includes great risks, most promising are renewable energies.
Their emission of greenhouse gases is reduced to the manufacturing of the facilities and their energy sources are unlimited on a human scale. However without energy storage, their availability can be very volatile, since it depends on the respective energy source. Besides wind and hydro, solar energies represent a major part among the renewable energies. Mostly spread and developed among them are photovoltaic systems, generating electricity directly from incident sun radiation. Here photovoltaic systems based on crystalline silicon have an LCOE of 73...145 $(MWh)^{-1}$ [3]. Less developed are the concentrated solar power (CSP) systems. They include a double energy conversion. First the solar irradiance is collected by mirrors and converted into heat. The heat is then converted in a steam turbine cycle into electricity. A great benefit compared to other renewable energies is, that CSP systems include a heat energy storage. Depending on its size and the operating region, this storage can compensate the volatile circumstances. The operating region depends mainly on the availability of direct normal irradiance (DNI), which is shown in figure 1.1 at the world map. CSP systems vary in their complexity of mirror area and sun tracking and therefore reach different working fluid temperatures in the steam turbine cycle. From the carnot efficiency $\eta_{\text{carnot}} = 1 - \frac{T_C}{T_H}$, higher working fluid temperatures are advantageous for the steam turbine cycle.
Among CSP systems, solar power tower yield the highest efficiencies of up to 23...35 %, with current working fluid temperatures of about 600 °C [5]. While

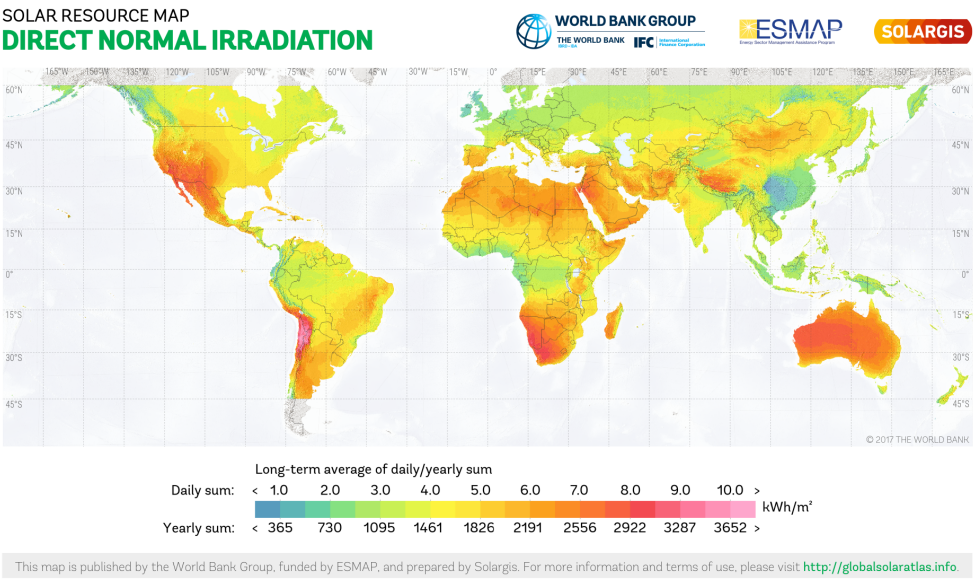

Figure 1.1.: World map showing the direct normal irradiance (DNI). Taken from [4]

on the one side, a lot of research is invested to reach higher temperatures [6], the cost and benefit for the LCOE has to be considered on the other side. A great part of the total solar power tower LCOE with 98...181$(\mathrm{MWh})^{-1}$ is related to the costs of solar receiver and their coatings, converting the concentrated sunlight into heat [5], [3]. Since various aspects, such as absorptivity, emissivity, degradation and reapplication effect the receiver coatings, the levelized cost of coating (LCOC) was introduced to compare different coatings [7]. To reduce this LCOC, one part of the RAISELIFE project aims to increase the coatings lifetime [8]. Therefore researches are carried out with accelerated aging campaigns [9]. In this context the following work concerns with the infrared temperature measurement of receiver coatings, which is essential in numerous aspects. From an industrial point of view, the optimal temperature has to be regulated and monitored, to increase the efficiency, while preventing an overheating of the receiver. For the related research campaign, knowledge about the temperature is furthermore necessary to investigate and compare the durabilities of the receiver coatings. This work is divided into the following four chapters. The chapter 2 (Infrared thermography), concerns theoretical aspects of radiation and infrared measurement. The next chapter 3 (Methodology), defines the boundary conditions of the measurement setup and applies the theoretical findings. The chapter 4 (Results and Discussions) gives the findings of the measurements and discusses its validity. The last chapter 5 (Conclusion) summarizes the whole work and shows potentials of improvement.

2. Infrared Thermography

This chapter covers some theoretical aspects of infrared thermography, based on the books [10]–[12]. Due to the vast amount of theory and applications, this chapter constrains to the infrared thermography principles, relevant for the current work. The first section 2.1 cover the physical radiation principles, while the second section 2.2 describes the principles of radiation measurement.

2.1. Physical radiation principles

The acceleration of charged particles, such as protons and electrons result in an emission of photons, whereas a photon is a zero mass particle with an energy E. These photons can also be described as electromagnetic waves, calculated by the Maxwell equations [13]. Since these waves are based on electromagnetic processes, their movement is not dependent on molecules and their velocity is the speed of light c. Electromagnetic waves are classified by their wavelength λ or frequency f, with

$$f = \mathrm{c}/\lambda. \tag{2.1}$$

The frequency, resp. wavelength intervals with the corresponding names are shown in figure 2.1. Herein the visible spectrum stretches from 770 to 430 THz (380 to 780 nm), with the infrared spectrum extending to smaller frequencies from 430 THz to 430 GHz (780 nm to 1 mm).
The radiated energy E of a photon depends linearly on its frequency f and can be described by the Planck–Einstein relation [14]

$$E = \mathrm{h}f, \tag{2.2}$$

with h being the Planck constant. Electromagnetic waves of a higher frequency therefore radiate more energy, than electromagnetic waves of a smaller frequency.

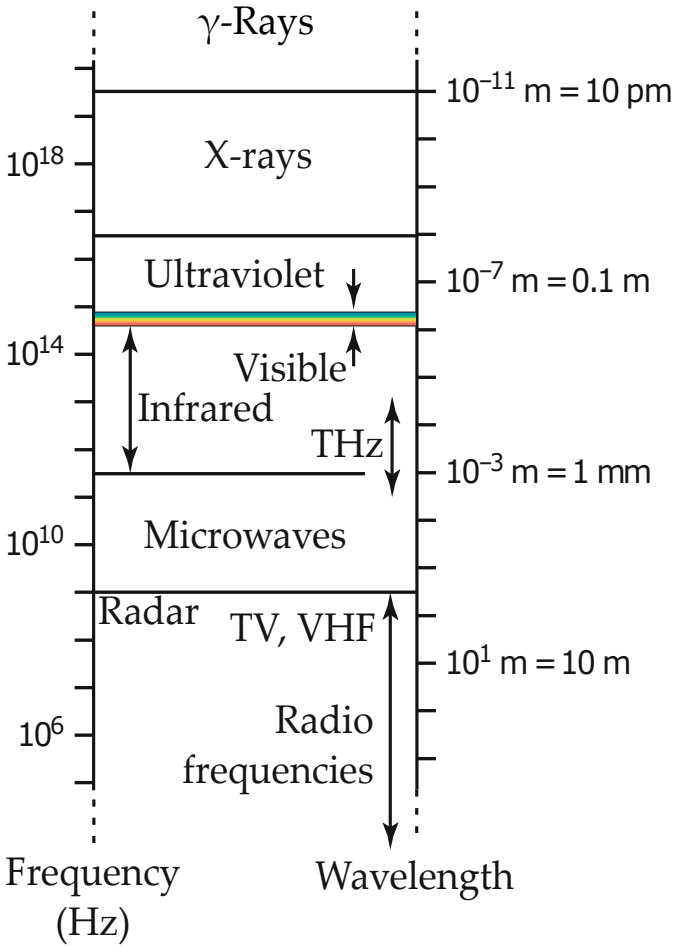

Figure 2.1.: Electromagnetic spectrum over frequency (left vertical axis) and wavelength (right vertical axis), taken from [10].

2.1.1. Geometric radiation quantities

Every body with a temperature T greater than 0 K contains accelerated charged particles and thus emits electromagnetic waves.
The radiation of a body with surface element dA is composed of various electromagnetic waves of different wavelengths. Their combined energy emitting of the surface dA is the total energy flux dΦ with the unit W.
The spectral density of the energy flux is expressed as

$$\Phi_\lambda = \mathrm{d}\Phi/\mathrm{d}\lambda, \tag{2.3}$$

with

$$\Phi = \int_0^\infty \Phi_\lambda \mathrm{d}\lambda. \tag{2.4}$$

Relating the energy flux to the emitting surface element $\mathrm{d}A$ yields the exitance

$$M = \mathrm{d}\Phi/\mathrm{d}A, \tag{2.5}$$

with the unit Wm^{-2}. Respectively the spectral exitance is calculated as

$$M_\lambda = \mathrm{d}M/\mathrm{d}\lambda, \tag{2.6}$$

with the unit $\mathrm{Wm}^{-2}\mathrm{m}^{-1}$. The Irradiance J, defined as the energy flux per irradiated surface element is defined analog.
In practice the radiation is often assumed to be independent on its angle of emission. This theoretical body, radiating isotropic into the hemisphere, is called a a Lambertian radiator.
To describe an angle dependent radiating surface, the radiant intensity

$$I = \mathrm{d}\Phi/\mathrm{d}\Omega, \tag{2.7}$$

is defined as shown in figure 2.2. $\Omega(\delta, \varphi)$ is the solid angle constituting the perpendicular surface $\mathrm{d}A_2$ in polar representation, with the unit sr (steradian).
Since only the perpendicular projected part of the emitting surface contributes

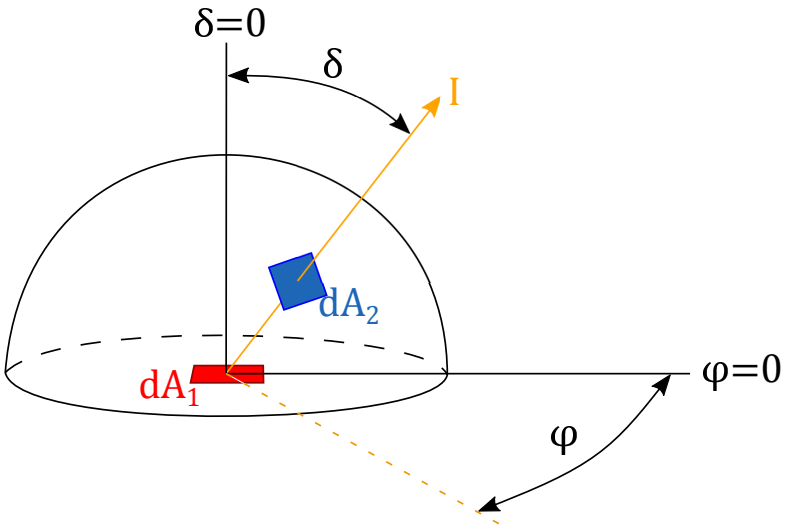

Figure 2.2.: Propagation of radiant intensity I into the hemisphere. Exemplary shown for a radiating surface element $\mathrm{d}A_1$ and hemisphere element $\mathrm{d}A_2$. Based on [11].

to the emitted radiation, the radiant intensity decreases along greater angles of δ, shown in figure 2.3 for a Lambertian radiator.
Relating the radiant intensity to the perpendicular projected part $\mathrm{d}A_1\cos(\delta)$ of

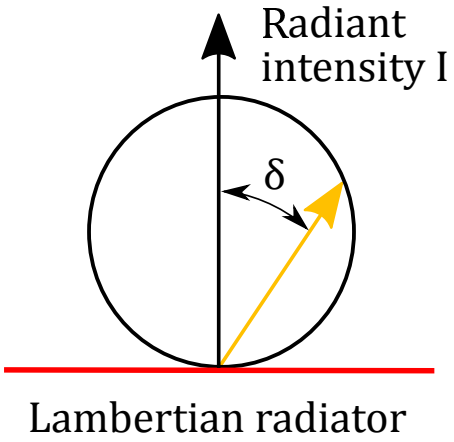

Figure 2.3.: Altitude δ dependence of radiant intensity I of a Lambertian radiator. Edited from [10].

the area $\mathrm{d}A_1$ gives the radiance

$$L = \frac{d^2\Phi}{\cos(\delta)\,\mathrm{d}A_1\,\mathrm{d}\Omega}\,, \tag{2.8}$$

with the unit $\mathrm{Wm^{-2}sr^{-1}}$. A representation is shown in figure 2.4.

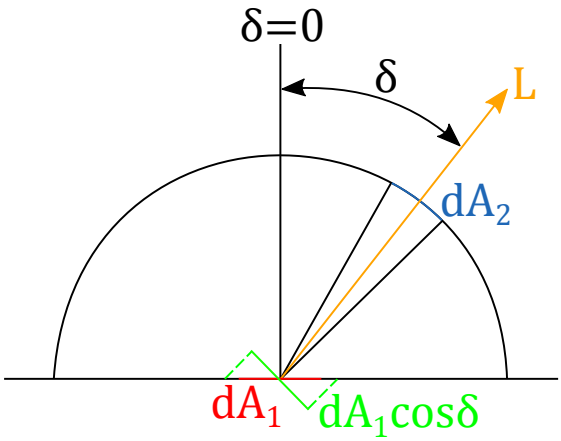

Figure 2.4.: Propagation of radiance L into the hemisphere. Exemplary shown for a radiating surface element $\mathrm{d}A_1$, resp. orthogonal radiating surface element $\mathrm{d}A_1 cos\delta$ and hemisphere element $\mathrm{d}A_2$. Based on [11].

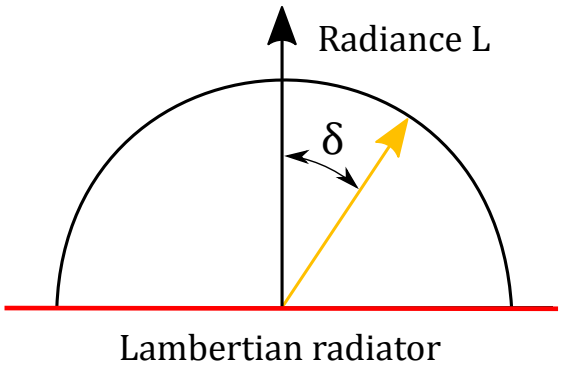

Figure 2.5.: Altitude δ independence of radiance L of a Lambertian radiator. Edited from [10].

Regarding the radiance, the truly uniform radiation of the Lambertian radiator is shown in figure 2.5.
Due to the angle independence of the Lambertian radiator, its exitance can be calculated as

$$M = L\pi. \tag{2.9}$$

2.1.2. Inverse-square law

The influence of measurement distance to the radiating body is explained in the following and illustrated in figure 2.6.
Considering the surface element $\mathrm{d}A_1$ emits an amount of energy into the hemisphere, then this amount will be constant along increasing hemisphere radii r, whereas the surface of the hemisphere is increasing. The result is a quadratical ($A_{\mathrm{hem}} = 2\pi r^2$) decreasing energy per hemisphere area.
Therefore, radiometric quantities are formulated in terms of constant angle $\Omega(\delta, \varphi) = A_2'/r'^2$. For the example in figure 2.6, the increase of the hemisphere area $\mathrm{d}A_2'$ compared to $\mathrm{d}A_2$ then cancels out with the increase of radius r' compared to r.
The energy flux Φ onto the perpendicular surface element $\mathrm{d}A_2'$ is then

$$\mathrm{d}^2\Phi = \frac{L_1 \cos(\delta_1)\, \mathrm{d}A_1\, \mathrm{d}A_2'}{r'^2}. \tag{2.10}$$

Along the distance r, the quadratically decreasing radiance L_1/r'^2 in equation 2.10, therefore cancels out with the quadratically increasing area $\mathrm{d}A_2'$, resulting in the same energy flux $\mathrm{d}\Phi$.

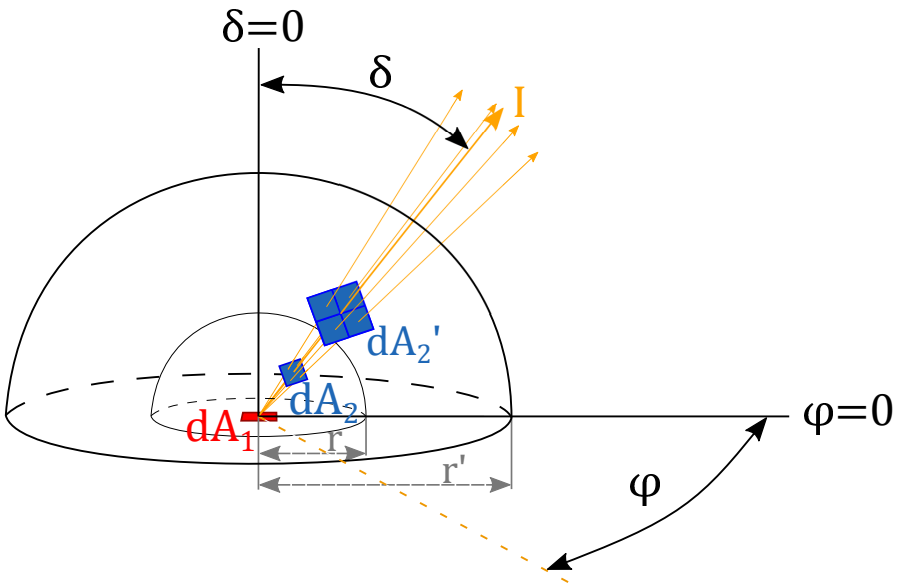

Figure 2.6.: Propagation of radiant intensity I into the hemisphere. Exemplary shown for a radiating surface element $\mathrm{d}A_1$, hemisphere element $\mathrm{d}A_2$ at distance r and hemisphere element $\mathrm{d}A_2'$ at distance r'.

2.1.3. Propagation of radiation

The propagation of visible light and infrared radiation in a medium or at the boundary between two media can be described by geometrical optics. Exemplary shown in figure 2.7, it is stated that:

- In a homogeneous medium the radiation propagates as rays along straight lines. Its velocity is dependent on the medium.
- When incident on a interface between two media, the radiation splits in two parts: A reflected and a transmitted part.
- The reflected part spans the same angle β_1' to the perpendicular of the reflecting surface as the incident ray β_1.
- The transmitted part is refracted at an angle β_2, described by the Snell's law of refraction, which states that

$$\mathrm{n}_1 \sin(\beta_1) = \mathrm{n}_2 \sin(\beta_2). \tag{2.11}$$

  n_1 and n_2 are the index of refraction, dependent on the velocity of radiation in that medium.
- A medium absorbs a part of the incident radiation, described by the absorptance Ab.

When applying energy conservation, it is evident that any radiation Φ_0 incident on a body can be divided into a reflected part Φ_R, a transmitted part Φ_T and an absorbed part Φ_A

$$\Phi_0 = \Phi_R + \Phi_T + \Phi_A. \tag{2.12}$$

Dividing the equation by the incident radiation Φ_0 yields

$$1 = \rho + \tau + \alpha, \tag{2.13}$$

where the reflectivity ρ, transmittivity τ and absorptivity α are the fractions of reflection, transmission and absorption by the incident radiation.

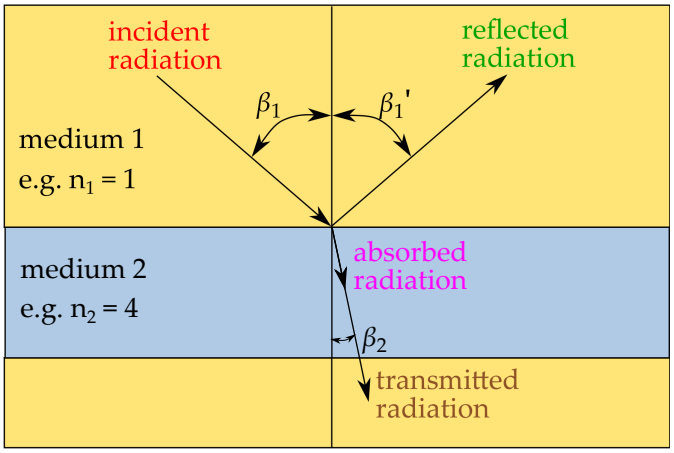

Figure 2.7.: Reflected, absorbed and transmitted propagation of radiation in a medium or at the boundary between two media.

2.1.4. Ideal bodies

In a thermodynamic equilibrium of a body with its surrounding, energy conservation yields that the amount of this body's own radiation Φ_{Em} is the same as the absorbed amount Φ_{Ab} of incident radiation [15]

$$\Phi_{\mathrm{Ab}} = \Phi_{\mathrm{Em}} \tag{2.14}$$

and therefore:

$$\alpha = \varepsilon. \tag{2.15}$$

The radiation balance of any body can then also be written from equation 2.13 and 2.15 as

$$1 = \rho + \tau + \varepsilon, \tag{2.16}$$

with the reflectivity ρ, transmissivity τ and emissivity ε. For opaque bodies, with $\tau = 0$, equation 2.16 yields

$$\varepsilon = 1 - \rho. \tag{2.17}$$

Accordingly, for transparent bodies, with $\rho = 0$

$$\varepsilon = 1 - \tau \tag{2.18}$$

applies. Another idealization is the blackbody, absorbing all incident radiation, i.e. $\tau = 0$ and $\rho = 0$. Equation 2.15 and 2.16 yield then

$$\alpha = \varepsilon = 1. \tag{2.19}$$

The blackbody therefore absorbs and emits at the maximum.

2.1.5. Planck's law

In experiments with cavity radiators, which are quasi blackbody radiators, Planck identified a formula for the spectral exitance of blackbodies [16]

$$M_\lambda(T_{BB})\mathrm{d}\lambda = \frac{2\pi hc^2}{\lambda^5(e^{hc/(\lambda k T_{BB})} - 1)}\mathrm{d}\lambda, \tag{2.20}$$

with h being the Planck constant, c the speed of light, k the Boltzmann constant, λ the wavelength of the radiation and T_{BB} the temperature of the blackbody. The corresponding spectral exitance of varying temperatures is displayed over the wavelength in a linear coordinate system in figure 2.8a and in a logarithmic coordinate system in figure 2.8b. Their characteristic spectrum is described as following:

- The wavelength $\lambda(M_{max})$ of the spectrum's maximum follows Wien's displacement law
$$\lambda(M_{max}) = b/T_{BB}, \tag{2.21}$$
with Wien's displacement constant b. For increasing temperatures, the peak exitance moves towards shorter wavelengths.
- For small wavelengths $\lambda << \lambda(M_{max})$, the term $1/e^{hc/(\lambda k T_{BB})}$ is very small and reduces the spectral exitance towards zero.
- For long wavelengths $\lambda >> \lambda(M_{max})$, the term $1/\lambda^5$ is very small and reduces the spectral exitance towards zero.
- At a higher blackbody temperature, the spectral exitance for every wavelength is higher as well.

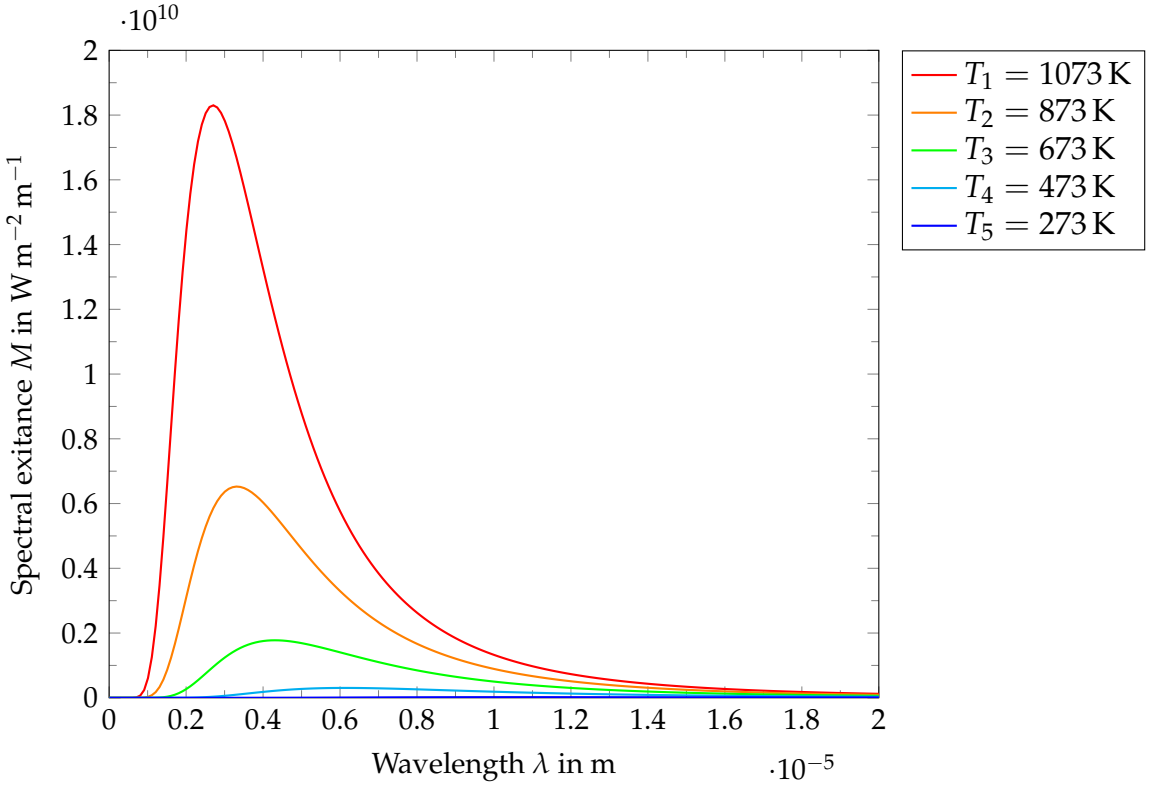

(a) Linear scaling of spectral exitance and wavelength.

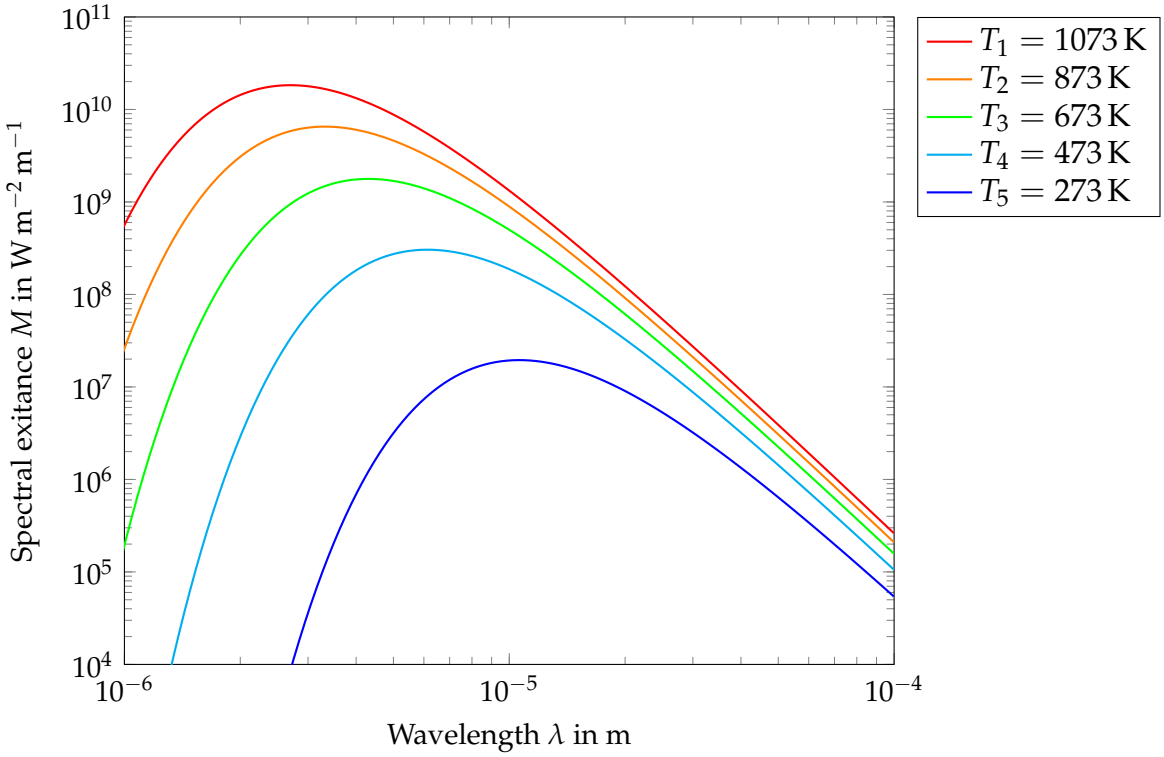

(b) Logarithmic scaling of spectral exitance and wavelength.

Figure 2.8.: Blackbody exitance as a function of wavelength and temperature.

Stefan-Boltzmann Law

Rearranging and integrating equation 2.6 gives the total exitance

$$M(T_{BB}) = \int M_\lambda(T_{BB})\mathrm{d}\lambda. \tag{2.22}$$

Since the total exitance is only dependent on the temperature of the blackbody, it is also called thermal radiation. Over the whole spectrum the Stefan-Boltzmann law

$$M(T_{BB}) = \int_{\lambda=0}^{\inf} M_\lambda(T_{BB})\mathrm{d}\lambda = \sigma T^4 \tag{2.23}$$

holds, with the Stefan-Boltzmann constant σ. In infrared measurements the wavelength spectrum is usually only partially detected ($\lambda_1 \ldots \lambda_2$). Integrating Planck's law (equation 2.20) in the boundaries λ_1 and λ_2 yields the band exitance

$$M(T_{BB}, \lambda_1, \lambda_2) = \int_{\lambda_1}^{\lambda_2} M_\lambda(T_{BB})\mathrm{d}\lambda = \int_{\lambda_1}^{\lambda_2} \frac{2\pi hc^2}{\lambda^5(e^{hc/(\lambda k T_{BB})} - 1)}\mathrm{d}\lambda, \tag{2.24}$$

which can not be solved analytically anymore. The applied numerical solution is explained in the following chapter for the particular wavelength band.

2.1.6. Characteristics of real objects

Some characteristics of real objects regarding their radiation are pointed out in the following. Afterwards the radiometric measurement chain with its components is described and modeled.

Emissivity

Since a theoretical formula of the maximum emitting blackbody was found by Planck, any other body is described related to it. The emissivity ε of any body is therefore expressed as the fraction of its emitted radiation to the radiation emitted by a blackbody at the same temperature T. This yields

$$\varepsilon(\lambda, \delta, \varphi, T, R_a, \text{Material}) = \frac{L(\lambda, \delta, \varphi, T, R_a, \text{Material})}{L_{BB}(T)}, \tag{2.25}$$

respectively

$$\varepsilon(\lambda, T, R_a, \text{Material}) = \frac{M(\lambda, T, R_a, \text{Material})}{M_{BB}(T)} \tag{2.26}$$

for the spectral radiance L and the spectral exitance M. The spectral radiance and thus the emissivity ε are here given to be dependent on the angles δ, ϕ, wavelength λ, temperature T, surface roughness R_a and Material. Therefore, in practice, special coatings, resp. paintings with known emissivity values for the temperatures and wavelengths to be examined are used.
Selective coatings are designed to absorb a specific band of wavelengths, i.e. their emissivity is wavelength dependent. A gray body on the contrary has a wavelength independent emissivity. A schematic course of the emissivity and the radiance over the Wavelength of a blackbody, grey body and selective emitter is shown in figure 2.9 and 2.10. The angle dependency of the emissivity results

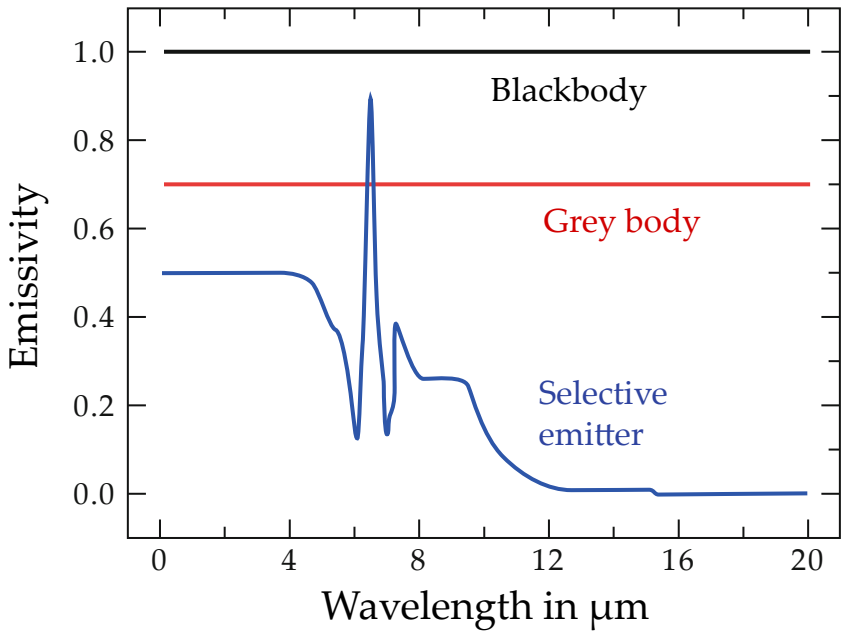

Figure 2.9.: Emissivity over wavelength of a blackbody, gray body and selective emitter. Taken from [10].

from the non lambertian emission of real bodies. Especially at big angles of observation the emitted radiance of a real body slopes significantly, shown in figure 2.11

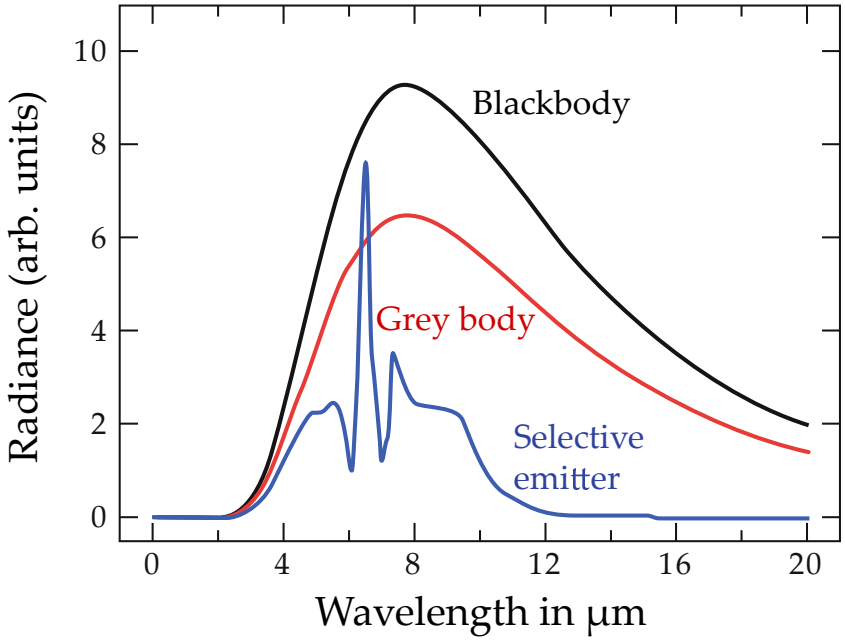

Figure 2.10.: Radiance over wavelength of a blackbody, gray body and selective emitter. Taken from [10].

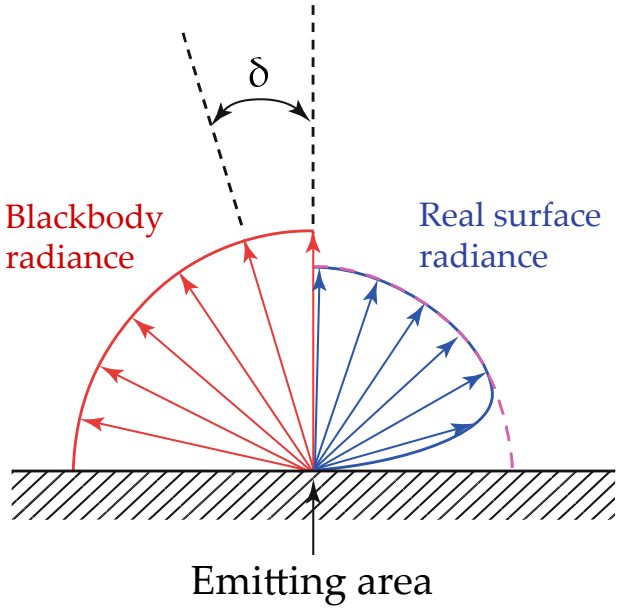

Figure 2.11.: Radiance dependence of emission angle for a blackbody (left) and real body (right). Taken from [10].

Reflectivity

When analyzing the reflection of radiation on a surface, the theoretical reflected ray holds only for very smooth surfaces. As presented in figure 2.12, increasing micro roughness R_a on the surface leads to higher scattering of the radiation. At some point the reflected ray will be dissolved and only diffuse scattered radiation will be existent.

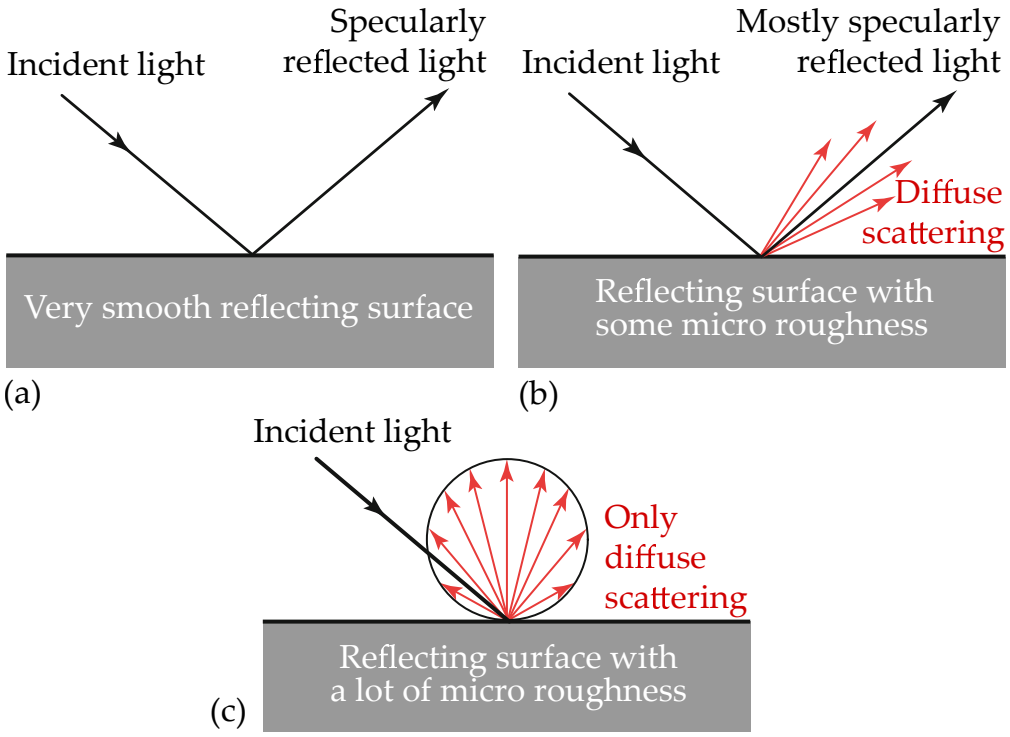

Figure 2.12.: Dependence of reflection on smooth reflecting surface (a), surface with some micro roughness (b) and surface with a lot of micro roughness (c). Taken from [10].

Transmissivity

The transmitted, resp. absorbed amount of radiation through a medium depends on its atomic structure. The molecules absorb the radiation only in specific wavelength bands, converting the radiation into molecular vibrations, which are furthermore temperature dependent. Various theoretical and empirical transmissivity models dependent on the substance, concentration and the temperature of the medium exist [17]–[19].

2.2. Radiation thermometer

The measurement of infrared radiation is described in the following for a radiation thermometer, with its measurement arrangement shown in figure 2.13. The

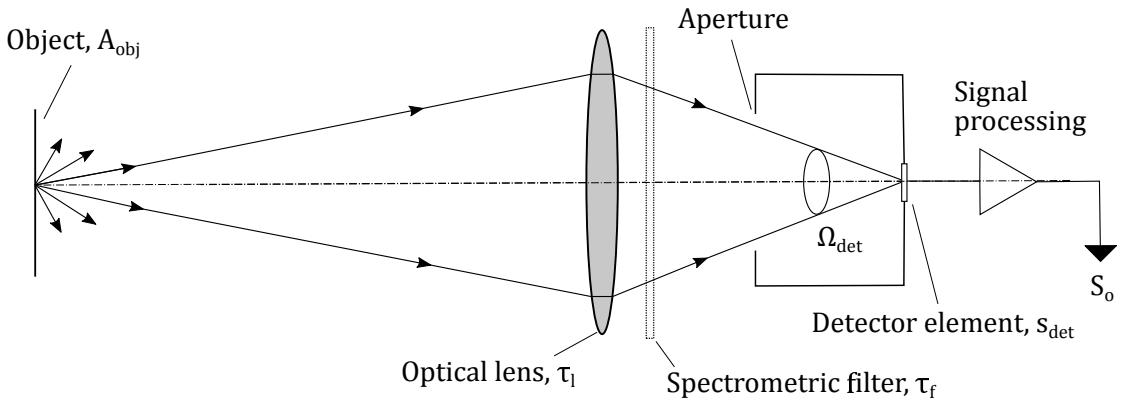

Figure 2.13.: Measurement arrangement of radiation thermometer. Based on [1]

incident radiation Φ_I from the object to be examined is focused by an optical lens and filtered by a spectral filter onto a radiometric detector element, where it is converted to a detector signal S_{det} and further processed to an output signal S_O. If the properties of lens, filter and detector are known, the incident radiation $\Phi_I(\lambda_f, T_{obj}, T_{amb}, \text{etc.})$ and thus the object temperature T_{obj} can be calculated from the output signal $S_O(\Phi_I(\lambda_f), \Phi_E)$. The incident radiation $\Phi_I(\lambda_f)$ is here dependent on the filtered wavelength spectrum λ_f and the detector signal is composed of an additional radiation from the detector element, resp. detector enclosure $\Phi_E(T_E)$ [20].

2.2.1. Optical lens

The optical lens focuses the incident radiation by refraction on the detector element, its principle is shown exemplary in figure 2.14. The field of view FOV is the angular range of the object, captured by the detector element. It can be calculated from the size of the detector b, resp. A_{det} and the focal length f as

$$\text{FOV} = 2 \arctan\left(\frac{b}{2f}\right), \tag{2.27}$$

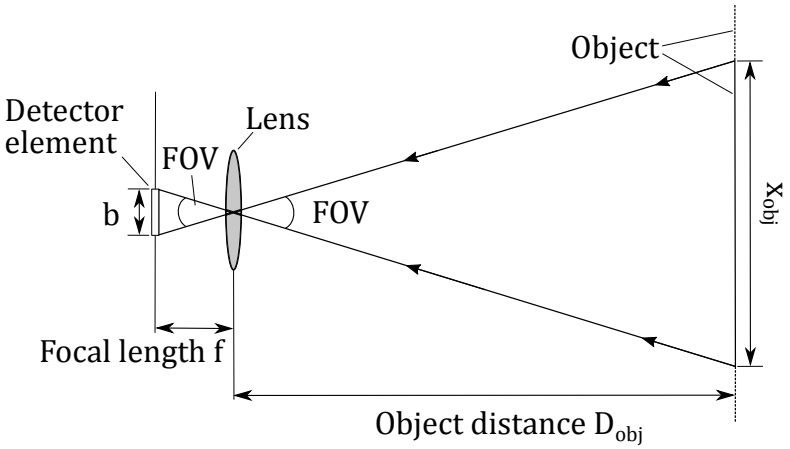

Figure 2.14.: Principle of an optical lens. Edited from [10]

or from the object distance D_{obj} and captured object length x_{obj} as

$$\mathrm{FOV} = 2 \arctan\left(\frac{x_{obj}}{2D_{obj}}\right). \tag{2.28}$$

According to the object distance D_{obj}, the focal length f can thus be adjusted to focus the object onto the detector element.

2.2.2. Filter

Since the radiometric properties are usually only known in a specific wavelength range, a reduction of the total radiation to this wavelength range by filters may be desired. The transmittance of various filters, subdivided into short-pass (SP), long-pass (LP), bandpass (BP) and narrow bandpass (NBP) filters are shown in figure 2.15. The width and transmittance of the filter depends on the optical properties of the particular filter material.

2.2.3. Infrared detector

Infrared detectors are the core part of an infrared camera, converting the incident radiation into an electric processible signal. Due to their sensitivity and to reduce error sources, they are isolated in an enclosure and receive radiation from the lens through an aperture. Infrared detectors can be distinguished between photon and thermal detectors.

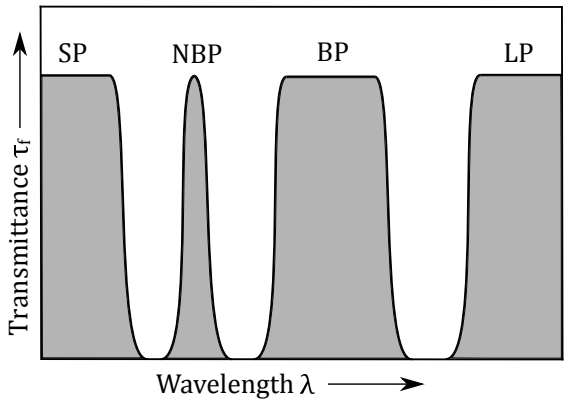

Figure 2.15.: Transmittance τ_f over wavelength λ of a short-pass (SP), long-pass (LP), bandpass (BP) and narrow bandpass (NBP) filter. Edited from [10].

Photon detectors use the photoelectric effect to convert the incident radiation directly into a change of an electric signal. Thermal detectors convert the incident radiation into heat, which changes the physical properties of the detector material and then measure the change of the physical property (e.g. electrical resistance). The spectral detector responsivity $s_{\mathrm{det},\lambda}$ is the relation of detector signal S_{det} to incident radiation $\Phi_{\mathrm{I},\lambda}$

$$s_{\mathrm{det},\lambda} = \frac{S_{\mathrm{det}}}{\Phi_{\mathrm{I},\lambda}}. \tag{2.29}$$

While the responsivity of photon detectors depend on their excitation wavelength of the electrons, the responsivity of a thermal detector is mostly dependent on the change of temperature and thus the detector material absorptivity α_{det} and thermal capacity $C_{\mathrm{th,det}}$ [21].

2.2.4. Radiometric correlation

From the prior considerations, the detector signal S_{det} and thereby the output signal S_{O} can be calculated in terms of the object radiance, respectively exitance as

$$S_{\mathrm{O}}(T_{\mathrm{obj}}) = c \int_{\lambda 1}^{\lambda 2} Res_{\lambda} L_{\lambda}(T_{\mathrm{obj}}) d\lambda \tag{2.30}$$

and

$$S_{\mathrm{O}}(T_{\mathrm{obj}}) = c \int_{\lambda 1}^{\lambda 2} Res_{\lambda} M_{\lambda}(T_{\mathrm{obj}}) d\lambda, \tag{2.31}$$

with the simplification of a homogeneous radiation over the solid angle Ω_{det} and detector area A_{det}, which are included in the constant c. Res_{λ} is the response of

the whole radiation thermometer, including the radiometric, spectral dependent properties of lens, filter and detector as well as the electronic signal processing c_{proc}

$$Res_{\lambda} = \tau_{l,\lambda} \cdot \tau_{f,\lambda} \cdot s_{\text{det},\lambda} \cdot c_{\text{proc}}. \tag{2.32}$$

Theoretically the detecting wavelength band would be $\lambda 1 = 0 \ldots \lambda 2 = \infty$. Practically it is reduced by the lens, filter and detector to a finite wavelength band $0 < \lambda 1 \ldots \lambda 2 < \infty$. The integral $\int_{\lambda 1}^{\lambda 2} M_{\lambda}(T) d\lambda$ is described by Planck's law for a blackbody in equation 2.24, for a finite wavelength band it can not be calculated analytically.
In theoretical approaches [10], [22], [23] various simplifications are described, such as utilizing a mean effective wavelength, to calculate equation 2.31.
An alternative empirical method replaces equation 2.31 with a least-square fitted expression $S_{\text{fit}}(T)$ at multiple measured temperature points. Various equations are existent in the literature to describe this expression $S_{\text{fit}}(T)$ for particular wavelength and temperature ranges [17], [24]–[28]. Most popular among them is the Sakuma-Hattori equation, here written in the Planck form [29] to resemble the Planck law (equation 2.20)

$$S(T) = C \cdot \left[\exp\left(\frac{c_2}{AT} \right) - 1 \right]^{-1}. \tag{2.33}$$

$c_2 = hc/k$ is Planck's second radiation constant, while A and C are the constants to be fitted, with C showing a λ^{-5} dependence [22]. Functions resembling the Planck equation are further called planckian. The applied functions with their characteristics are described in the methodology section 3.4.1.

2.2.5. Infrared thermometer calibration

Following the VDI-guidelines for radiation thermometry [20], the calibration of an infrared thermometer is preferably carried out with a blackbody radiator of $\varepsilon \approx 1$. For a short blackbody-infrared thermometer distance, the atmospheric transmissivity can also be assumed as $\tau \approx 1$. Temperatures of the blackbody radiator are set and the corresponding signal of the infrared thermometer is measured. For the measurement ranges $S_O(T_{BB,1})$ and $S_O(T_{BB,2})$ the calibrated infrared thermometer signal yields

$$S_O = \frac{S_O(T_{BB}) - S_O(T_{BB,1})}{S_O(T_{BB,2}) - S_O(T_{BB,1})}. \tag{2.34}$$

If there is a linear relationship between emitted radiation and the camera radiometric signal, i.e. Res_λ in equation 2.31 is not temperature dependent, then the output signal S_O can be written as a function of the exitance M:

$$S_O = \frac{M(\lambda, T_{BB}) - M(\lambda, T_{BB,1})}{M(\lambda, T_{BB,2}) - S(\lambda, T_{BB,1})}. \tag{2.35}$$

2.2.6. Practical effects

Additional effects occur, dependent on the practical implementation of the measurement arrangement. Most crucial upon them are the focus effect [30] and the size of source effect [31], [32].

Focus Effect

The focus effect is the result of an alternative positioning of the optical lens. Shown in figure 2.16, for a close focused object (dotted lines) and a far focused object (solid lines), the lens should be positioned between the aperture and the object.

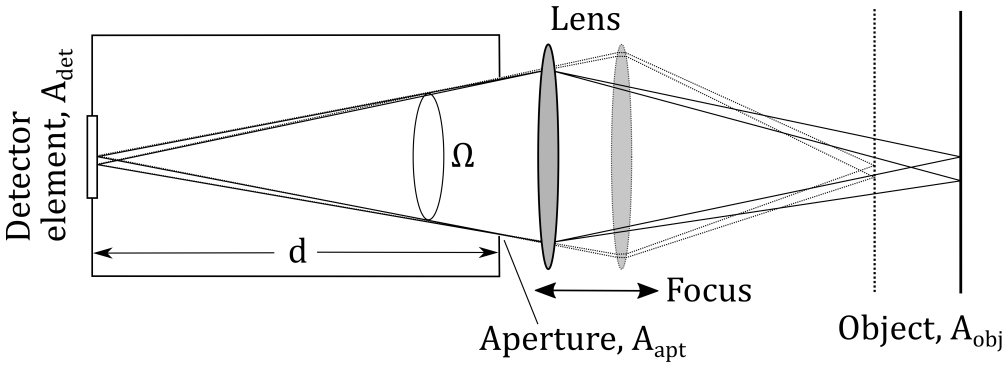

Figure 2.16.: Schematic radiation thermometer focused on a near object (dotted, transparent) and focused on a far object (solid). The solid angle Ω is constant over the focus range. Based on [33].

When the lens is shifted over the focus range, the solid angle Ω is constant, since the aperture diameter and the distance from the detector to the aperture are constant.
In an alternative setup, shown in figure 2.17, the lens is positioned between the

aperture and and the detector element. This setup is error-prone [33], since the solid angle Ω varies with the shifting of the lens over the focus range. Assuming an isotropic radiation over the solid angle Ω and homogeneous absorbing detector element area A, with a transparent lens, the perpendicular energy flux calculated with equation 2.8 yields

$$\Phi = LA_{\text{det}}\Omega = LA_{\text{det}}\frac{A_{\text{Apt}}}{d^2}, \tag{2.36}$$

with $\Omega \approx A_{\text{Apt}}/d^2$.
Thus a variation of the angle Ω results in a variation of the incident detector radiance, causing an erroneous temperature measurement.

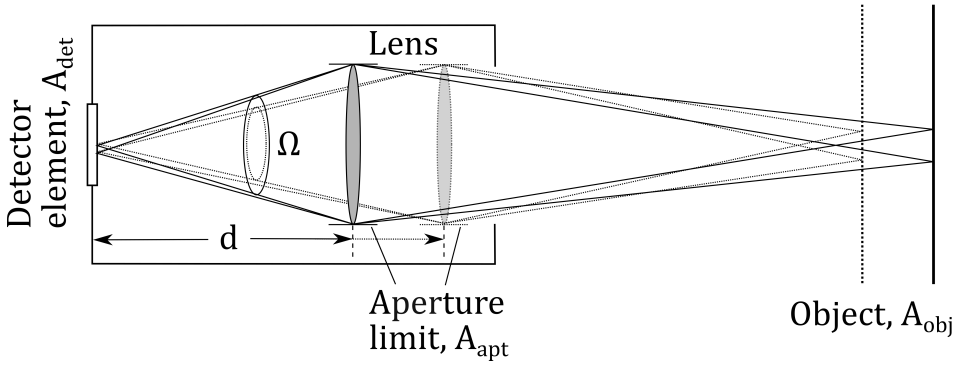

Figure 2.17.: Schematic alternative radiation thermometer focused on a near object (solid) and focused on a far object (dotted, transparent). The solid angle Ω varies over the focus range. Based on [33].

Size of Source effect

The size of source effect (SSE) results from various optical phenomena, such as diffraction, aberrations, refraction and scattering of the radiation in the measurement arrangement of the radiation thermometer [32].
These phenomena blur the radiometric image and cause a shading of the FOV boundary, shown in figure 2.18 in the angle range dFOV. Furthermore, particularly the scattering, causes the detector element to miss radiation from the FOV and detect radiation from outside of the FOV. The result is that the received radiation of the detector depends on the size and the ambient of the measured object.
Several recalibrations are described in the literature ([35]–[37]) to correct this SSE.

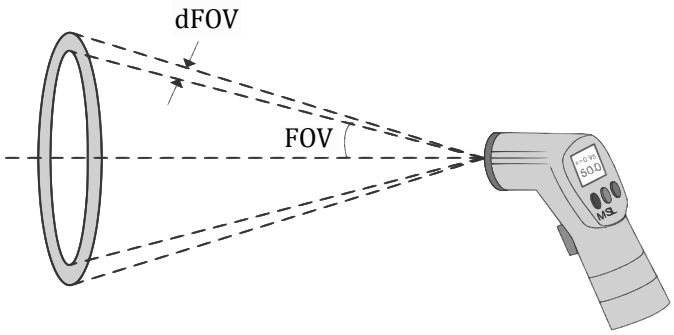

Figure 2.18.: Shade of SSE shown in an angle range dFOV at the boundary of the FOV. Edited from [34].

Furthermore particular lenses and a minimization of the optical imperfections can reduce the amount of the SSE [38].

2.2.7. Infrared camera

In contrast to infrared thermometers, infrared cameras resolve a spatial temperature image. They are distinguished between scanning and staring systems, both are shown in figure 2.19.
Scanning systems build up the infrared image sequentially by scanning the object with a single detector element. Staring systems on the contrary use numerous detector elements arranged to a focal plane array (FPA). Each detector element

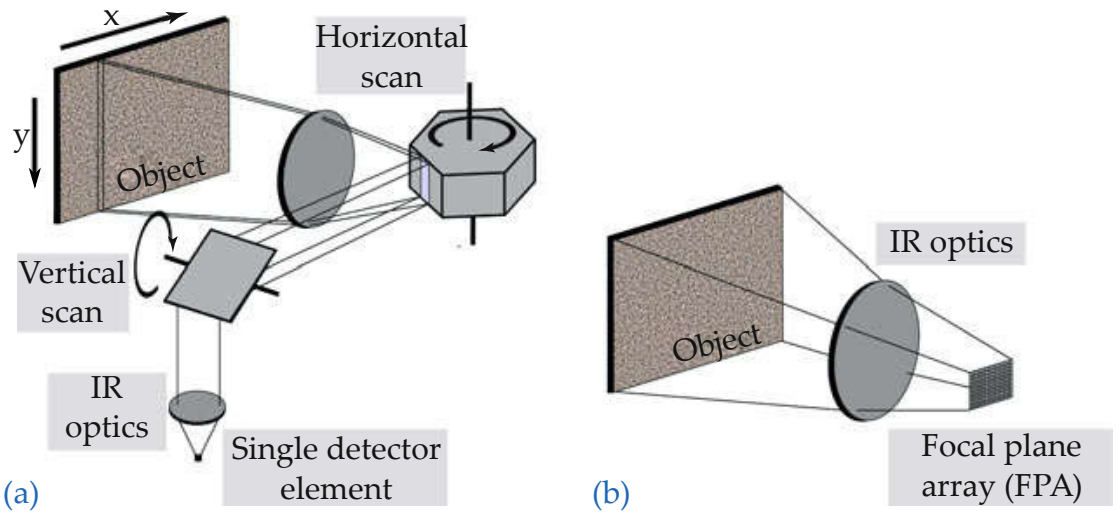

Figure 2.19.: Scanning (a) and staring (b) IR camera types. Taken from [10].

stares at its particular FOV, described by the horizontal and vertical instantaneous field of view HIFOV, VIFOV, shown in figure 2.20.
The infrared image is then composed of pixels arranged in rows and columns, with each pixel representing a detector element.

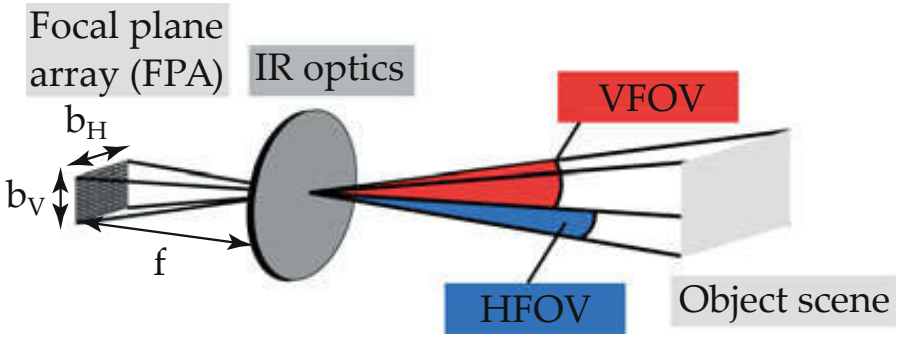

Figure 2.20.: IFOV of a staring IR camera system. Taken from [10].

3. Methodology

In this chapter, the infrared thermography principles in chapter 2 are applied to the particular boundary conditions. These boundary conditions are defined for the solar dish facility and lead to the radiometric chain, described in the first section 3.1. The following section 3.2 specifies the radiometric chain by giving hypotheses and simplifications about the involved components. In the third section 3.3 the characteristics of the particular employed camera model are given. The final section 3.4 of this chapter combines the findings about the radiometric chain (section 3.2) with the theoretical (section 2.2) and particular (section 3.3) processing in the IR camera, to obtain a radiometric model and ascertain its parameters using correlation functions and experiments.

3.1. Radiometric modeling of the solar dish facility

The following section describes the modeling of the solar dish test bench in terms of the radiometric chain. First the functionality and basic components of a solar dish concentrator are described and afterwards the radiometric modeling is carried out.

3.1.1. Solar dish concentrator

Solar concentrators are divided into concentrating linear Fresnel, parabolic trough, dish and solar tower systems. The explanation is restricted in the following to a solar dish concentrator, exemplarly shown in figure 3.1.
The main component of the facility is the solar dish, a parabolic shaped mirror concentrating sunlight onto the test bench. The dish facility includes a two axis azimuth-elevation drive system to track the sun position.
The test bench, spotlighted by the solar dish, contains five strings of tubular coated samples, shown in figure 3.2. Their temperature is regulated by a cooling air flow, with each string of samples being connected to a blower. Each string of samples consists of three individual samples of same material substrate and

Figure 3.1.: Solar dish test facility. The solar dish (1) with the mounted IR camera (2) collects sun radiation onto the test bench (3).

coating. The sample locations are defined with respect to their relative position to the blower, i.e. inlet, center, outlet.
Each sample temperature is measured with a thermocouple in a drill hole [9], shown in figure 3.3 for one sample string. A surface temperature is estimated based on the thermocouple measurement and a calculation of the temperature gradient. Additionally the samples surface temperature will be measured by an infrared camera, mounted at the center of the dish.

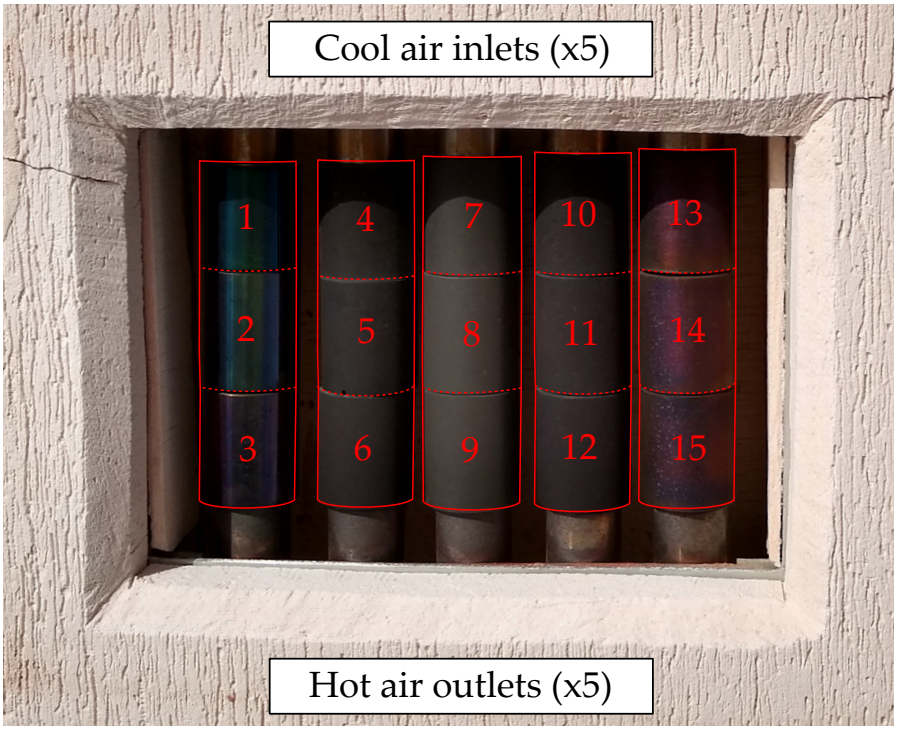

Figure 3.2.: Test bench of the solar dish facility. Five air cooled absorber strings (red framed), include cylindrical coated absorber samples (1-15), subdivided by dashed lines. The sample on the top, middle and bottom of each string is called inlet (1, 4, 7, 10, 13), center (2, 5, 8, 11, 14) and outlet sample (3, 6, 9, 12, 15).

3.1.2. Solar dish DISTAL II

In the following are some information about the particular solar dish test facility DISTAL II (figure 3.1) given. The diameter of the solar dish is 8.5 m, yielding with some deduction due to shadows a reflecting area A_{refl} of 52.54 m^2 [39]. The radiant power Φ_{sun} collected by the solar dish can be calculated with a direct normal irradiance (DNI) of the sun as

$$\Phi_{\text{sun}} = \text{DNI} \cdot \rho_{\text{refl}} \cdot A_{\text{refl}}. \tag{3.1}$$

For a DNI of 1000 Wm^{-2} and reflectivity ρ_{refl} of 94 % a collected radiant power $\Phi_{\text{sun}} = 49.39 \pm 0.25\,\text{kW}$ is calculated [39].
The solar dish DISTAL II was build 1997 to power a stirling motor with a focal length of $f = 4.1\,\text{m}$. Since this configuration in combination with the blower cooling would result in an overheating of the samples, the solar dish is operated for the aging process out of focus at a focal length of $f \approx 5.0\,\text{m}$. The focal length is adjusted with a linear drive to compensate for daily and seasonal DNI variations.

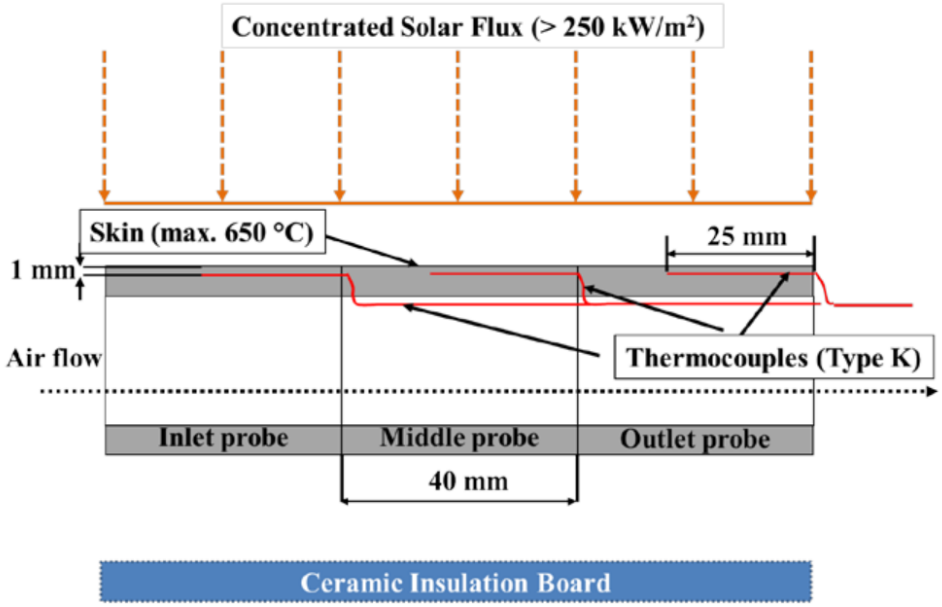

Figure 3.3.: Detailed information about the thermocouple measurement of one sample string [9].

The samples are then operated in a temperature range of 200 to 650 °C.
With the irradiated (focus) area A_f at the test bench, the concentration factor ζ of the solar dish can be calculated as the reflecting area related to the focus area

$$\zeta = A_{\text{refl}} / A_f. \tag{3.2}$$

With the reflecting area $A_{\text{refl}} = 52.54\,\text{m}^2$ and a later calculated focus area $A_f = 0.15\,\text{m}^2$ (section 4.7), a concentration factor $\zeta \approx 350$ is calculated.

3.1.3. Aging process

To gain insight about the sample material and coating properties along their lifetime, accelerated aging test campaigns are carried out.
One test campaign consists of 100 thermal cycles, whereby the coatings optical properties are measured before the campaign and periodically after 25 cycles.
One thermal cycle consists of a heating phase, a dwell phase and a cooling phase.
In the heating phase, the surface temperature is heated from 200 to 650 °C at a constant heat rate of 30 °Cmin^{-1}. The surface temperature is maintained in the dwelling phase at 650 °C with a minimum average solar flux of 250 kWm^{-2}. The cooling phase is the inverse of the heating phase, with a cooling of the surface temperature from 650 to 200 °C at a constant cooling rate of -30 °Cmin^{-1}.

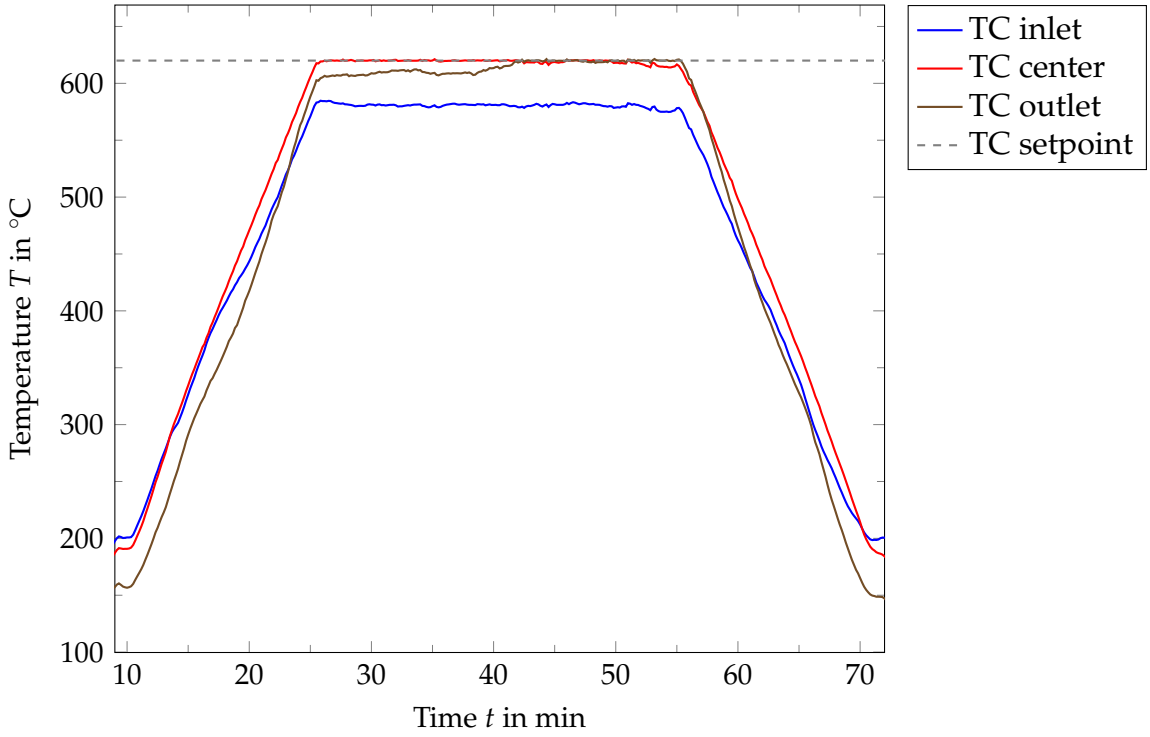

Figure 3.4.: Thermal cycle of the accelerated aging test campaign.

One temperature cycle is shown in figure 3.4 for one string of three samples, for which the thermocouple readings are plotted. The blower is regulated to maintain a maximum temperature setpoint of 620 °C at the center thermocouple. Due to the distance of the thermocouple to the surface of 1 mm, shown in figure 3.3, a surface temperature of approximately 650 °C is reached. The center and outlet samples approach the setpoint temperature, while the temperature of the inlet sample is cooler with greater variations.

3.1.4. Radiometric chain

In the following a stationary radiometric model of the solar dish facility is established in terms of energy flux contributions. The model is shown in figure 3.5. It considers the sun and ambient environment (sun), the object to be examined (object), the air (atmosphere) between IR camera and object, a protective window mounted in front of the camera (window) and the infrared camera itself (IR camera).

The Energy flux of the sun Φ_{sun} reflected by the solar dish and ambient objects is incident on the opaque object, where it is partly absorbed and partly reflected.

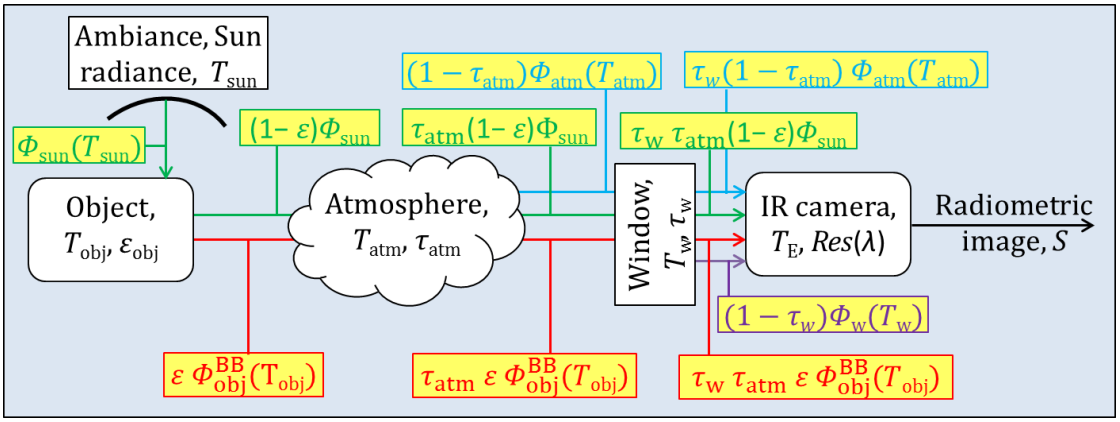

Figure 3.5.: Radiometric chain, including Ambiance, sun, object to be examined, atmosphere, protective window and IR camera.

The reflected part can be described with regard to the reflectivity and equation 2.17 as

$$\rho_{obj}\Phi_{sun} = (1-\varepsilon_{obj})\Phi_{sun}. \tag{3.3}$$

The absorbed part of the incident energy flux causes the object to heat up to a temperature T_{obj}. While the objects own radiation depends on this temperature, its energy flux is described with its emissivity ε according to a blackbody of the same temperature

$$\Phi_{obj}(T_{obj}) = \varepsilon_{obj}\Phi_{obj,BB}(T_{obj}). \tag{3.4}$$

The reflected and emitted energy flux of the object pass an amount of transparent atmosphere on their way to the infrared camera. This is taken into account by multiplying the energy fluxes with the transmissivity of the atmosphere.
The absorption of energy flux causes the atmosphere to heat up and radiate. If the absorbed amount of energy flux is assumed to be dominant over the scattered amount, then the radiating energy flux of the atmosphere is $(1-\tau_{atm})\Phi_{atm}$.
After the atmosphere, these energy fluxes of sun, object and atmosphere pass the protective window in front of the infrared camera. The protective window is modeled similar to the atmosphere, multiplying a window transmissivity τ_w to the passing energy fluxes and emitting an own energy flux $(1-\tau_w)\Phi_w$.
The energy flux incident on the infrared camera Φ_{IRcam} then yields

$$\Phi_{IRcam} = \tau_w\tau_{atm}(1-\varepsilon_{obj})\Phi_{sun} + \tau_w\tau_{atm}\varepsilon_{obj}\Phi^{BB}_{obj} + \tau_w(1-\tau_{atm})\Phi_{atm} + (1-\tau_w)\Phi_w. \tag{3.5}$$

The further processing by the IR camera is described in section 3.4.

3.2. Hypotheses and simplifications of the radiometric chain

Crucial for the infrared measurement under atmospheric conditions is its absorption of particular wavelength bands. The transmissivity of the atmosphere close to the earth's surface is shown in figure 3.6 as a function of the wavelength for a 10 and 100 m transmission. Potential wavelength bands for an infrared mea-

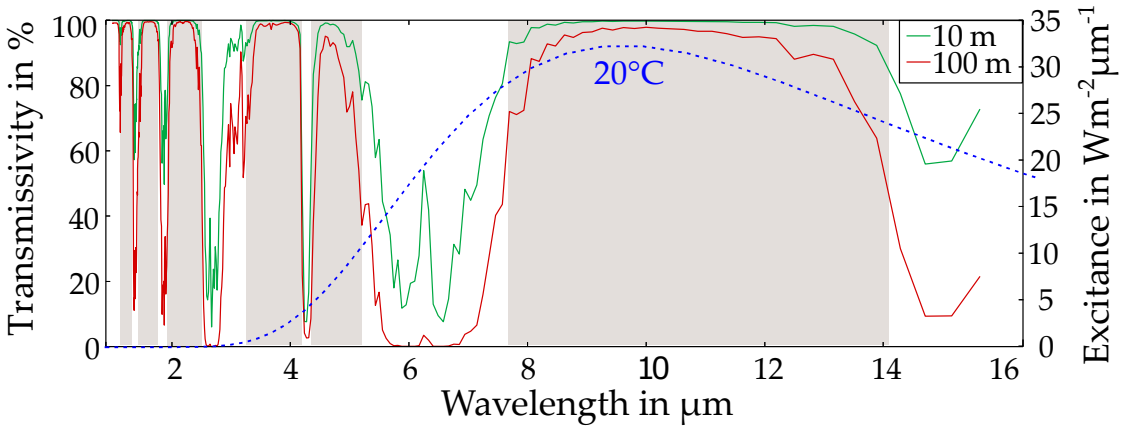

Figure 3.6.: 10 and 100 m(green, red) central European atmospheric transmission and excitance (blue) of a 20 °C blackbody as a function of the wavelength. Taken from [40].

surement with a high transmissivity are highlighted in grey. They are typically indicated as the short-wave (SW) band from 0.9 to 1.7 µm, the mid-wave (MW) band from 3 to 5 µm and the long-wave (LW) band from around 8 to 14 µm.
The measuring wavelength band for the IR camera should be chosen to maximize the portion of object radiation and minimize the portion of interfering radiations incident on the IR cameras detector element. Whereas the potential interfering radiations (section 3.1.4, equation 3.5) are the reflected sun radiation, reflected ambient radiation, atmosphere and protective window radiation. These are compared in the following to the object radiation.

3.2.1. Reflected sun radiation

The extraterrestrial spectral irradiance of the sun, i.e. the solar spectrum, is shown in figure 3.7 (blue line) and found out to be very similar to a 5777 K blackbody irradiance. When passing the earths atmosphere, this irradiance is reduced to the global irradiance (red line) due to molecular absorption and scattering.

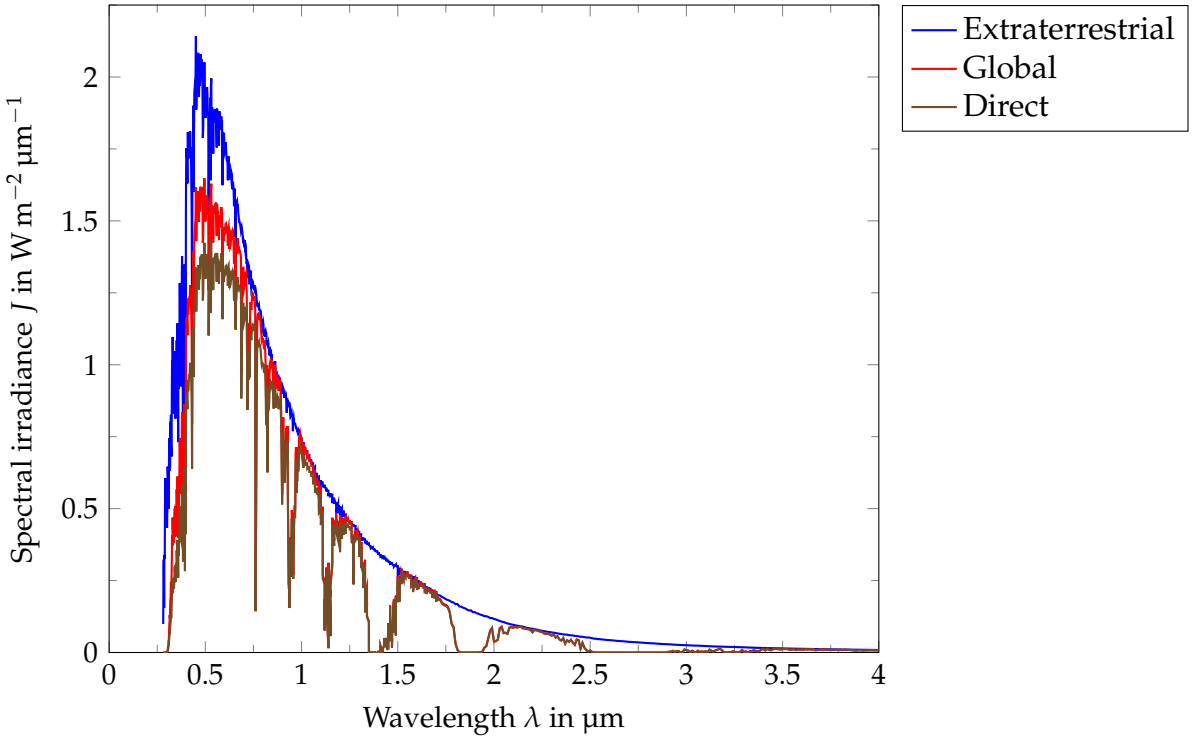

Figure 3.7.: Extraterrestrial, global and direct solar irradiance as a function of the wavelength. Edited from ASTM International [41].

Moreover, only the direct irradiance (brown line) is applicable, due to the use of concentrating facilities with optical lenses (section 2.2.1).

To calculate the influence of a solar concentrator on the spectral solar irradiance, Pfänder [1] applied an area concentration factor of 1000 and a reflectivity of typical concentrating mirrors [42]. His findings are shown in figure 3.8, with the reflectivity (magenta line), spectral solar irradiance (brown line) and reflected spectral solar irradiance (orange line) over the wavelength spectrum. The concentrating mirrors have a very large reflectivity in the short wavelength range (0.5...2.8 µm) and a small reflectivity at higher wavelength ranges, with the exception of a moderate peak at 9 µm. This reflectivity drop is evident in the difference of solar spectrum (brown line) to reflected solar spectrum (orange line).

This resulting reflected spectrum (orange line) is then compared in figure 3.9 to radiations of blackbodies (black lines) of $T_{BB} = 673\,K$ and $T_{BB} = 1273\,K$, modeling the object radiation.

The constraints at the solar dish facility (section 3.1.1) are very similar to those of Pfänder [1], with the difference that the concentration factor is approximately 350 (section 3.1.2) instead of 1000, resulting in a lower reflected sun irradiance.

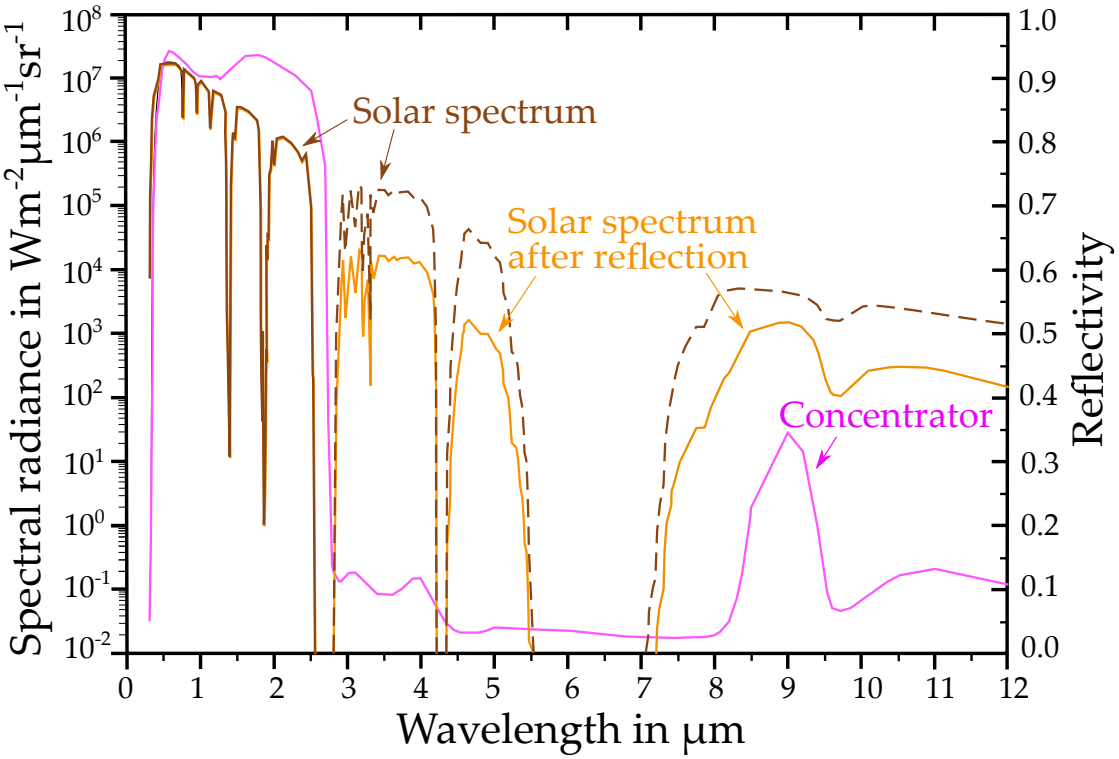

Figure 3.8.: Solar radiation after reflection at a heliostat. From Pfaender et al. [1]

Furthermore a typical dish object temperature of 923 K (650 °C) is within the range of the blackbody temperatures.
Therefore, the results in figure 3.9 can also be applied to the dish setup. In the wavelength bands of 4.3 to 5.5 µm and 7.6 to 14 µm, blackbody radiation is at least one magnitude greater than the reflected solar radiation. These ranges are described as solar blind. Restricted by narrow band pass filters, an infrared measurement in these wavelength bands is preferable.
To compute real radiations, the object emissivity has to be included (section 3.1.4). For typical absorber emissivities greater than 0.5, the amount of reflected solar radiation compared to the object radiation would reduce even further.

3.2.2. Ambient, atmosphere and window radiation

To roughly estimate the influence of ambient, atmosphere and window radiation, they are modeled as blackbodies of temperatures $T_{amb} = T_{atm} = T_W = 313.15\,K$ (40 °C). The exitance over all wavelengths is then calculated with the

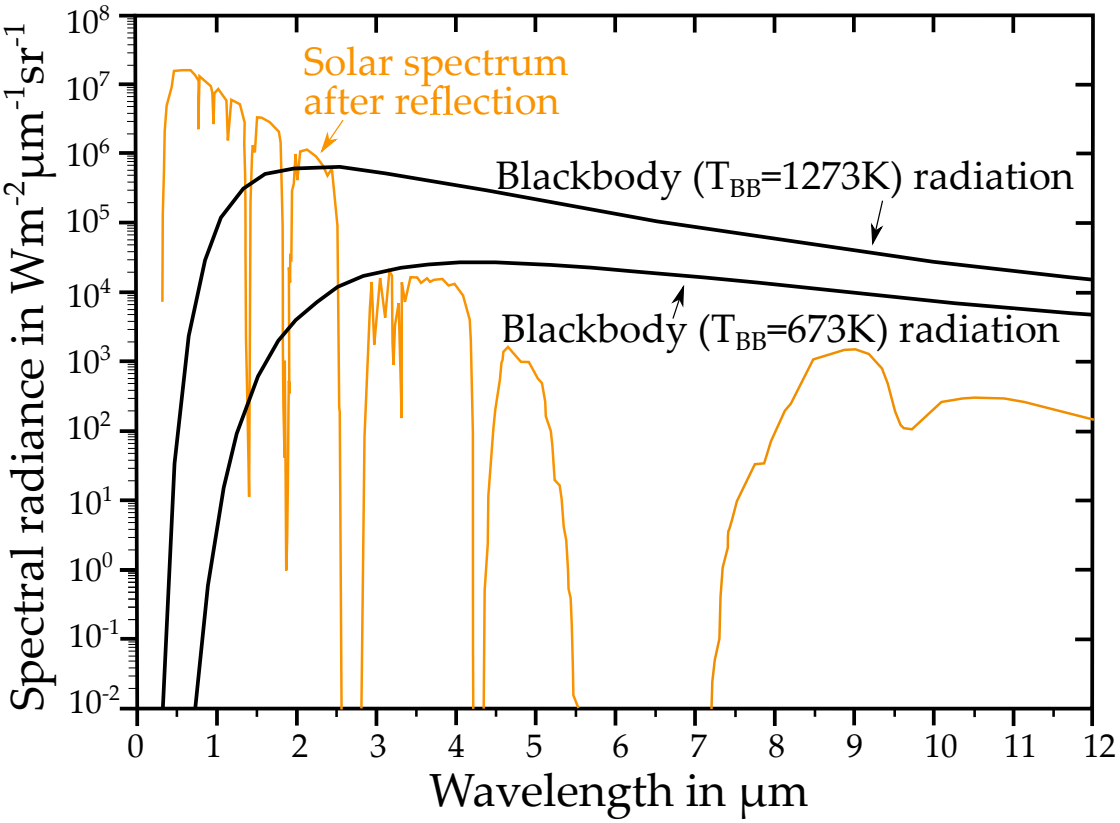

Figure 3.9.: Comparison of reflected solar spectrum to blackbody radiation of $T_{BB} = 673\,K$ and $T_{BB} = 1273\,K$. From Pfaender et al. [1]

Stefan-Boltzmann law (equation 2.23) as

$$M_{BB}(313.15\,K) = \sigma \cdot (313.15\,K)^4 = 545.28\,Wm^{-2}. \tag{3.6}$$

Similarly, for an exemplary absorber temperature of 923.15 K (650 °C), the Stefan-Boltzmann law yields

$$M_{BB}(923.15\,K) = \sigma \cdot (923.15\,K)^4 = 41181.32\,Wm^{-2}. \tag{3.7}$$

Each of the interfering radiations is roughly estimated to account for an non neglectable error of $545.28/41181.32 \approx 1.32\,\%$. The interfering radiations are therefore further considered in the discussion and results section 4.4 , taking into account the emissivity of the ambient $(\varepsilon_{amb}, \varepsilon_{obj})$, atmosphere $(1 - \tau_{atm})$ and window $(1 - \tau_W)$.

3.2.3. Object emissivity

The further described radiometric properties are obtained for the measuring wavelength band of the IR camera from $\lambda_{\text{min}} = 7.55\,\mu\text{m}$ to $\lambda_{\text{max}} = 8.35\,\mu\text{m}$, described in the section 3.3.
The reflectivity and thus the emissivity of the opaque coated samples are characterized utilizing a Perkin Elmer Frontier-FTIR spectrophotometer with a Pike LTD integrating sphere as accessory (appendix B.4). The spectrophotometer measures the hemispherical reflectance of a coated sample. Utilizing Fourier transform spectroscopy (FTS), a wavelength spectrum from 2 to 16 µm with 0.004 µm steps is measured.
Similar to the thermographic measurement, the detector is calibrated with a reference object of reflectivity $\rho_{\text{ref}}(\lambda)$ to obtain a reference output signal $S_{\text{FTS,ref}}(\lambda)$. For the ideal case of a white body $\rho_{\text{ref}}(\lambda) = 1$ would hold. Since the coated sample and the reference object are effected by the same radiation, their behavior can be described as

$$\frac{S_{\text{FTS,ref}}(\lambda)}{\rho_{\text{ref}}(\lambda)} = \frac{S_{\text{FTS,sample}}(\lambda)}{\rho_{\text{sample}}(\lambda)}. \tag{3.8}$$

The coated samples reflectivity $\rho_{\text{sample}}(\lambda)$ can then be calculated with the known reference values and measured sample signal $S_{\text{FTS,sample}}(\lambda)$ [43].
With equation 2.17 for opaque bodies, spectral emissivities $\varepsilon(\lambda)$ are calculated for an exemplary selective (F2) and non selective (D532) coating, shown in figure 3.10a over the whole measured wavelength range (2...16 µm). Furthermore, the coatings emissivities are shown in the particular wavelength range of the IR camera (7.55...8.35 µm) in figure 3.10b. The coating emissivities for particular wavelength bands are calculated by weighting with blackbody radiation (equation 2.20). For the overall thermal emissivity this yields

$$\varepsilon_{\text{th}}(T) = \frac{\int_{\lambda=0.28}^{16\,\mu\text{m}} \varepsilon(\lambda) M(T,\lambda)\,\mathrm{d}\lambda}{\int_{\lambda=0.28}^{16\,\mu\text{m}} M(T,\lambda)\,\mathrm{d}\lambda} \tag{3.9}$$

and for the emissivity in the wavelength band of the IR camera, stated throughout this work as $\varepsilon_{\text{obj}}(T)$

$$\varepsilon_{\text{IRcamera}}(T) = \varepsilon_{\text{obj}}(T) = \frac{\int_{\lambda=7.55}^{8.35\,\mu\text{m}} \varepsilon(\lambda) M(T,\lambda)\,\mathrm{d}\lambda}{\int_{\lambda=7.55}^{8.35\,\mu\text{m}} M(T,\lambda)\,\mathrm{d}\lambda}. \tag{3.10}$$

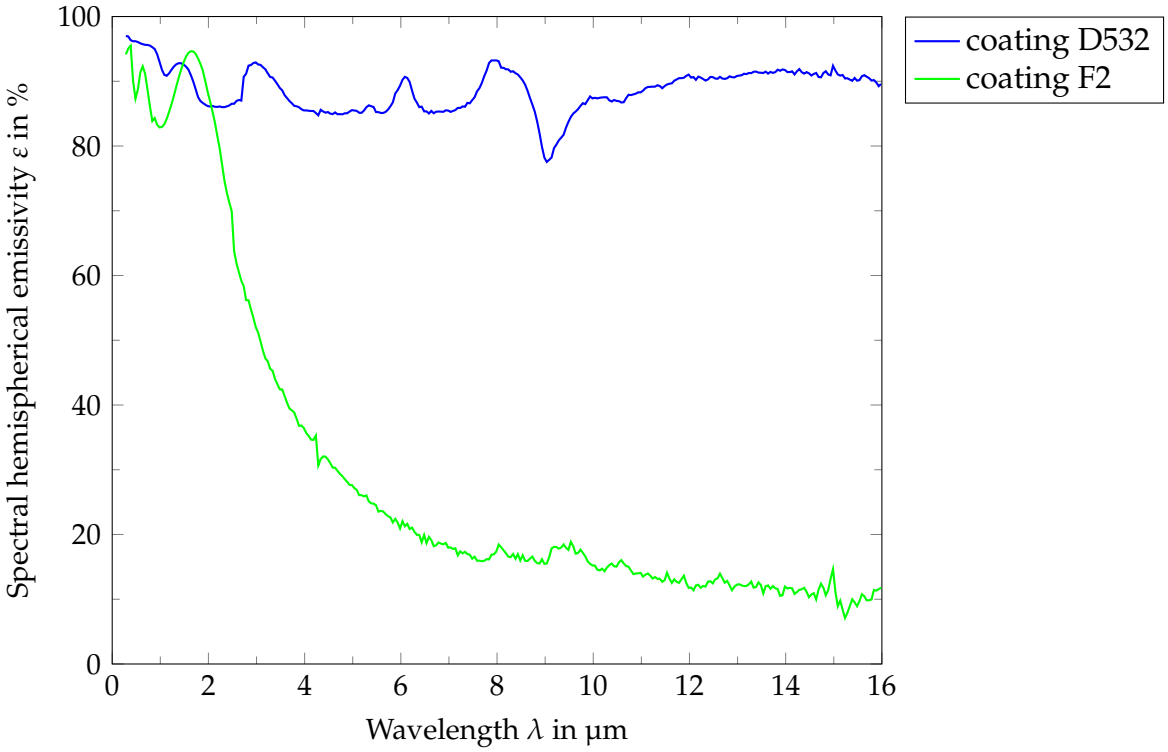

(a) Emissivities over the whole wavelength band.

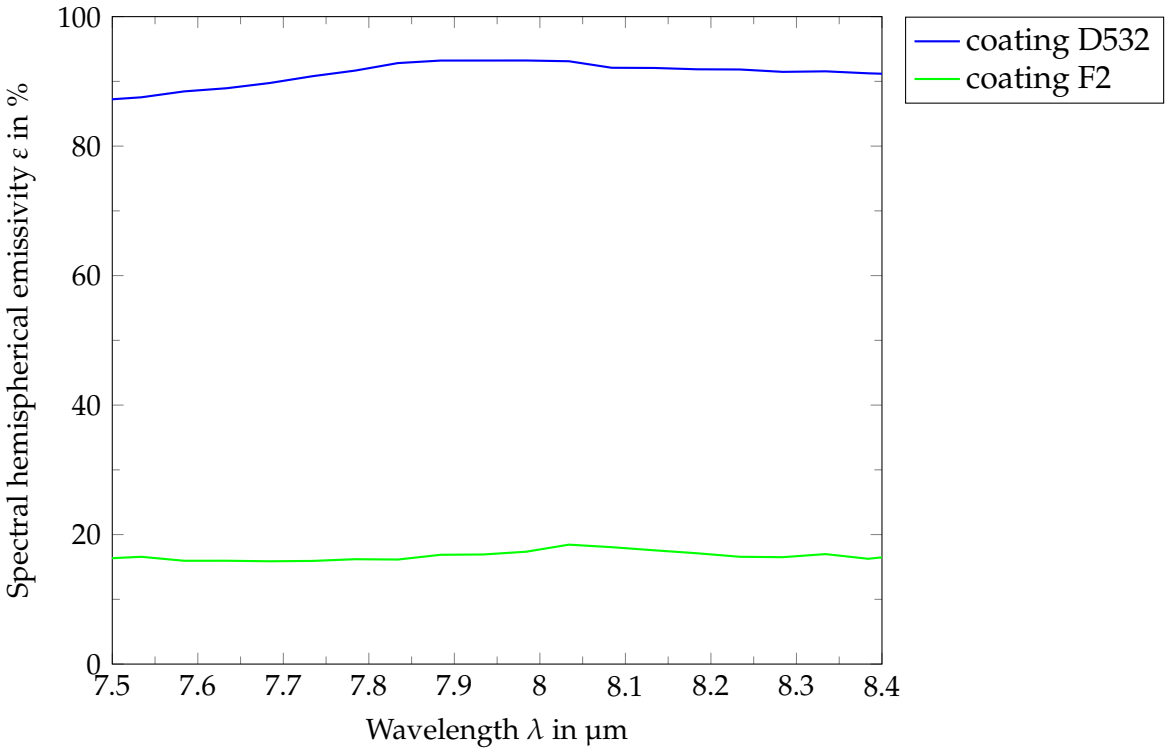

(b) Emissivities in the wavelength band of the IR camera.

Figure 3.10.: Emissivities of the D532 and F2 coating measured by spectrophotoscopy as a function of wavelength.

According to Wien's law (equation 2.21), an increasing coating temperature shifts the maximum spectral exitance towards smaller wavelengths. The thermal emittance varies then with the temperature if the coating is not a gray body.

3.2.4. Atmospheric transmissivity

To calculate the atmospheric transmissivity, the simulation program MODTRAN [18] was used. Modtran calculates the spectral transmissivity based on physical principles, such as absorption and scattering and utilizes reference data such as composition of the atmosphere in Europe, distance and relative humidity. For a measurement distance at the dish facility of 5 m and three relative humidities (0.1, 0.5 and 0.9), each spectral transmissvity is calculated and shown in figure 3.11 over the range of the IR camera wavelength band from $\lambda_{\text{min}} = 7.55\,\mu\text{m}$ to $\lambda_{\text{max}} = 8.35\,\mu\text{m}$. While smaller transmissivities are observed for greater relative humidities, the minimum transmissivity with 99.45 % at $\lambda = 7.67\,\mu\text{m}$ is still very high. For an average transmissivity of about 99.85 % in this wavelength band, the absoptivity and thus the emissivity is $\varepsilon_{\text{atm}} = 100\,\% - \tau_{\text{atm}} = 0.15\,\%$, when neglecting scattering radiation. Due to the very small resulting radiation of the atmosphere (section 3.2.2) and an error of 0.15 % for passing radiations, the atmosphere is neglected compared to the object radiation for the further modeling of the radiometric chain.

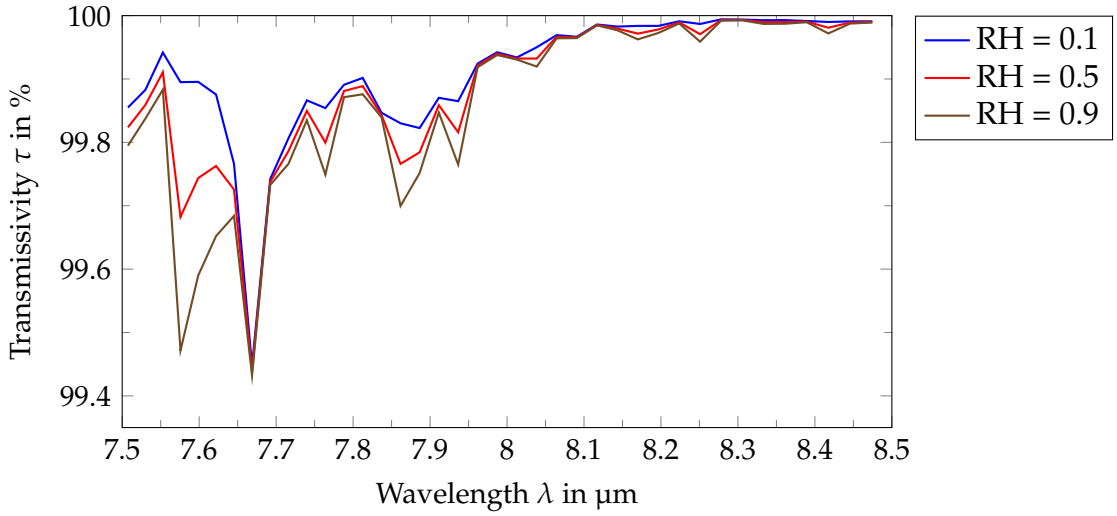

Figure 3.11.: 5 m transmissivity of an European atmosphere as a function of the wavelength. Calculated with MODTRAN [18].

3.2.5. Transmissivity protective window

The additionally mounted protective window with a diameter of 50.8 mm consists of Germanium with an anti reflective coating. Since no spectral transmissivity was given from the manufacturing company, it is obtained from experiments (section 3.4.3).

3.3. Optris IR camera

The choice of the IR camera model depends on various aspects. Besides the prior described wavelength range (section 3.2.1) practical aspects such as temperature measurement range, relative error, spatial resolution, cooling, weight, size, and price have to be concerned. A compromise was found for the model PI640 G7, manufactured by the company Optris GmbH. Relevant data for further calculations are the measurement range of 200...1500 °C, the measuring spectrum of (7.95 ± 0.4) µm and the spatial resolution of 640x480 pixel with the solid viewing angle of 15°x11°. Figure 3.12 shows the resulting FOV area for the particular camera model at a 1 and 5 m distance. Further information can be found in the data sheet included in the appendix B.1.

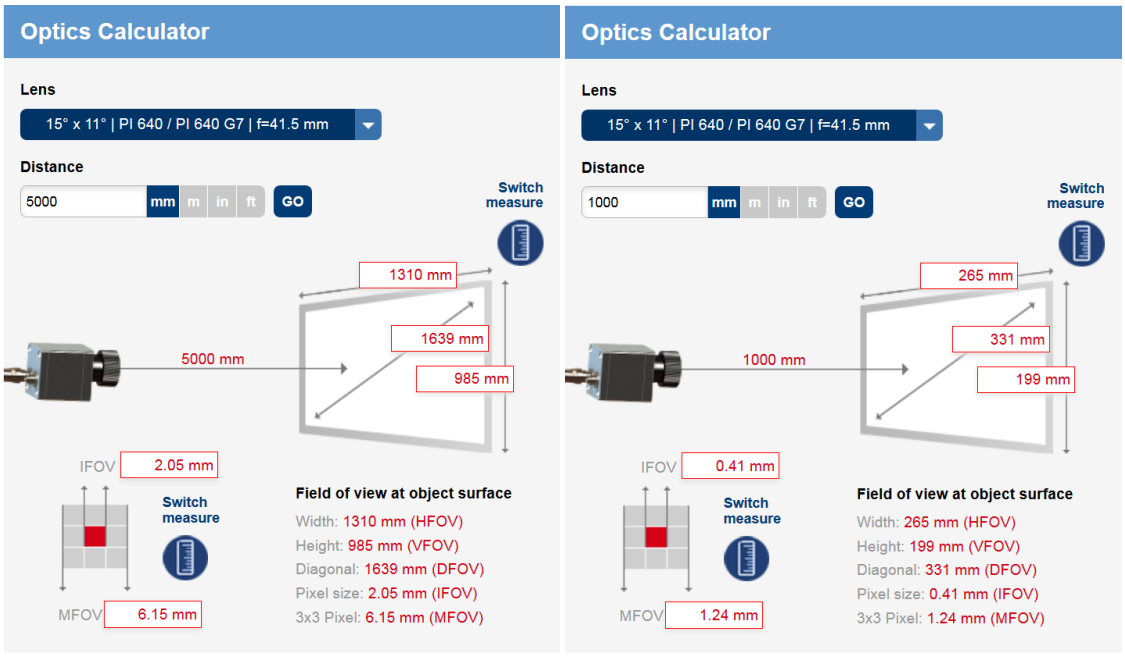

(a) IR camera - object distance of 1000 mm.

(b) IR camera - object distance of 5000 mm.

Figure 3.12.: Optic properties of the IR camera model PI640 G7 at different distances, determined with an online calculator (www.optris.com/optics-calculator) of the Optris company.

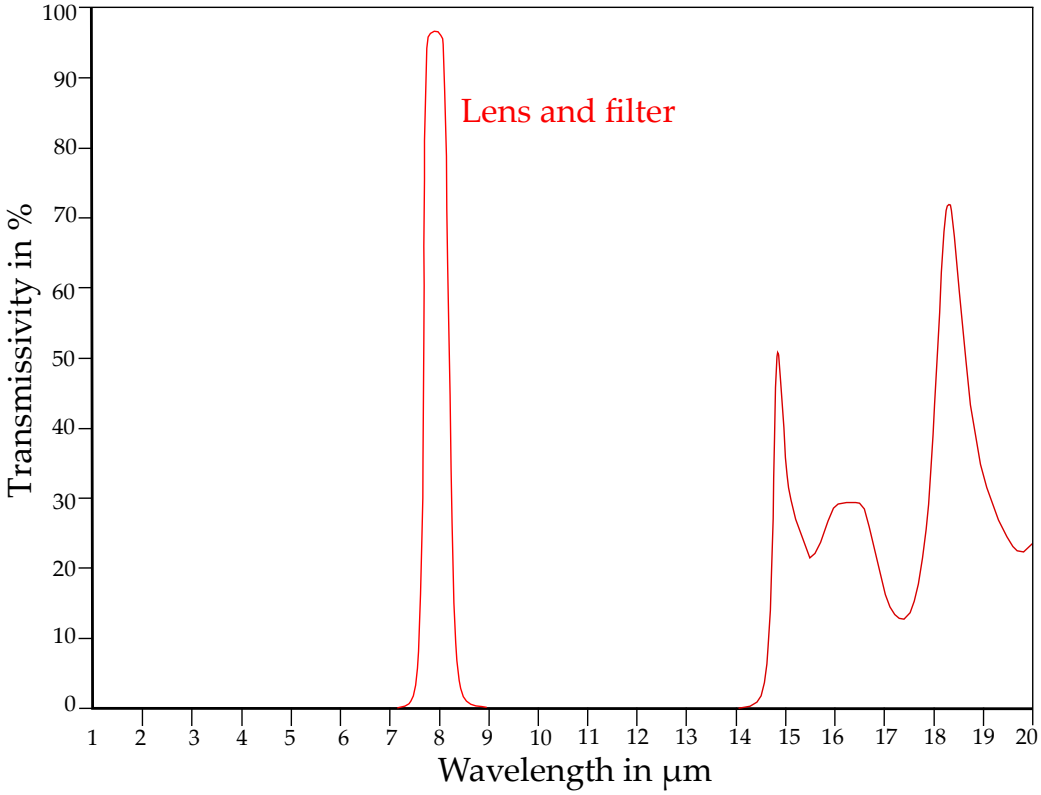

(a) Transmissivity of filter and lens from the utilized IR camera model PI640 G7

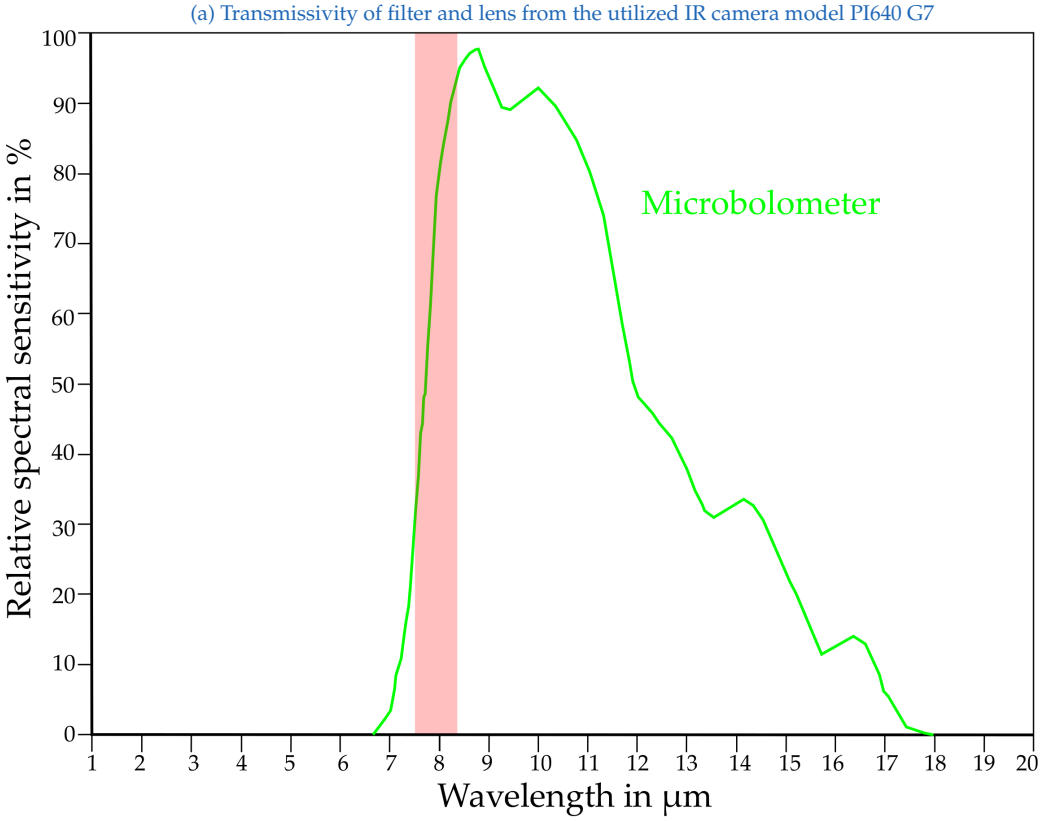

(b) Sensitivity s_{det} of a micriobolometer detector element, edited from [10]

Figure 3.13.: Radiometric properties of the IR camera PI640 G7.

3.3.1. Radiometric properties of the PI640 G7 IR Camera

The radiometric properties of a radiation thermometer, i.e. IR camera consist of a lens and filter transmissivity τ_l and τ_f, the sensitivity of the detector element(s) s_{det} and a description of the signal processing (section 2.2).
The IR camera model PI640 G7 includes an optical lens with a coated filter. The combined transmissivity of optical lens and filter is given by the Optris company as shown in figure ??. It is apparent, that the transmissivity is reduced to wavelength ranges from $\lambda_{min,1} = 7.55\,\mu m$ to $\lambda_{max,1} = 8.35\,\mu m$ and $\lambda_{min,2} = 14\,\mu m$ to $\lambda_{max,2} = 20\,\mu m$.
Because of Optris intellectual property restrictions, information about the detector and signal processing was not provided. The obstructed detector is an uncooled microbolometer focal plane array (FPA). Its spectral sensitivity is shown exemplary in figure ?? and ranges from $\lambda_{min} = 6.5\,\mu m$ to $\lambda_{max} = 18\,\mu m$. In combination with the transmissivity of the optical lens and filter (figure ??) it is assumed that the major part of the detected radiation is in the red highlighted wavelength range from $\lambda_{min} = 7.55\,\mu m$ to $\lambda_{max} = 8.35\,\mu m$.

3.3.2. Calibration curve

A detailed radiometric description throughout the IR camera is made impossible, due to the lack of hardware information and complexity of radiation propagation and transduction.
Therefore the calibration curves (section 2.2.5) of the IR camera were utilized, shown in figure 3.14 for the sighting (red) and measuring (blue) range.
These calibration curves were measured without an additional protective win-

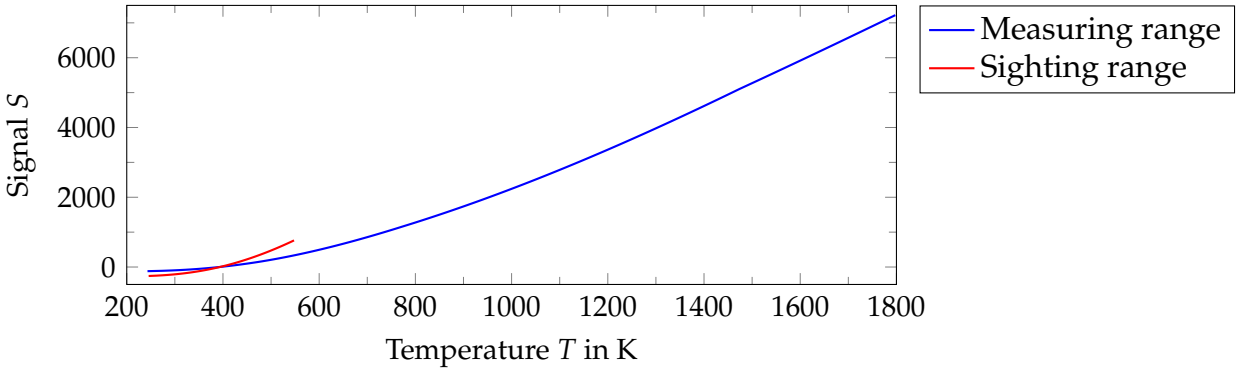

Figure 3.14.: IR camera calibration curves. Measuring (250...1500 °C) and Sighting range (0...200 °C)

dow, i.e. they include the radiation conversion of the optical lens, spectral filter, detector element and signal processing. Further calibration information is documented in the calibration certificate (appendix B.5). For the estimation of the SSE, information about the measuring range and the blackbody size is however missing.

3.3.3. Optris Software

A propietary Optris software (PIX Connect) was available for the control of the IR camera. A snapshot of the graphical user interface is shown in figure 3.16. The main advantages of the software are:

- Easy operability, by pointing and clicking
- Online temperature measurement
- Monitoring of ambient, internal and chip temperatures, including alarms
- Automatic recording of thermographic images with metadata (chip and case internal temperature) and time stamps
- Adjustment of radiometric parameters in online measurement and playback mode of recorded images
- Temperature measurement of self defined subareas
- Access to the metadata of saved thermographic images

This software however has some disadvantages for quantitative thermographical analyses:

- No direct access to radiometric data
- No information about the radiometric model
- SSE correction not implemented
- Image segmentation is not automatic

The general infrastructure of the software is proven to be very useful in securing a stable connection to the IR camera, obtaining thermographic images, chip and internal enclosure temperatures with implemented warnings for overheating. Therefore the software by the Optris company was used for the online measurement and recording of thermographic images. To solve some of the software technical limits, recorded images were post-processed in MATLAB for object segmentation and radiometric processing.

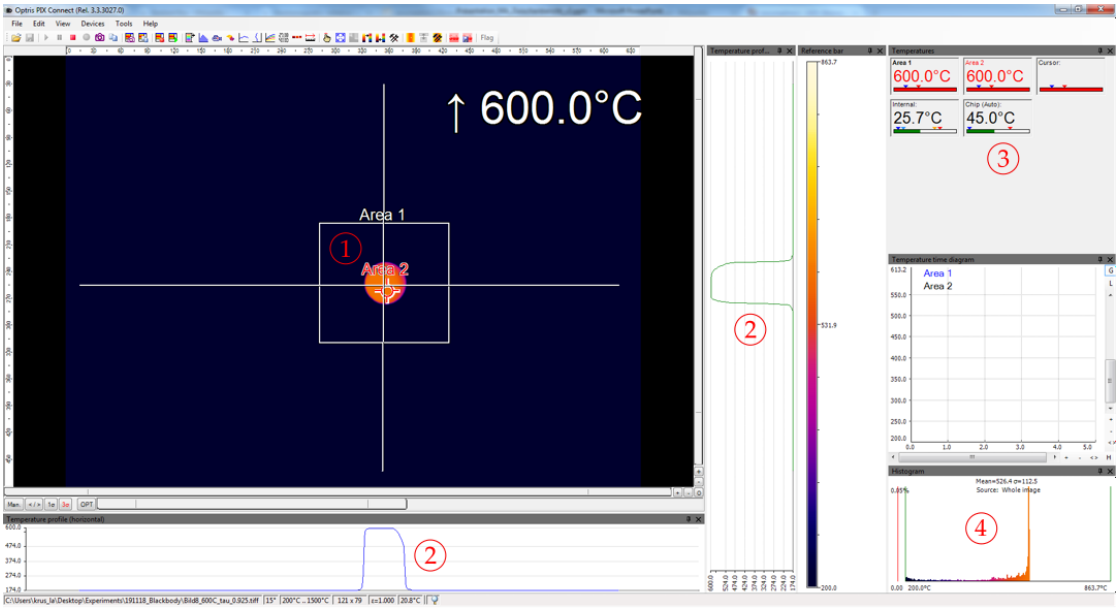

Figure 3.15.: Snapshot of the graphical user interface of the software PIX Connect. Temperature regions in the live thermographic image (1) are selected and quantified by temperature profiles (2), temperature areas (3) and histograms (4).

3.3.4. Image post-processing

To obtain insight in the temperature calculation and be able to correct physical effects, knowledge of the radiometric data is essential. The postprocessing script is therefore structured around the segmentation and processing of radiometric data as follows:

- Format conversion and reading of the thermographic image and additional radiometric properties
- Segmentation of the objects using image processing operators, such as the prewitt operator, dilation and erosion
- Generation of sampling areas, as part of the segmented object
- Thermographic statistics generation of the sampling areas
- Radiometric conversion of the statistics and processing with the radiometric properties and SSE
- Thermographic conversion, saving and output of the object statistics

The specific calculations are described for the particular set ups at the experiments and the dish facility in section 4.

3.4. Radiometric model identification

This section concerns the whole radiometric model, including the radiation considerations in the radiometric chain and the processing and conversion (section 2.2) in the particular IR camera (section 3.3) until the obtainment of an thermographic image.
The radiometric chain (equation 3.5) can be rearranged by neglecting the influence of sun radiation (section 3.2.1) and atmosphere (section 3.2.4). The sun radiation Φ_{sun} reduces then to an ambient radiation Φ_{amb}. Furthermore assigning radiances L with the IR cameras particular solid angle and area for the energy fluxes Φ yields

$$L_{IRcam} = \tau_w(1-\varepsilon_{obj})L_{amb} + \tau_w\varepsilon_{obj}L_{obj}^{BB} + (1-\tau_w)L_w. \tag{3.11}$$

Further, representative IR camera signals can be assigned for the radiances [20], if the behavior of radiance to IR camera signal is proportional (equation 2.30):

$$S_{IRcam} = \tau_w(1-\varepsilon_{obj})S_{amb} + \tau_w\varepsilon_{obj}S_{obj}^{BB}(T_{obj}) + (1-\tau_w)S_w(T_w) - S_E(T_E) \tag{3.12}$$

S_E is here an additional offset signal related to the temperature of the camera enclosure (section 2.2). The application-specific radiometric model is further obtained by identifying a signal-temperature correlation $S(T)$ (section 3.4.1), a correction for the SSE (section 3.4.2) and the radiometric parameters τ_w (section 3.4.3) and ε_{obj} (section 3.4.5).

3.4.1. Radiometric correlation expressions

To obtain a correlation between radiometric signal and object temperature, the empirical approach (section 2.2.4) was applied due to missing information about the IR camera response Res_λ. Here the calibration curve was utilized for the fitting of the radiometric correlation expressions. Five temperature and signal values ($T_1 = 823.05\,K$, $T_2 = 873.15\,K$, $T_3 = 923.15\,K$, $T_4 = 973.05\,K$, $T_5 = 1023.05\,K$) and ($S_1 = 1378.30$, $S_2 = 1608.97$, $S_3 = 1850.22$, $S_4 = 2101.51$, $S_5 = 2363.40$) in the desired temperature range were chosen for the least square fitting procedure. Three candidate expressions for the signal $S(T)$ from Sakuma and Kobayashi [24] were selected. They are shown in table 3.1. Among them is an exponent expression, and two Sakuma-Hattori expressions in the Planck form (here called Sak-Hatt I and II). The Parameter D behaves as an offset to describe ambient radiation [24] and is not necessary to obtain the general form

Expression	Formula	Bandwidth	Planckian
Exponent Optris	$S(T) = \mathrm{C} \cdot T^{\mathrm{A}}(+D)$	broad	no
Sak-Hatt I FLIR	$S(T) = C \cdot \left[\exp\left(\frac{\mathrm{B}}{T}\right) - \mathrm{D}\right]^{-1}$	monochromatic	yes
Sak-Hatt II	$S(T) = \mathrm{C} \cdot T^{\mathrm{A}} \cdot \left[\exp\left(\frac{\mathrm{B}}{T}\right) - \mathrm{D}\right]^{-1}$	broad and narrow	yes

Table 3.1.: Candidate equations and their qualities of representing the Planck law [24].

of the formula. In their handouts, the Optris company states to use the exponent form, while the FLIR company states to apply the Sakuma-Hattori I form. The Sakuma-Hattori II form is a combination of both.
The exponent expression is similar to the Stefan-Botzmann law (equation 2.23) and thus well applicable for a broad bandwidth. For a narrow-band radiation thermometer it is limited in its temperature range [24]. The Sakuma-Hattori I expression is stated by Sakuma and Kobayashi [24] to be applicable for a radiation thermometer with a monochromatic band. The Sakuma-Hattori II expression behaves for low temperatures like the Sakuma-Hattori I expression and for high temperatures like the exponent expression.

3.4.2. Recalibration of the IR camera

The first experiment is performed to recalibrate the focus and size of source effect.

Figure 3.16.: Setup of the MIKRON M305 calibration blackbody (1) and the PI640 G7 IR camera (2) for the recalibration.

Calibration requirements were reproduced by measuring a blackbody at room temperature with the IR camera PI640 G7, while having the protective window demounted, shown in figure 3.16. Detailed information about the blackbody model M305 from the manufacturing company MIKRON, shown in figure 3.17, can be found in the appendix B.2.

Figure 3.17.: Calibration blackbody M305 with aperture diameter of 25.4 mm

Focus effect routine

A routine to identify the focus effect is described in Saunders [33]. For an closed up IR measurement of a blackbody it is stated, that a change in focal length should not affect the measurement in the center of the IR image. Following the described routine, the IR measurement was held under the smallest IR camera - blackbody range, with the focal length varied from one to the other extreme. Here the smallest possible IR camera - blackbody range was measured to be 0.42 m instead of the postulated few centimeters.

Size of source effect routine

Saunders [44] further specified a routine for the identification of the SSE with the same blackbody setup (figure 3.16). He states that the crucial parameter for the SSE identification is the angular target size θ of the blackbody calibration source. The further called recalibration routine follows that multiple angular target sizes

$\theta_1, \theta_2, ...$ are obtainable, when varying the distance $D_1, D_2, ...$ of the IR camera to the blackbody, shown in figure 3.18

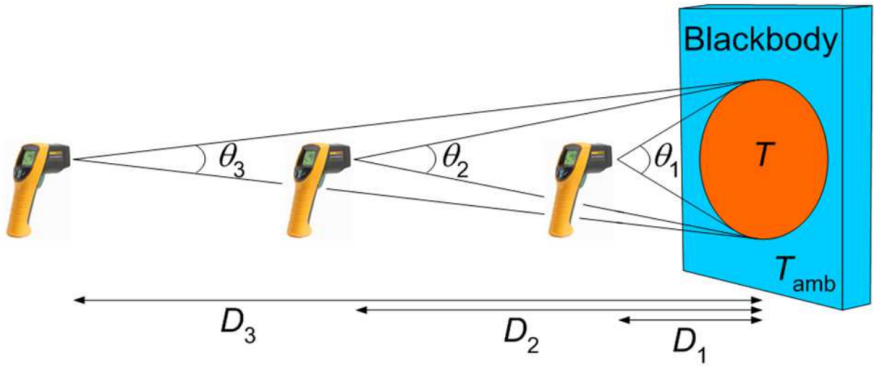

Figure 3.18.: Schematic illustration of the SSE routine. Taken from [44]

The angular target size of the initial factory calibration θ_{cal} is found, when the temperature measured by the IR camera meets the blackbody temperature. The correct radiometric signal with no influence of the SSE would be measured for an angular target size of 180°, respectively an infinitely large blackbody radiator. Empirical analytical representations of the SSE were described by Bloembergen [45] for a radiometric signal related quantity $SSE(T_{meas})$ in relation to varying blackbody diameters. To apply these empirical analytical representations, equivalent blackbody diameters X were calculated with the angular target sizes $\theta_1, \theta_2, ...$ at the distance D_{cal} found to meet initial factory calibration at the angular target size θ_{cal}. The SSE factor is calculated by relating the measured value to a reference value. Since the IR cameras error is minimized at the factory calibration, the respective signal value is chosen as the reference value:

$$SSE(X) = \frac{S_{meas}(X)}{S_{cal}(X_{cal})}. \tag{3.13}$$

With an analytical representation for the quantity $SSE(X)$, any measured signal $S_{meas}(X)$ can be transferred into an signal $S_{cal}(X_{cal})$ at the calibration distance.

3.4.3. Identification of the protective window transmissivity

The same recalibration routine (section 3.4.2), described in the SSE identification was applied with the mounted protective window. Signals of the setup without

a protective window are compared to signals of the setup with the protective window to determine its transmissivity τ_w. The protective window is shown in figure 3.19.

Figure 3.19.: Protective window mounted in front of the IR camera.

3.4.4. Validation of the radiometric model and parameters

To validate the identified focus and size of source effects the recalibration routine (section 3.4.2) was applied to another blackbody model (MIKRON M335) with a different aperture diameter $r_{BB,M335} = 8.25\,mm$. Furthermore varying temperatures were measured to exclude a temperature dependence of the focus- and size of source effect.
The blackbody M335 from the company MIKRON used for the validation is shown in figure 3.20, a data sheet of the similar M330 model is given in the appendix B.3.

Figure 3.20.: Verification blackbody M335 with an aperture diameter of 16.5 mm.

3.4.5. Emissivity identification of a real body

To test the developed radiometric model with its radiometric parameters, the measurement of a real body is carried out. A plate of inconel 625 steel is prepared with welded K-type thermocouples and painted with a Macota high temperature black paint (Model: 08008), shown in figure 3.21a. For standardization of the experiment and the SSE model, two manufactured apertures of 125, shown in figure 3.21b and 145 mm were utilized to disclose a circular area of the plate. The

(a) Plate of inconel 625 steel painted with black Macota 08008 paint.

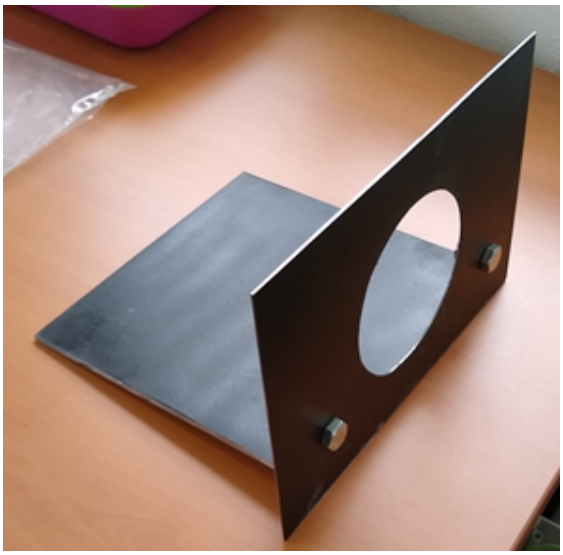

(b) Aperture painted with black Macota 08008 paint.

Figure 3.21.: Equipment used for the emissivity measurement of a real body.

plate is mounted in front of an Nabertherm L15/12/p330 muffle furnace and measured without, as shown in figure 3.22 and through the respective apertures with the IR camera PI640 G7. A custom segmentation script, here called APTSEG is made for the correct choice of pixels in the IR image, selecting automatically same sized areas next to the thermocouples and calculating mean and maximum signals. Here pixelareas of 20x20, 7x7, 6x6, 5x5 and 4x4 pixel were applied for the measured distances $D_1 = 1\,\mathrm{m}$, $D_2 = 3\,\mathrm{m}$, $D_3 = 3.5\,\mathrm{m}$, $D_4 = 4\,\mathrm{m}$ and $D_5 = 5\,\mathrm{m}$. The Macota (model: 08008) paint emissivity is then obtained by relating the IR camera signals S_{IRcam}, which are measured with the wrong emissivity $\varepsilon = 1$ to signals S_{TC}, which are equivalent to the respective thermocouple temperature (equation 2.26):

$$\varepsilon = \frac{S_{\mathrm{IRcam}}}{S_{\mathrm{TC}}} \tag{3.14}$$

Figure 3.22.: Setup for the infrared measurement with the PI640 G7 IR camera (2) of the Macota black painted Inconel 625 plate (3) heated with the Nabertherm L15/12/P330 furnace (1) [Distance: 1 m]

The radiometric model and parameters are then compared and validated with emissivities measured with the stand-alone Perkin Elmer Frontier-FTIR spectrophotometer.

3.4.6. Radiometric measurement at the dish facility

Finally the IR camera PI640 G7 was mounted at the DISTAL II solar dish facility (section 3.1.1) to measure the temperatures of the tubular coated absorber samples, shown in figure 3.23.
Due to the defocused operation of the solar dish facility DISTAL II, the samples and a part of the surrounding ceramic were illuminated, shown in the thermographic image in figure 4.21. As a result of the blower cooling, the samples reached a significantly lower temperature than the ceramic.
An additional weighted radiometric signal S_{SSE} was therefore calculated for the application of the SSE correction:

$$S_{SSE} = \psi S_{sample} + (1 - \psi) S_{ceramic} \tag{3.15}$$

Where ψ is the number of sample pixel divided by the number of ceramic pixel in the IR image, S_{sample} is the radiometric signal of the respective sample and $S_{ceramic}$ is the average radiometric signal of all ceramic pixel.

Figure 3.23.: Setup for the infrared measurement with the PI640 G7 IR camera (2) of the solar test bench (3) heated with concentrated solar radiation of the parabolic mirror (1). [Distance: 5 m]

The SSE is then applied as

$$S_{\text{Sample}} = S_{\text{Sample,radiom}} + (1 - SSE) \cdot S_{\text{SSE}}, \tag{3.16}$$

where $S_{\text{Sample,radiom}}$ is the signal processing from applying all radiometric parameters, with the emissivity among them obtained from prior spectroscopy analysis.
The signal S_{Sample} is then the corrected radiometric signal, with the calibration curve (section 3.3.2) it is transformed into the sample temperature T_{sample} .

4. Results and Discussion

The following chapter presents and discusses the results, which are obtained by applying the methods described in section 3. To identify the parameters of the radiometric model, radiometric correlation expressions were fitted (section 4.1), the focus effect identified (section 4.2), the size of source effect recalibrated (section 4.3) and the transmissivity of the protective window determined (section 4.4). The radiometric model was then validated with a blackbody (section 4.5) and a real body (section 4.6) radiation source. Finally results of two thermographic images from the solar dish facility are presented and discussed (4.7). The raw thermographic images are processed first with the radiometric model and then with the SSE correction. Thermographic images, generated with an radiometric model emissivity and transmissivity of 1 are here called raw images.

4.1. Fitting of the radiometric correlation expressions

As described in section 3.4.1, the calibration curve was utilized to fit the radiometric correlation expression in the temperature range $T_1 = 823.05\,\mathrm{K}...T_5 = 1023.05\,\mathrm{K}$. Under calibration conditions ($\varepsilon_{\mathrm{BB}} = 1$, $\tau_{\mathrm{W}} = 1$, $\tau_{\mathrm{atm}} = 1$, $T_{\mathrm{amb}} = 20\,^{\circ}\mathrm{C}$), the radiometric model in equation 3.12 reduces to

$$S_{\mathrm{IRcam}} = S^{\mathrm{BB}}_{\mathrm{obj}}(T_{\mathrm{obj}}) - S_{\mathrm{E}}(T_{\mathrm{E}}). \tag{4.1}$$

Applying the formulas from table 3.1 for the signal quantities, derives temperature related formulas, shown in table 4.1. Two effects, the SSE and the radiation from the enclosure, cause an offset to the radiometric model. Due to a temperature regulation in the IR camera, the enclosure temperature T_{E} was found to be constant under laboratory conditions at 318.15 K (45 °C).The remaining SSE offset, which was unknown at the calibration conditions, is then accounted for by the parameter D. The coupling of the two offset effects is demonstrated with the Exponent 1 (Exp 1) and Exponent 2 (Exp 2) model (table 4.1). Compared to the Exp 2 model, the Exp 1 model does not account for an additional SSE parameter D. The resulting least square fit for the Exp 1 model gives therefore an unrealistic

Model	Formula	Offset	Parameter	RMSE
Exp 1 (Optris)	$S = \mathrm{C} \cdot (T_{\mathrm{obj}}^{\mathrm{A}} - T_{\mathrm{E}}^{\mathrm{A}})$	$T_{\mathrm{E}} = 445.87$	$A = 1.79$ $C = 0.0124$	0.152
Exp 2	$S = \mathrm{C} \cdot (T_{\mathrm{obj}}^{\mathrm{A}} - (\mathrm{T_E})^{\mathrm{A}}) - D$	$D = 312.95$ $\mathrm{T_E} = 318.15$	$A = 1.79$ $C = 0.0124$	0.152
SH Pl I (FLIR)	$S = \frac{\mathrm{C}}{e^{(\mathrm{B}/T_{\mathrm{obj}})} - \mathrm{D}} - \frac{\mathrm{C}}{e^{(\mathrm{B}/\mathrm{T_E})} - \mathrm{D}}$	$\mathrm{D} = 1.01$ $\mathrm{T_E} = 318.15$	$B = 1.18$ $C = 1.568$	18.6
SH Pl II	$S = \mathrm{C}\frac{T_{\mathrm{obj}}^{\mathrm{A}}}{e^{(\mathrm{B}/T_{\mathrm{obj}})} - \mathrm{D}} - \mathrm{C}\frac{\mathrm{T_E}^{\mathrm{A}}}{e^{(\mathrm{B}/\mathrm{T_E})} - \mathrm{D}}$	$\mathrm{D} = -12$ $\mathrm{T_E} = 318.15$	$A = 1.73$ $B = 1786.9$ $C = 0.269$	0.016

Table 4.1.: Least square fitting results of the radiometric correlation expressions.

high enclosure temperature $T_{\mathrm{E}} = 445.87\,\mathrm{K}$.The Exp 2 model is then fitted with a fixed enclosure temperature $\mathrm{T_E} = 318.15\,\mathrm{K}$, resulting in an SSE related offset of $D = 312.95$. Due to the same calculated parameters $A = 1.79$ and $C = 0.0124$, an offset behavior of the parameters T_{E} and D is shown.
The Sakuma-Hattori Planck I (SH Pl I) model gives, after fitting with the fixed enclosure temperature $\mathrm{T_E} = 318.15\,\mathrm{K}$, the offset $D = 1.005$, which is interestingly very close to the value in the Planck formula 2.20.
The fitted parameters $A = 1.73$ and $B = 1786.9$ of the combined Sakuma-Hattori Planck II (SH Pl II) model, show higher resemblance with the Exp 2 model ($A = 1.79$) than with the SH Pl I model ($B = 1.18$).
The fitting quality of the respective model is estimated by the root mean squared error (RMSE) of the least square fit to the calibration function. Here the best fit is found for the SH Pl II model with a RMSE of 0.016, followed by the Exp 2 (RMSE= 0.152) and the SH Pl I (RMSE= 18.6) model. The goodness of fit for different models is visualized in figure 4.1. The Sakuma-Hattori Planck II model was therefore applied to express the radiometric correlation $S(T)$. By applying the Sakuma-Hattori Planck II formula, the radiometric model (equation 3.12) is further specified yielding

$$\begin{aligned} S_{\mathrm{IRcam}} = \tau_{\mathrm{w}}(1-\varepsilon_{\mathrm{obj}})\frac{\mathrm{C}T_{\mathrm{amb}}^{\mathrm{A}}}{e^{(\mathrm{B}/T_{\mathrm{amb}})} - \mathrm{D}} + \tau_{\mathrm{w}}\varepsilon_{\mathrm{obj}}\frac{\mathrm{C}T_{\mathrm{obj}}^{\mathrm{A}}}{e^{(\mathrm{B}/T_{\mathrm{obj}})} - \mathrm{D}} + \ldots \\ (1-\tau_{\mathrm{w}})\frac{\mathrm{C}T_{\mathrm{w}}^{\mathrm{A}}}{e^{(\mathrm{B}/T_{\mathrm{w}})} - \mathrm{D}} - \mathrm{C}\frac{\mathrm{T_E}^{\mathrm{A}}}{e^{(\mathrm{B}/\mathrm{T_E})} - \mathrm{D}}, \end{aligned} \tag{4.2}$$

with the Parameters $\mathrm{A} = 1.73$, $\mathrm{B} = 1786.9$, $\mathrm{C} = 0.269$ and $\mathrm{D} = -12$.

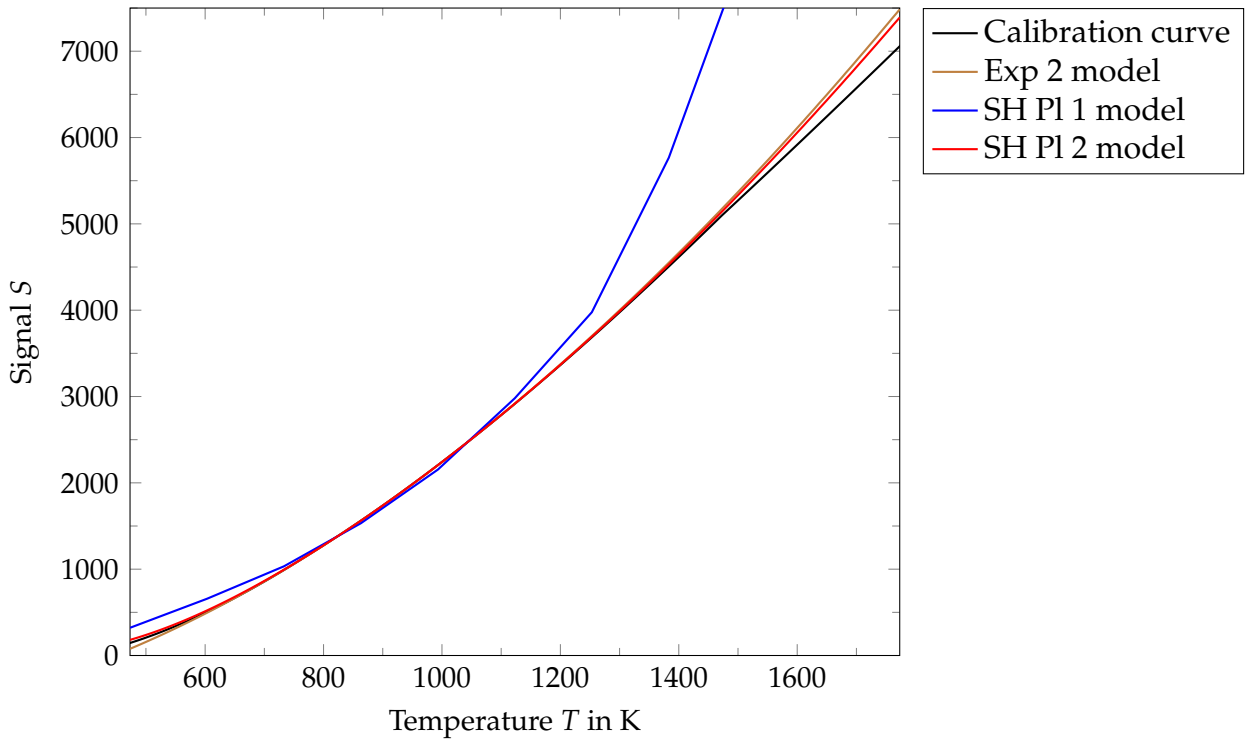

Figure 4.1.: Signal of the calibration curve (black) fitted in the range $T = 773.15...1023.15\,\mathrm{K}$ by the models Exp 2 (brown), SH Pl 1(blue) and SH Pl 2(red) over the temperature.

4.2. Identification of the focus effect

While carrying out the focus effect routine (3.4.2) raw images ($\varepsilon = 1$, $\tau = 1$) were recorded using the PIX Connect software. These images are displayed in figure 4.2. By adjusting the IR camera position at the maximum focal length, shown in figure 4.2a, the IR camera - blackbody distance of 0.42 m was obtained. At that distance, the focus effect routine is carried out by turning the ring for the focal distance adjustment respectively a half rotation (180°). The recorded images are shown consecutive from figure 4.2a to figure 4.2i. From figure 4.2a to figure 4.2f an increased blurred area at the edge of the blackblody aperture and a reduced focused area with constant temperature in the center is apparent. Couterintuitively, the area with constant temperature in the center seem to increase from figure 4.2f to figure 4.2i.
The raw data was here utilized to carry out the thermographic evaluation, shown in figure 4.3, with the displayed temperatures representing the maximum temperature value of the respective image. The image sequence follows from focused (image 1) to maximal defocused (image 9). The IR measured temperature shows

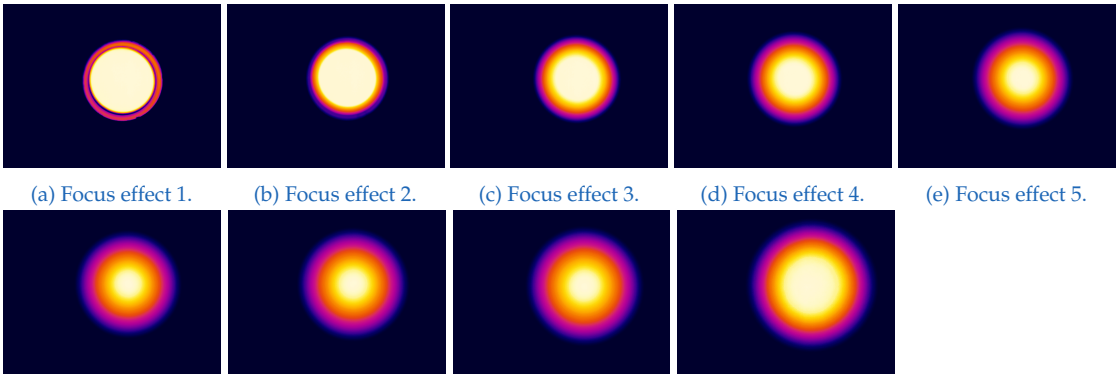

(a) Focus effect 1. (b) Focus effect 2. (c) Focus effect 3. (d) Focus effect 4. (e) Focus effect 5.

(f) Focus effect 6. (g) Focus effect 7. (h) Focus effect 8. (i) Focus effect 9.

Figure 4.2.: Focus effect routine at a distance $D = 0.42\,\mathrm{m}$.

a constant course from image 1 to image 6 at about 725 °C and then decreases from image 6 to image 9. Here the temperature difference of 25 K to the readout blackbody temperature of 700 °C arises from a non correction of the SSE (section 4.3). The temperature slope from image 6 to image 9 is assumed to result from the inaccurate setup (3.4.2) and can be eliminated by a bigger blackbody aperture. Due to the constant temperature measurement from figure 4.2a to figure 4.2f, the focus effect was stated to not be existent for the further experiments with subsequent focussing.

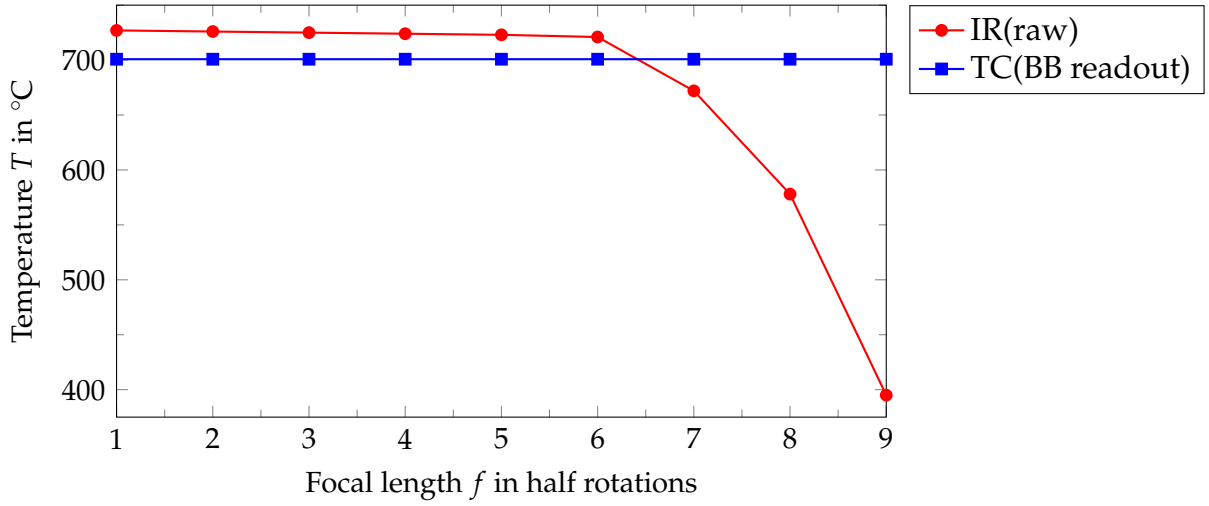

Figure 4.3.: IR measured and blackbody readout temperature as a function of focal length. The focal length is given in half rotations, its actual length can be calculated from the total focal length of 41.8 mm.

4.3. Recalibration of the size of source effect

The SSE routine, described in section 3.4.2 was applied from the minimal distance of 0.42 m (section 4.2), until a maximum distance of 6.5 m. The maximum distance was here defined by the minimum object FOV area of 3x3 pixel, given in the IR cameras data sheet (appendix B.1). Some of the raw thermographic images, recorded by the PIX Connect software are shown in figure 4.4. Here the recording distance increases from figure 4.4a to figure 4.4j. Slight inaccuracies of the focusing and aperture centering in the image are apparent, which may lead to small variations in the obtained results.
To correct for the blackbody emissivity ($\varepsilon_{BB} = 0.995$) (appendix B.2) the raw ther-

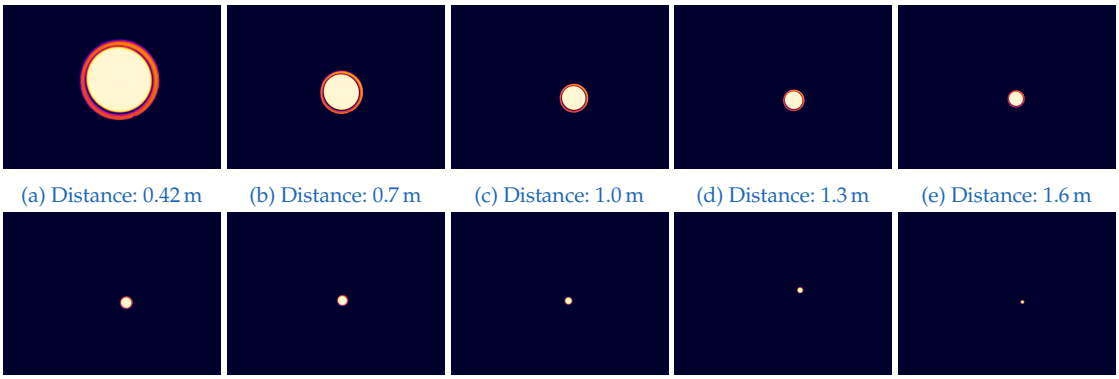

(a) Distance: 0.42 m (b) Distance: 0.7 m (c) Distance: 1.0 m (d) Distance: 1.3 m (e) Distance: 1.6 m

(f) Distance: 2.1 m (g) Distance: 2.4 m (h) Distance: 3.3 m (i) Distance: 4.1 m (j) Distance: 6.5 m

Figure 4.4.: Thermographic images of the size of source effect routine from a distance of 0.42 m until 6.5 m.

mographic data of each pixel was post-processed with the calibration curve and the radiometric model (equation 4.2). Due to the demounting of the protective window the radiometric model reduces to

$$S_{\mathrm{IRcam}} = (1-\varepsilon_{\mathrm{obj}})\frac{\mathrm{C}T_{\mathrm{amb}}^{\mathrm{A}}}{e^{(\mathrm{B}/T_{\mathrm{amb}})}-\mathrm{D}} + \varepsilon_{\mathrm{obj}}\frac{\mathrm{C}T_{\mathrm{obj}}^{\mathrm{A}}}{e^{(\mathrm{B}/T_{\mathrm{obj}})}-\mathrm{D}} - \mathrm{C}\frac{\mathrm{T_E}^{\mathrm{A}}}{e^{(\mathrm{B}/\mathrm{T_E})}-\mathrm{D}}. \tag{4.3}$$

To eliminate a focusing error, the maximum temperature values of the respective images were utilized and are shown in figure 4.5. The blackbody readout shows slightly higher temperatures ($\Delta T < 1\,\mathrm{K}$) at small distances. Measurements were here made while the transient phase was not yet finished. Beyond the distance of 2 m the blackbody readout were constant at 700 °C. With an increasing distance, a slope of the measured temperature is apparent. At the distance of 2.4 m, the measured temperature T_{IR} meets the blackbody temperature T_{BB} and the initial factory calibration angle $\theta_{cal} = 0.606°$ is found.

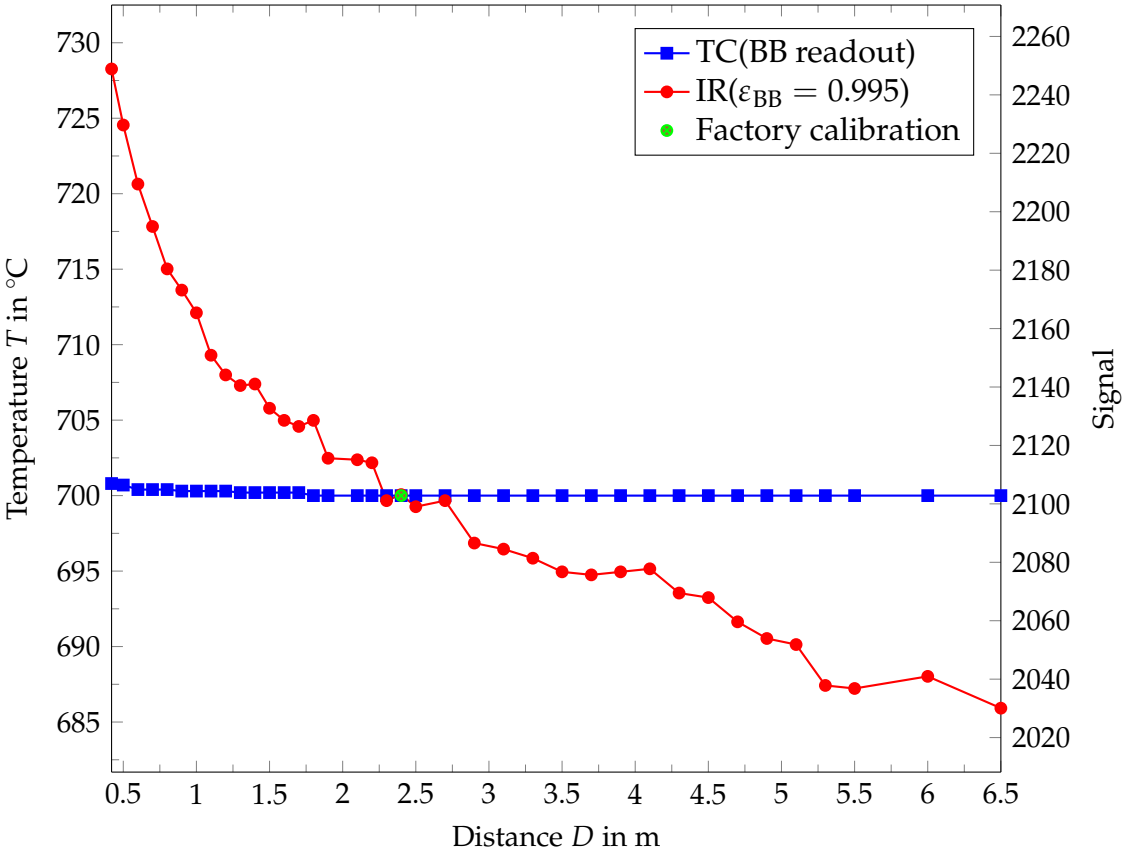

Figure 4.5.: Size of source effect. Temperature and signal as a function of the IR camera - object distance

To apply analytical representations by Bloembergen [45], the SSE quantity is calculated regarding equation 3.13 with the calibration signal S_{cal} and the equivalent blackbody diameter X is determined at the reference distance of 2.4 m ($SSE = 1$). This quantity X is further referred to as equivalent radiation source diameter. For the data of SSE over the equivalent radiation source diameter, the least square fit in Bloembergen [45] was found by the representation

$$SSE(X) = A_{BL} \cdot X^{n_{BL}} + C_{BL}, \tag{4.4}$$

with a root mean squared error of 0.00245. $A_{BL} = 0.34$, $n_{BL} = 0.20$ and $C_{BL} = 0.84$ are here the fitted Parameters and X the equivalent radiation source diameter at the 2.4 m distance. The measured data and the fitted representation are shown in figure 4.6. The maximum thermographic values of the raw images obtained in the SSE routine are used to show the radiometric correction in figure 4.7. Processed with the calibration curve, a maximum thermographic equivalent

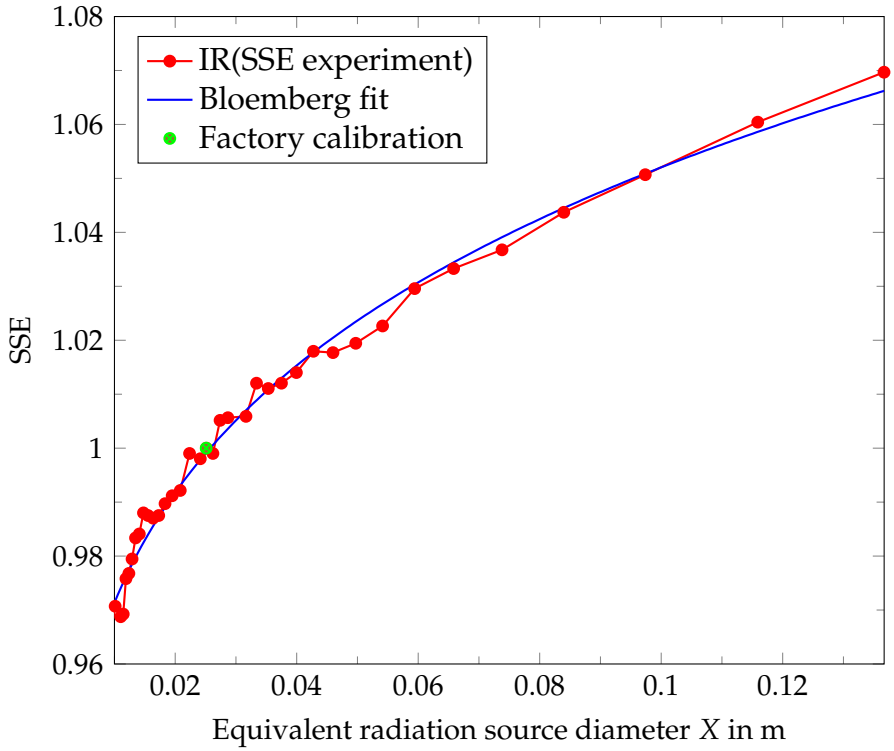

Figure 4.6.: *SSE* quantity (blue), measured with the SSE routine and representation $A_{\mathrm{BL}} \cdot X_{\mathrm{BL}}^{n} + C_{\mathrm{BL}}$ (red), from Bloembergen [45] as a function of the equivalent radiation source diameter X.

signal (blue) is determined. Applying equation 4.3, a radiometric ($\varepsilon_{\mathrm{obj}} = 0.995$) corrected temperature, i.e. signal (red) is calculated. After correcting the size of source effect with equation 3.13, signals related to the calibration distance (brown) are obtained.

4.4. Estimation of the protective window's transmissivity

To estimate the transmissivity of the protective window, the SSE routine was repeated with the window mounted in front of the IR camera. Due to restriction of the focal length by the assembly of the window, the shortest measured distance was here 0.7 m instead of the prior reported 0.42 m. The obtained camera signal with the mounted window $S_{\mathrm{IRcam}}(\mathrm{Window})$ and the prior (section 4.3) calculated camera signal without the window $S_{\mathrm{IRcam}}(\mathrm{No\ Window})$ did then only deviate by

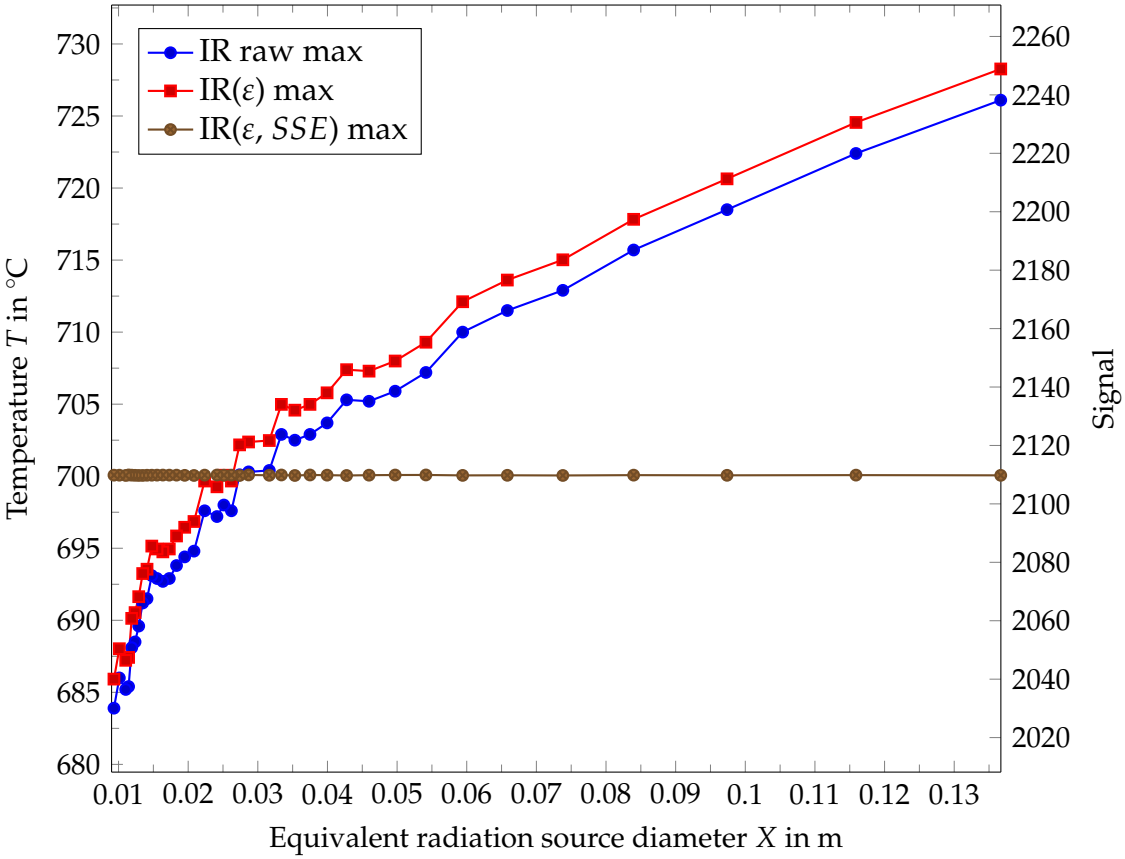

Figure 4.7.: Radiometric correction of maximum thermographic data, respective to raw images of the SSE routine. Temperature and radiometric signal of the raw (blue), radiometric corrected (red) and SSE corrected (brown) values over the equivalent radiation source diameter X.

the influence of the window. $S_{\mathrm{IRcam}}(\mathrm{Window})$ was here expressed under the condition of the mounted window with the whole radiometric model (equation 4.2) while $S_{\mathrm{IRcam}}(\mathrm{No\,Window})$ was expressed regarding equation 4.3. Subtracting the expression for $S_{\mathrm{IRcam}}(\mathrm{Window})$ from those of $S_{\mathrm{IRcam}}(\mathrm{No\,Window})$, rearranging and inserting the expression for $S_{\mathrm{IRcam}}(\mathrm{No\,Window})$ yields

$$\tau_{\mathrm{w}} = 1 - \frac{S_{\mathrm{IRcam}}(\mathrm{No\,Window}) - S_{\mathrm{IRcam}}(\mathrm{Window})}{S_{\mathrm{IRcam}}(\mathrm{No\,Window}) - \frac{\mathrm{CT_w}^{\mathrm{A}}}{e^{(\mathrm{B}/\mathrm{T_w})} - \mathrm{D}} - \frac{\mathrm{CT_E}^{\mathrm{A}}}{e^{(\mathrm{B}/\mathrm{T_E})} - \mathrm{D}}}. \tag{4.5}$$

The temperature of the window $\mathrm{T_w}$ was estimated as 20 °C, i.e. 293.15 K. Together with the parameter A, B, C, D and $\mathrm{T_E}$ from table 4.1 and the measured quantities $S_{\mathrm{IRcam}}(\mathrm{No\,Window})$ and $S_{\mathrm{IRcam}}(\mathrm{Window})$, the transmissivity of the window was calculated according to equation 4.5. The result is shown in figure 4.8 with

the average of 92.13 %. Along greater equivalent radiation sources, a slightly decreasing trend of the transmissivity is evident. Reasons for this course may be related to the prior discussed blackbody temperature stability (figure 4.5), or due to the variation of incident radiation angles on the protective window. Reflective effects, or spatial variations of the transmissivity on the protective window might be relevant. With the initial calibration of the IR camera at the factory calibration angle θ_{cal}, i.e. $X_{cal} = 0.0251\,\mathrm{m}$, its transmissivity value, given as 92.28 %, should be minor effected by errors. Hereof and with the average value, a window transmissivity $\tau_w = 0.922$ was estimated.
The roughly estimated 1.3 % influence of the window radiation in section 3.2.2 reduces with the inclusion of the transmissivity to $545.28 \cdot 0.078/(41181.32 \cdot 0.922) \approx 0.11\,\%$. On the one side, this rough calculation was carried out utilizing the Stefan-Boltzmann law, which result in an slight underestimation of the window radiation. On the other side, the window was assumed to not reflect any radiation ($\rho = 0$). From equation 2.16 this results in an overestimation of the window emissivity ε_w and thus the window radiation.
Due to the uncertainties and the small estimated influence of $\approx$ 0.11 %, the radiation of the protective window was neglected in the further calculations of the radiometric model, which is then given as

$$S_{\mathrm{IRcam}} = \tau_w(1-\varepsilon_{obj})\frac{C T_{amb}^{A}}{e^{(B/T_{amb})} - D} + \tau_w \varepsilon_{obj}\frac{C T_{obj}^{A}}{e^{(B/T_{obj})} - D} - C\frac{T_E{}^{A}}{e^{(B/T_E)} - D}. \quad (4.6)$$

The correction of the infrared measured raw values is shown in figure 4.9.

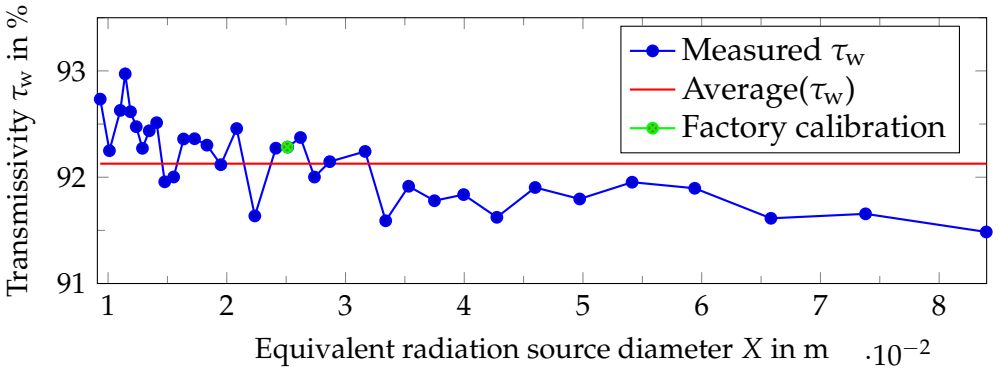

Figure 4.8.: Transmissivity of the protective window and its mean value as a function of the equivalent radiation source diameter X.

The raw temperatures, i.e. signals (red) are processed with the same correction steps as in section 4.3, to obtain a comparable signal (brown). Utilizing the full radiometric model (equation 4.2) the signal is corrected for the protective

window transmissivity (black). In comparison the signal results of recalibrated SSE routine (blue) are shown.

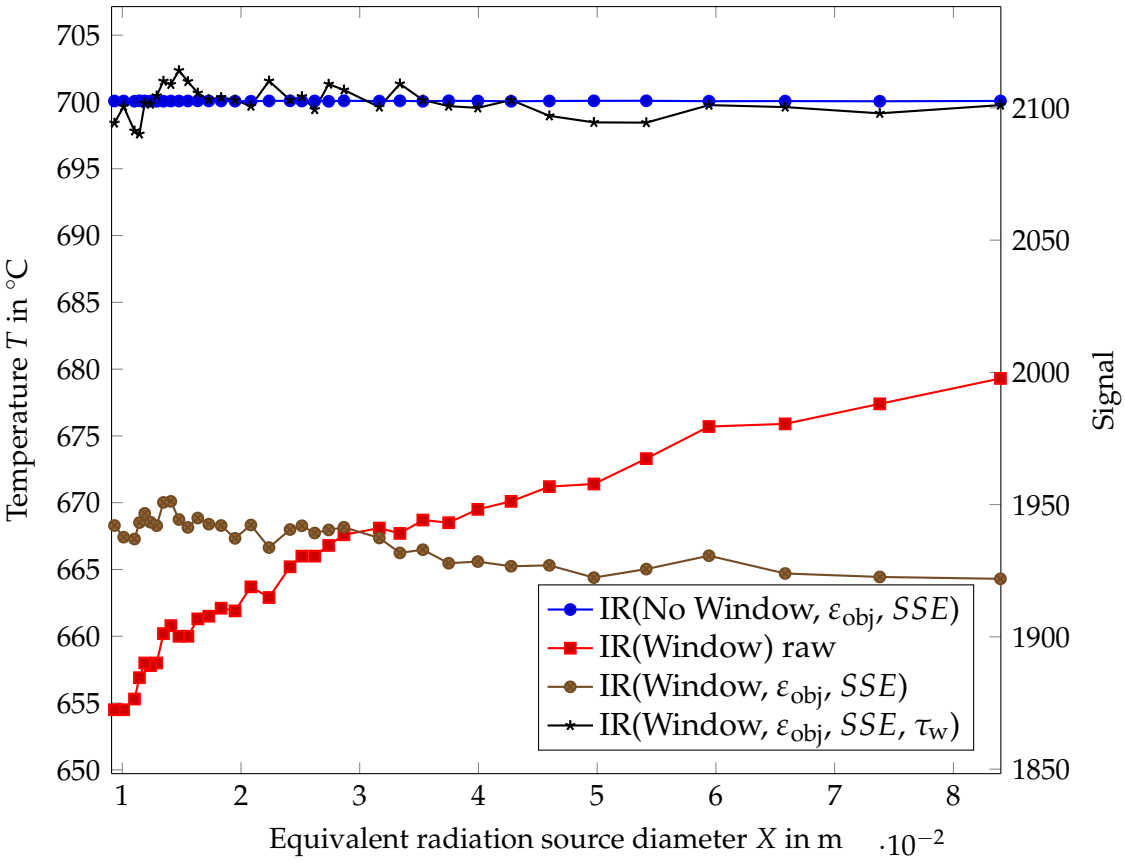

Figure 4.9.: Measured and corrected radiometric data with and without a protective window. Temperature and radiometric signal of raw (red), radiometric corrected (brown) and SSE corrected (black) values over the equivalent radiation source diameter X. For comparison, corrected values recorded without the protective window (blue) are also shown.

4.5. Validation of the SSE's temperature independence

Measurements with the blackbody model Mikron M335 were carried out to test the temperature independence of the SSE. A data sheet of this model was not available for this model, however the model was stated by the manufacturing

company to be similar to the M330 model (appendix B.3). The emissivity of the M335 blackbody was estimated to be $\varepsilon_{BB} = 0.990$ and the aperture radius was given as $r_{BB} = 8.25\,\text{mm}$. Five temperatures of 500 °C, 550 °C, 600 °C, 650 °C and 700 °C were measured under conditions of equivalent radiation source diameters 0.059 m, 0.049 m, 0.0395 m and 0.0263 m. The results, obtained with the radiometric model (equation 4.2) are shown in figure 4.10. The IR measured raw values show an increasing behavior along greater equivalent radiation source diameters X due to the SSE. After the radiometric correction of the IR measurements, they estimate the blackbody temperatures very accurately. Despite one outlier at the $T = 700\,°\text{C}$, $X = 0.0395\,\text{m}$ measurement, the deviations between blackbody readout and corrected IR measurement were smaller than 5 K. Furthermore no trend along with variations in temperature was apparent. However it should be noted, that the accuracy depends highly on the emissivity. An emissivity deviation of 1 % results here approximately in an 4 K offset.

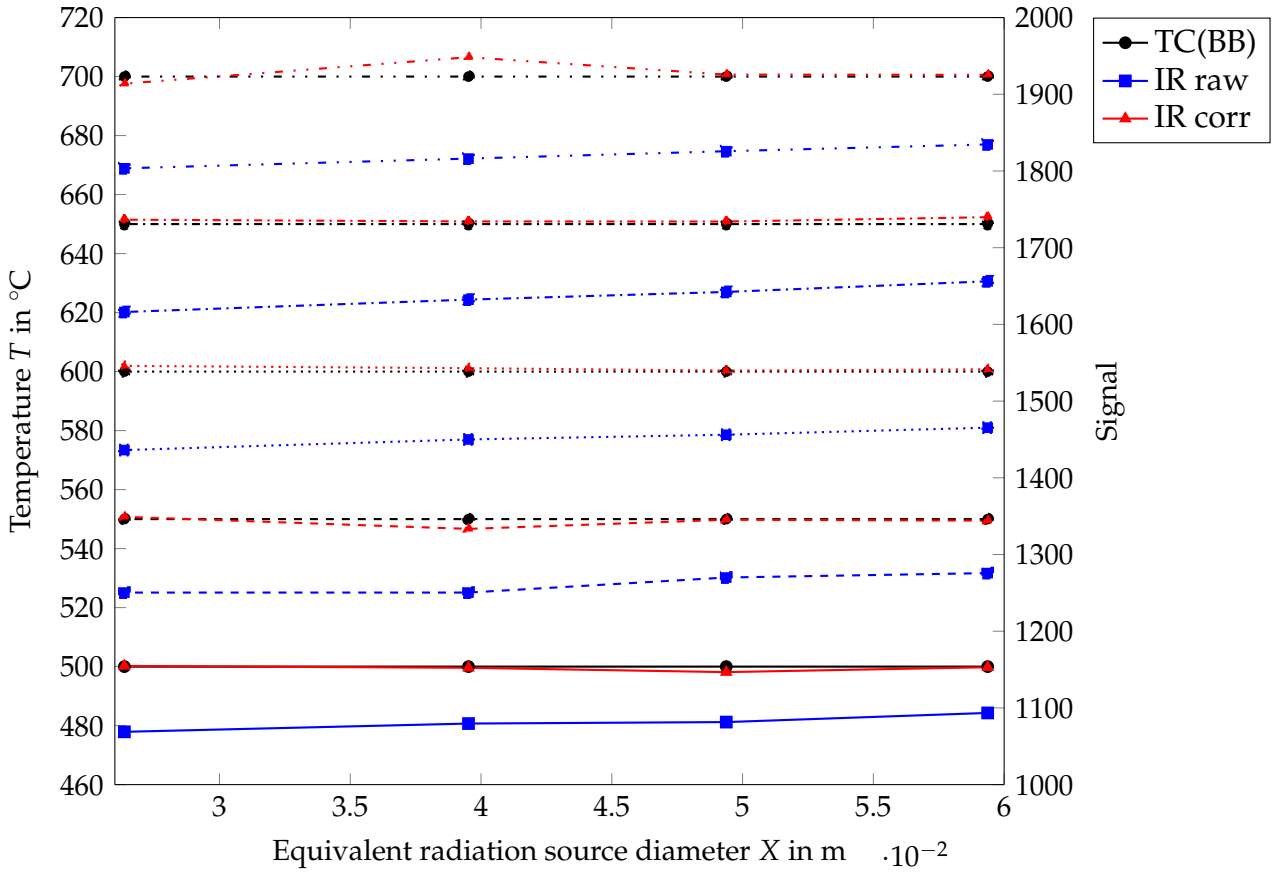

Figure 4.10.: Temperature and signal values for the blackbody readout (black), raw IR measurement (blue) and corrected IR measurement (red) of the Mikron M335 blackbody over the equivalent radiation source diameter X. Values related to the temperatures 500 °C, 550 °C, 600 °C, 650 °C and 700 °C are represented by solid, dashed, dotted, dashdotted and dashdotdotted lines.

4.6. Validation of the radiometric model with a real body experiment

The objective in this next validation experiment, was to measure a real body and thus follow a routine similar to temperature measurements at the solar dish facility. This experiment allows to determine the band emissivity of a coated metal plate. Furthermore the radiation source apertures are manufactured in greater sizes than those of the blackbodies, which made a validation of the Bloemberg fit for greater equivalent radiation source diameters possible.
The experiment was evaluated for three temperatures, 500 °C, 550 °C and 600 °C at five equivalent radiation source diameters of 0.3 m, 0.1 m, 0.086 m, 0.075 m and 0.06 m through a 0.125 m aperture and at further five equivalent radiation source diameters of 0.35 m, 0.12 m, 0.1 m, 0.087 m and 0.07 m through a 0.145 m aperture. Higher temperatures could not be obtained, since substrate for the welding of the thermocouples does not withstand temperatures above 625 °C. Besides the IR measurement, the temperature of the plate was also measured with four thermocouples welded on the surface of the plate. Due to the metallic based welding substrate, a good thermal conduction from the plate to the thermocouple was achieved. The positioning of these thermocouples is shown in the exemplary thermographic image 4.11 ($T = 500\,°C$, $X = 0.35\,m$) next to the four measuring points. Especially the non welded part of the thermocouples is here shown in a darker color, representing lower temperatures.

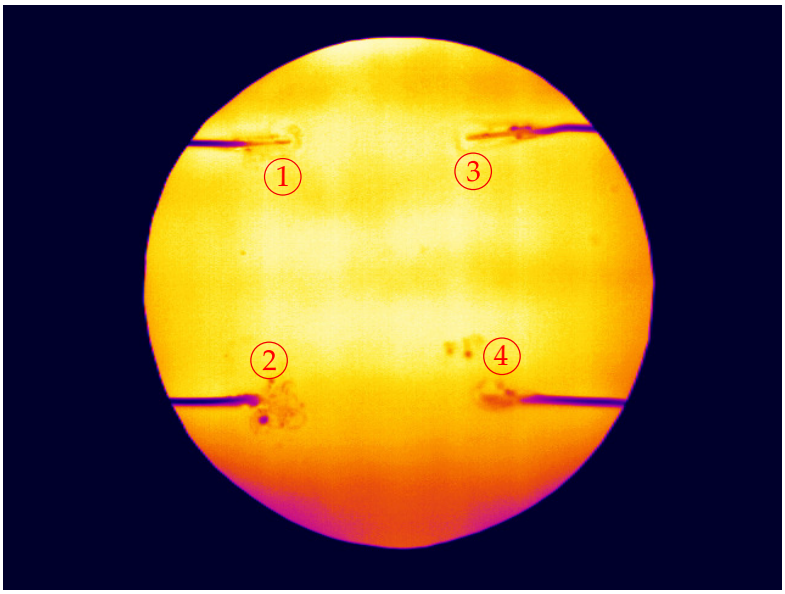

Figure 4.11.: Thermographic image of the 1 m distant heated plate at $T = 500\,°C$ through the 145 mm Aperture. The plate is measured at four points (1, 2, 3, 4) by thermocouples and the IR camera.

Despite of the bottom of the aperture, the temperature profile was homogeneous with slight stripe shaped irregularities, due to the spraying and width of the paint. Artifacts, resulting from the welding process are apparent at the bottom thermocouples at measuring positions 2 and 4. Due to these artifacts and the better homogeneity of the temperature profile around the thermocouples at the measuring positions 1 and 3, thermal data of the thermocouples at the measuring positions 2 and 4 were discarded for the evaluation.
Utilizing the APTSEG script (section 3.4.5), similar geometrical areas were chosen on the raw IR images for the evaluation, shown in figure 4.11 as the measuring points. The average and the maximum values of these evaluation areas were then measured. The average IR and thermocouple temperature, resp. signal measurements are shown in figure 4.12 for the 0.125 m aperture and in figure 4.13 for the 0.145 m aperture.

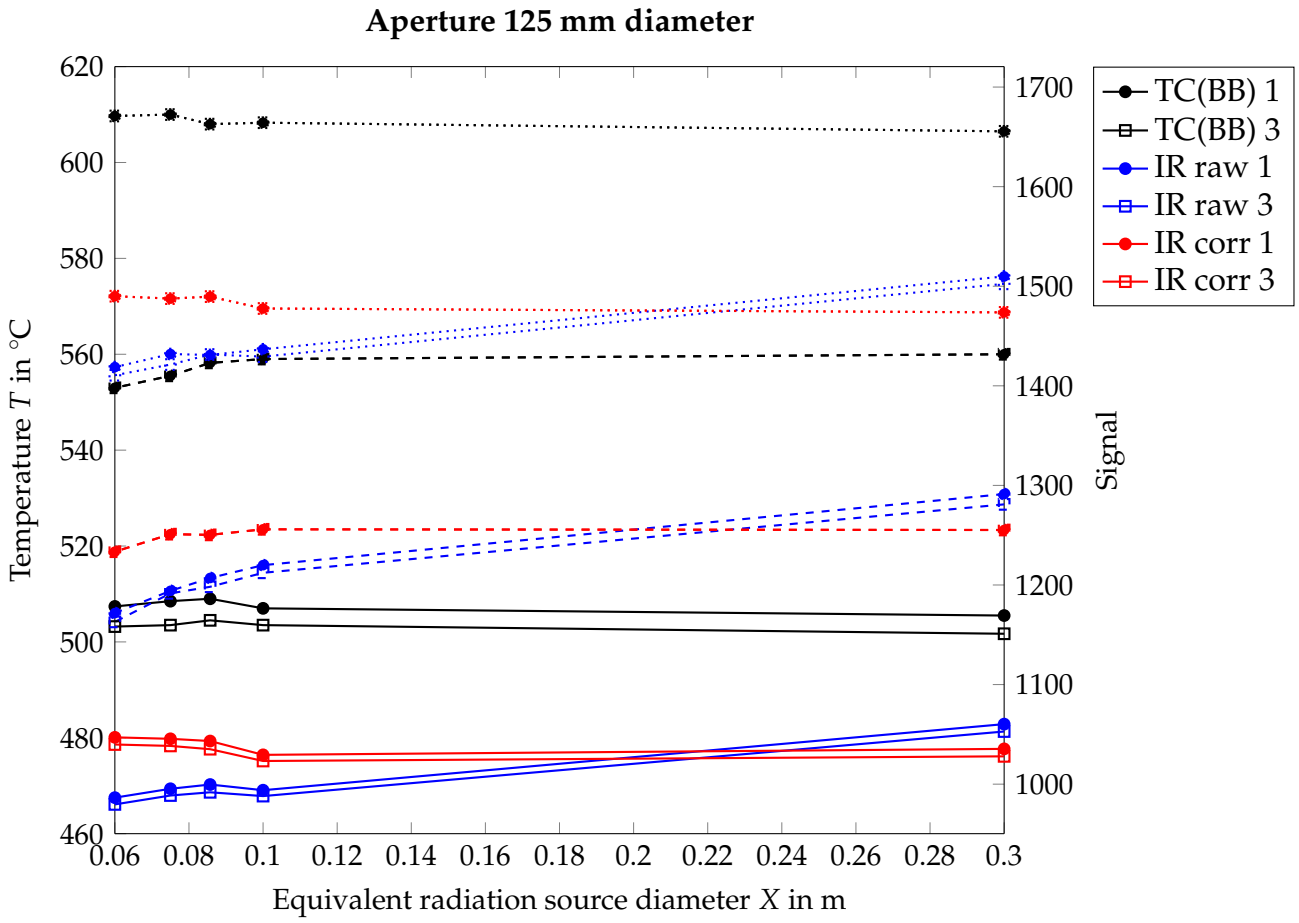

Figure 4.12.: Temperature and signal of the thermocouple (black), raw IR (blue) and corrected IR measurement (red) of the heated plate through the 125 mm aperture at measurement position 1 (circle) and 3 (square) over the equivalent radiation source diameter X. Values related to the temperatures 500 °C, 550 °C and 600 °C are represented by solid, dashed and dotted lines.

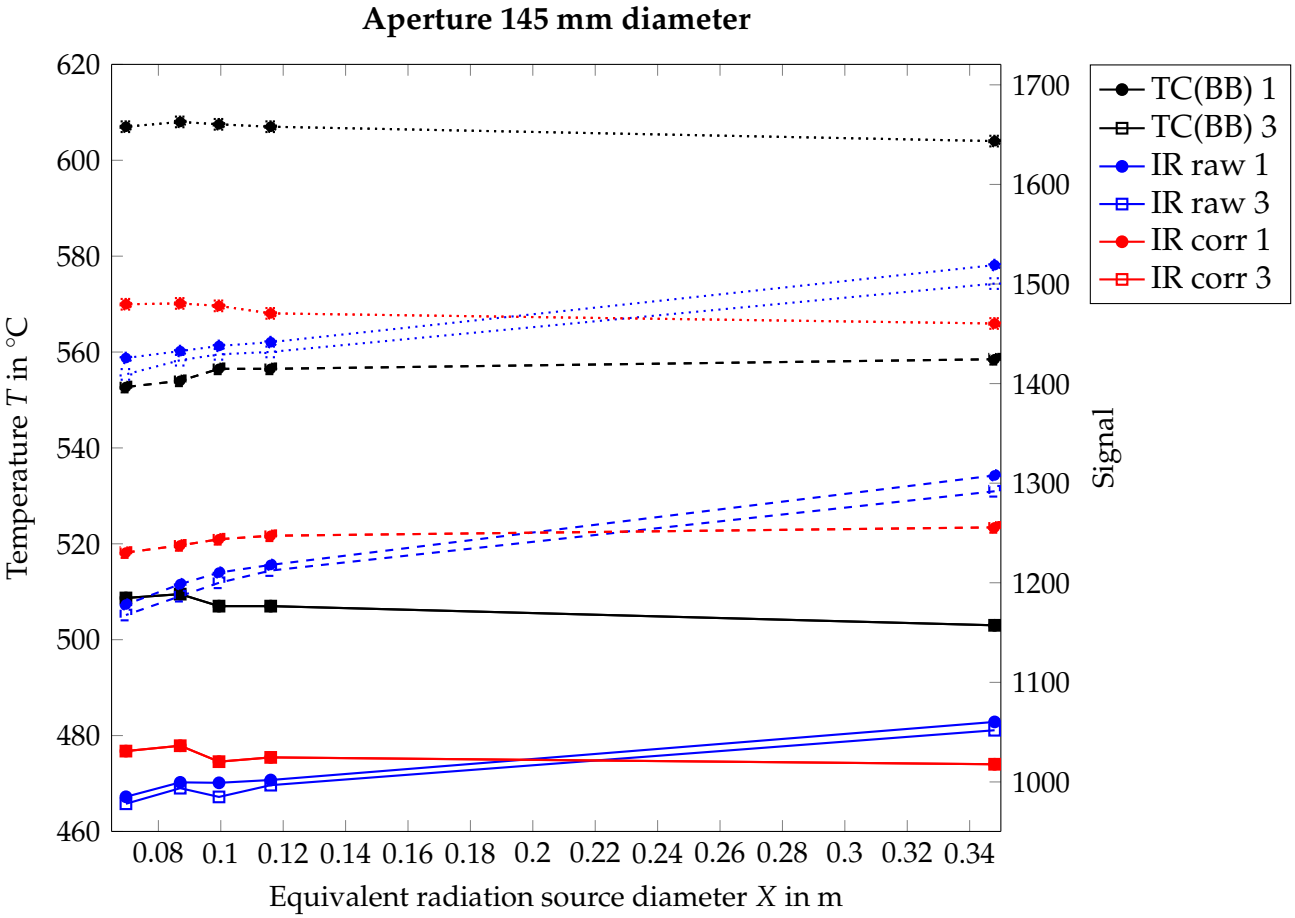

Figure 4.13.: Temperature and signal for the thermocouple (black), raw IR (blue) and corrected IR measurement (red) of the heated plate through the 145 mm aperture at the measurement position 1 (circle) and 3 (square) over the equivalent radiation source diameter X. Values related to the temperatures 500 °C, 550 °C and 600 °C are represented by solid, dashed and dotted lines.

For the correction of the raw values the SSE correction and the radiometric model from equation 4.6 was used with an emissivity $\varepsilon = 1$, yielding

$$S_{\mathrm{IRcam}} = \tau_{\mathrm{w}} \frac{\mathrm{C} T_{\mathrm{obj}}^{\mathrm{A}}}{e^{(\mathrm{B}/T_{\mathrm{obj}})} - \mathrm{D}} - \mathrm{C} \frac{\mathrm{T_E}^{\mathrm{A}}}{e^{(\mathrm{B}/\mathrm{T_E})} - \mathrm{D}}. \tag{4.7}$$

The difference between the correctly measured thermocouple temperature and the corrected IR temperature is accounted for by the incorrect emissivity setting of ($\varepsilon = 1$). To calculate this emissivity, the radiometric model (equation 4.6) was

rearranged, yielding

$$\varepsilon = \frac{S_{\mathrm{IRcam}}(SSE) - \tau_{\mathrm{W}} \frac{\mathrm{C}T_{\mathrm{amb}}^{\mathrm{A}}}{e^{(\mathrm{B}/T_{\mathrm{amb}})} - \mathrm{D}} + \mathrm{C} \frac{{\mathrm{T_E}}^{\mathrm{A}}}{e^{(\mathrm{B}/\mathrm{T_E})} - \mathrm{D}}}{\tau_{\mathrm{W}} \frac{\mathrm{C}T_{\mathrm{obj}}^{\mathrm{A}}}{e^{(\mathrm{B}/T_{\mathrm{obj}})} - \mathrm{D}} - \tau_{\mathrm{W}} \frac{\mathrm{C}T_{\mathrm{amb}}^{\mathrm{A}}}{e^{(\mathrm{B}/T_{\mathrm{amb}})} - \mathrm{D}}}, \tag{4.8}$$

where $S_{\mathrm{IRcam}}(SSE)$ is the SSE corrected signal value of the IR camera and T_{obj} the actual object temperature, measured by the thermocouples. The obtained results from equation 4.8 are shown in figure 4.14 and 4.15 over the temperature for a mean evaluation of the measuring areas in the APTSEG script.

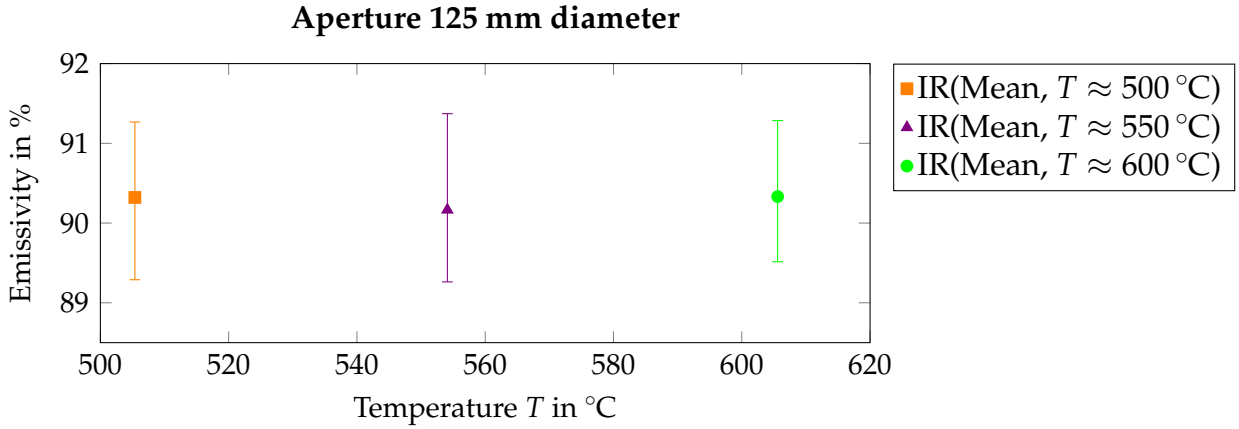

Figure 4.14.: Aperture with 125 mm diameter: Measured emissivities of all distances pooled in a error bar for the temperatures $T \approx 500\,^{\circ}\mathrm{C}$ (orange), $T \approx 550\,^{\circ}\mathrm{C}$ (violet) and $T \approx 600\,^{\circ}\mathrm{C}$ (green).

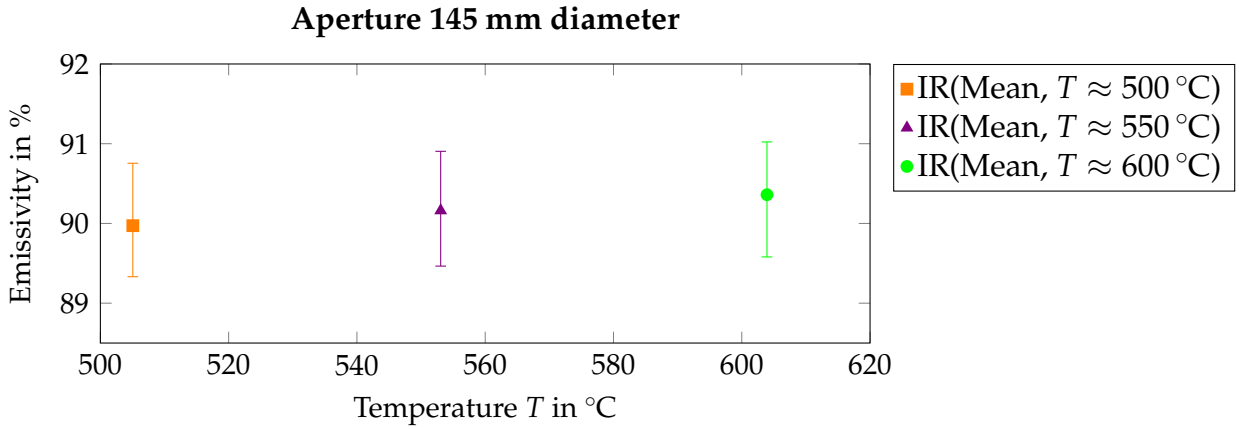

Figure 4.15.: Aperture with 145 mm diameter: Measured emissivities of all distances pooled in a error bar for the temperatures $T \approx 500\,^{\circ}\mathrm{C}$ (orange), $T \approx 550\,^{\circ}\mathrm{C}$ (violet) and $T \approx 600\,^{\circ}\mathrm{C}$ (green).

The emissivities are scattered between 89 and 91.5 %. A trend along the temperature, shown on the x-axis, or degradation effects are not apparent. Average emissivity values were therefore calculated to estimate the coating band emissivity. For the 0.125 m aperture, the mean measured values resulted in averages of $\varepsilon_{\text{mean}} = 90.27\,\%$. Similarly, for the 0.145 m aperture, the mean measured values resulted in averages of $\varepsilon_{\text{mean}} = 90.16\,\%$. To account for the variation in paint width, emissivities were calculated with the maximum temperatures of the measuring area. Here the average of the maximum measured emissivity of the 0.125 m aperture yielded $\varepsilon_{\text{max}} = 90.88\,\%$. For the 0.145 m aperture, an average of the maximum measured emissivity of $\varepsilon_{\text{max}} = 90.72\,\%$ was calculated. The measurements were therefore found to be independent on the aperture size. The difference between mean $\varepsilon_{\text{mean}}$ and maximum ε_{max} measured emissivity is found to be $\Delta\varepsilon \approx 0.6\,\%$ and assumed to result from the spatial irregularities, due to the spraying and coating thickness. The emissivity of the colored plate was therefore estimated to be $\varepsilon = 90.22 \pm 0.6\,\%$. To validate this finding, flat metal samples of inconel 625 steel painted with the MACOTA (Model: 08008) paint were analyzed with the Perkin Elmer Frontier-FTIR spectrophotometer (section 3.2.3, appendix B.4).

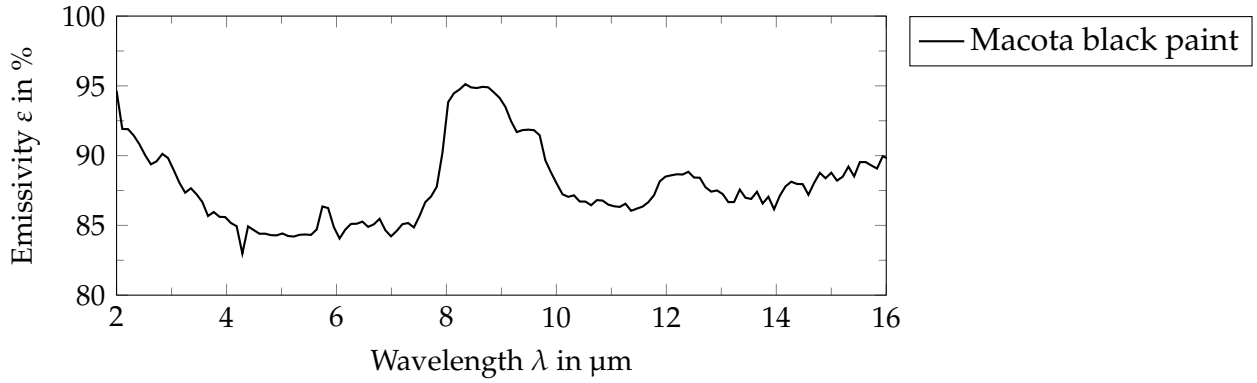

(a) Emissivity over the whole wavelength.

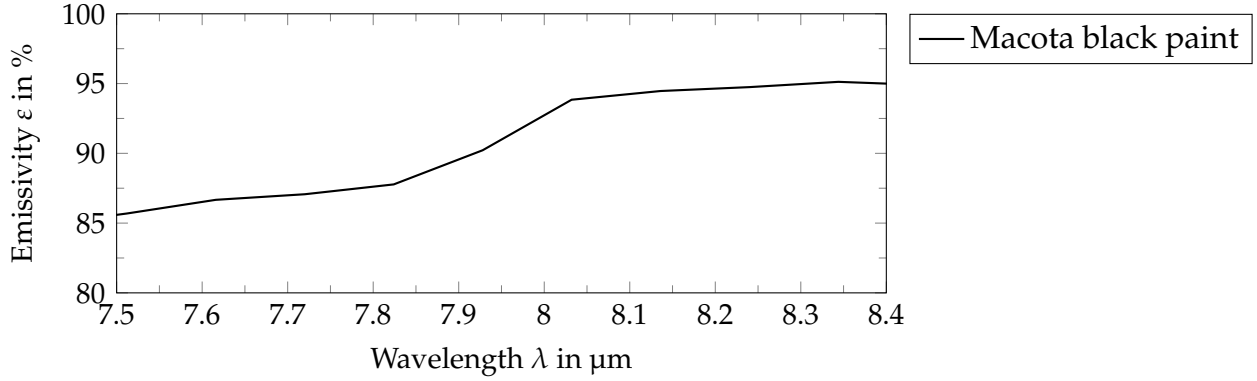

(b) Emissivity in the wavelength range of the IR camera.

Figure 4.16.: Emissivity of Macota 08008 black paint as a function of wavelength.

Temperature in °C	500	550	600	650	700	750	800
Emissivity(sample A) in %	90.59	90.58	90.57	90.56	90.55	90.55	90.54
Emissivity(sample B) in %	90.58	90.57	90.56	90.55	90.54	90.54	90.53
Emissivity(sample C) in %	90.29	90.28	90.27	90.26	90.25	90.24	90.23
Emissivity(sample D) in %	90.65	90.64	90.63	90.62	90.61	90.61	90.60
Average in %	90.53	90.52	90.51	90.50	90.49	90.48	90.48
Standard deviation in %	0.16	0.16	0.16	0.16	0.16	0.16	0.16

Table 4.2.: Findings of the Photospectroscopy: Averaged emissivities in the wavelength bandwidth of the IR camera PI640G7 from inconel 625 samples A, B, C, D painted with MACOTA (Model:08008) paint. The result is weighted with blackbody radiation of temperatures from 500 °C to 800 °C. Further averages between the samples and standard deviations are given.

The emissivity, obtained from the reflectivity as $\varepsilon = 1 - \rho$ is shown in figure 4.16a over the whole spectrum and in figure 4.16b over the IR camera respective bandwidth. Over the whole spectrum the sample can be characterized as a grey body, with a peak between 8 and 9.5 µm. Unfortunately, a part of this peak lies in the IR camera spectrum of $7.55\,\mu\text{m} < \lambda_{\text{IRcam}} < 8.35\,\mu\text{m}$. The emissivity increases here from 86 % at $\lambda = 7.55\,\mu\text{m}$ to 95 % at $\lambda = 8.35\,\mu\text{m}$. To eliminate a thermal dependence due to this selectivity, spectrophotometric measurements are analyzed with additional weighting for temperatures in the respective range. The results of the photospectroscopy are shown in table 4.2. The average emissivity in the bandwidth of the IR camera is presented for four samples A, B, C and D, weighted with seven temperatures from 500 °C to 800 °C. A small temperature dependence, resulting from the shift of the peak spectral radiation, described by Wien's law is observed in the average emissivity between the four samples. However, due to a difference of $\Delta\varepsilon = 0.05\,\%$ from 500 to 800 °C, this effect is neglected. Therefore an average emissivity of $\varepsilon_{\text{spec}} = 90.50\,\%$ is obtained. Since this value agrees very well with the emissivity obtained from the IR measurements of $\varepsilon_{\text{IRcam}} = 90.22\,\% \pm 0.6\,\%$, the validation of the radiometric model was successful.
Furthermore an extrapolation of the Bloemberg fit is investigated from the greater equivalent radiation source diameters X of the 0.125 m and 0.145 m apertures at the short distances D of 1 and 3 m. A non SSE corrected signal value from the IR measurement was related to the thermocouples temperature value, to obtain a SSE quantity for that measurement. The SSE quantities of the four

measurements are shown in figure 4.17 together with the Bloemberg fit over the equivalent radiation source diameter. Where the two SSE quantities represent

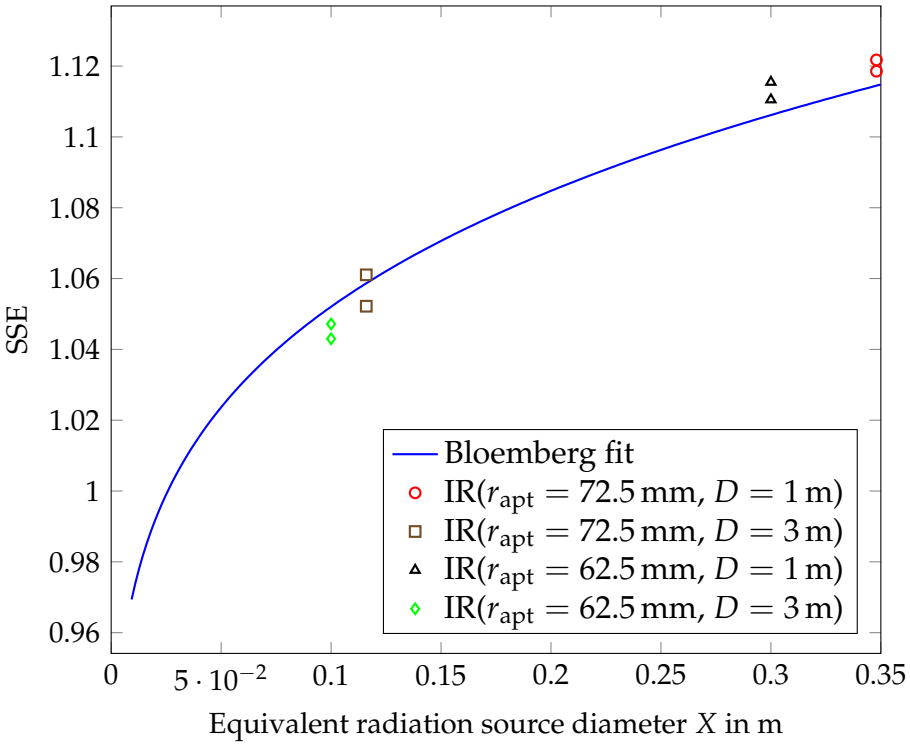

Figure 4.17.: SSE quantities from plate measurements and the fitted representation from Bloembergen (blue) over the equivalent radiation source diameter X. Shown plate measurements are obtained at 500 °C with an 145 mm aperture at 1 m (red) and 3 m (brown) and with an 125 mm aperture at 1 m (black) and 3 m (green)

the two measuring points, i.e. thermocouples 1 and 3. Due to the singularity of the measurement, an interpretation is restricted and a scattering of the SSE quantities evident. From the shown results however, a good agreement with the Bloemberg fit is apparent.

4.7. IR measurements at the solar dish facility

To test the functionality of the IR measuring method, two thermographic images of different measurement campaigns were evaluated and the results were compared to thermocouple measurements. The routine of the temperature evaluation involves the recording of the thermographic image at the dwelling phase of a thermal cycle, the photospectroscopic measurement of the samples emissivity

and the evaluation of the thermographic image. Samples with a varying, e.g. degrading coating emissivity over time are hardly evaluated, since the emissivity measurement is carried out only after every 25th cycle. Here the image of the dish campaign 1 is taken at the 12th thermal cycle, while the image of the dish campaign 2 is taken at the 20th thermal cycle. The name of the sample, defining the particular substances of the steel and coating is further colored in cyan. The enumeration of the samples for one particular setup at the solar dish test bench follows figure 3.2, described in section 3.1.1.

Dish campaign 1

In this section the evaluation of the first measurement campaign, with the respective tubular coated samples shown in figure 4.18 is discussed.

Figure 4.18.: Center samples 79, 82, 77, 89 and 78 bevore the start of the dish campaign 1, mounted at the dish test bench.

The strings of samples are here coated with paint applied by spraying, while the string of sample 78 is a sandblasted, uncoated sample. The photospectroscopic results after the 25th thermal cycle of the center samples 79, 82, 77 and 89 is shown in figure 4.19 for the whole spectral range and in figure 4.20 for the spectral range of the IR camera. Despite the uncoated sample 78, all samples

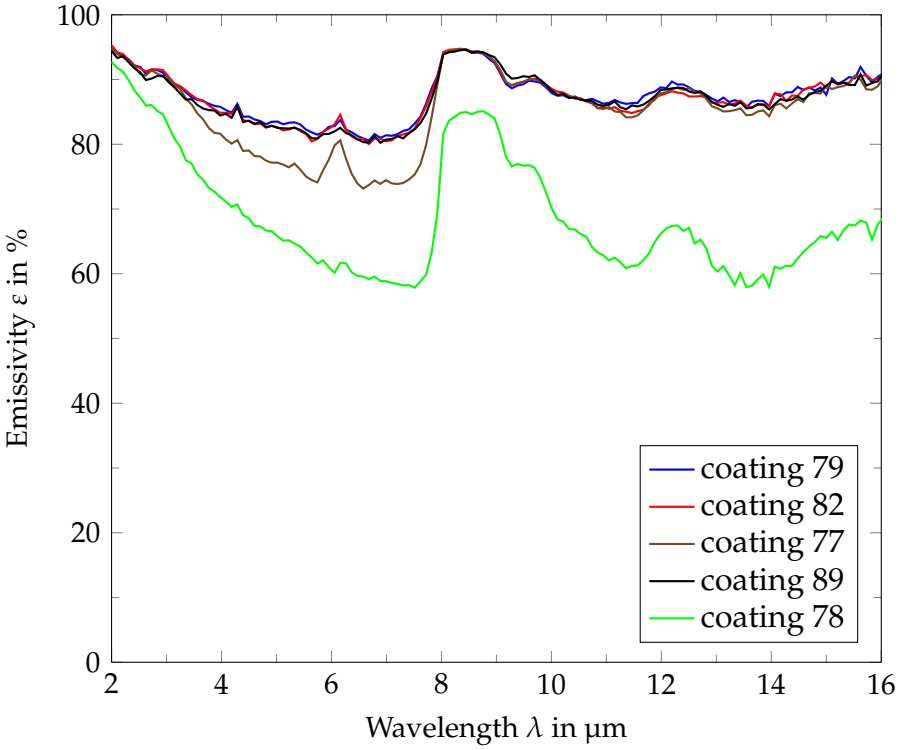

Figure 4.19.: Emissivity of center coatings 79, 82, 77, 89 and 78 as a function of wavelength.

show constant emissivities at 85 % ± 10 % with a peak between 7.8 and 9.3 µm. The uncoated sample shows a similar course, shifted towards lower emissivities at about 65 %. The emissivity peak is further represented as an incline in the spectral range of the IR camera (figure 4.20) and accounted for by the weighting with equation 3.10. The averaged results over the spectral range of the IR camera are shown for all samples in table 4.3. Moreover, the thermographic image to be evaluated is shown in figure 4.21. From the postprocessing, an ceramic area of 29439 pixel and a samples area of 6764 pixel was calculated. To apply the SSE correction, it was here assumed that the star shaped radiation source agrees reasonably well with a circular shape. Thus an equivalent radius of 0.22 m and an equivalent radiation source diameter of $X = 0.2113\,\mathrm{m}$ was calculated from the total area $A_f = 0.15\,\mathrm{m}^2$, focused by the dish. Since a great part of the apparent radiation source is illuminated ceramic at higher temperatures than the samples

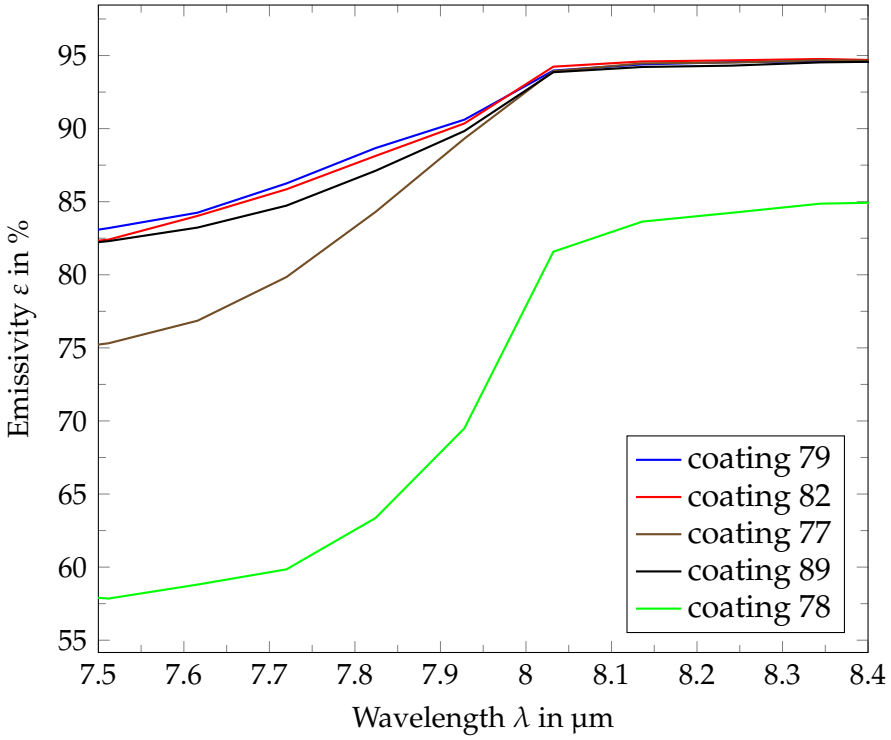

Figure 4.20.: Emissivity of center coatings 79, 82, 77, 89 and 78 as a function of wavelength range of the IR camera.

$T_{\text{samples}} < T_{\text{ceramic}}$, the signal to which the SSE correction is applied is adjusted by equation 3.15. Here the ceramic signal value is corrected with an emissivity of 90 %, estimated from [46]. To analyze the influence of this effect, the further called method 1 calculates the SSE correction by wrongly assuming same ceramic and sample temperatures $T_{\text{samples}} = T_{\text{ceramic}}$, while the further called method 2 utilizes the weighted average of sample and ceramic temperature, i.e. signal (equation 3.15). The findings of postprocessing the thermographic image are then shown in figure 4.22 over the sample enumeration. A sample is measured here with a 3x3 pixel area, applied to the position of the thermocouple. The

sample	**1**	**2**	**3**	**4**	**5**	**6**	**7**	**8**
Emissivity in %	90.09	90.26	88.33	89.48	89.87	90.41	89.49	88.72
sample	**9**	**10**	**11**	**12**	**13**	**14**	**15**	
Emissivity in %	89.71	88.22	89.68	89.50	69.31	71.07	69.33	

Table 4.3.: Photospectroscopic emissivity measurements of the dish campaign 1 samples from position 1 to 15, regarding figure 3.2.

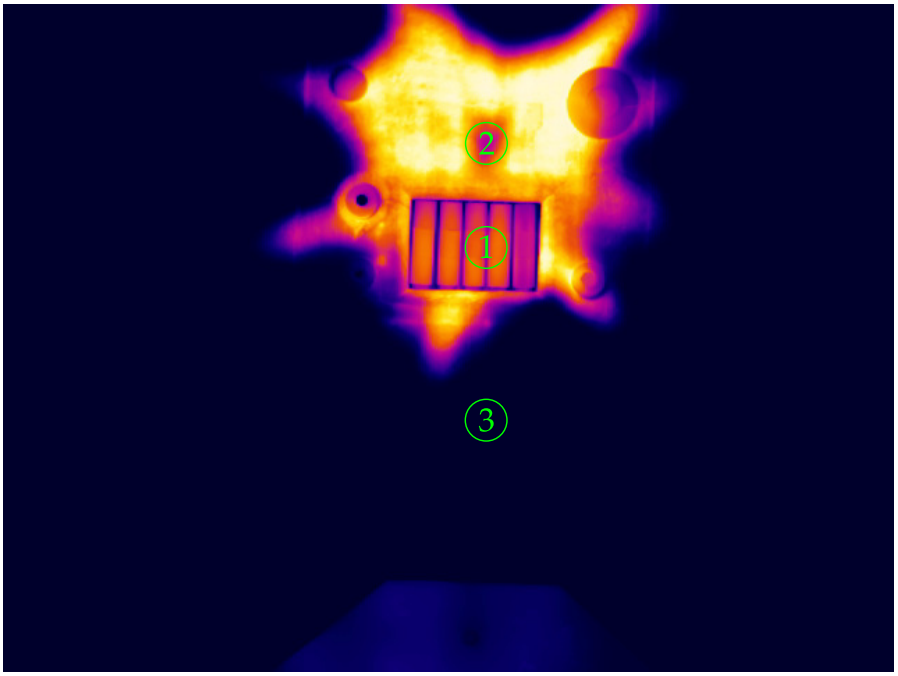

Figure 4.21.: Thermographic raw image at dish campaign 1. Tubular coated absorber samples (1) in the center, surrounded by heated ceramic (2). Remaining non heated ceramic and other environment (3) is not visible.

presented methods are selected regarding the SSE, since it was assumed to cause the greatest uncertainty and is not implemented in the IR camera software PIX Connect. Thus, despite the thermocouple measurement, one method without SSE correction, the prior described method 1 and method 2 SSE correction are displayed in different colors. Furthermore each string of samples is displayed by a different marker type.
Generally the IR measurements in figure 4.22 show greater temperatures, than the thermocouples, because of the temperature gradient between thermocouple and coating temperature. The string of samples 13, 14 and 15 could not be measured successfully, which was caused by a great degradation due to oxidation. Furthermore the inlet samples (1, 4, 7, 10, 13) show an abberant behavior, which is caused by variations in the cooling flow. Since the cooling flow is regulated for the center sample, especially the inlet samples can be effected by non stationary conditions. The general course from inlet to outlet however shows a similar behavior. With the SSE factor of $1.0875 > 1$, the SSE correction causes a reduction of measured temperature, i.e. signal (equation 3.13). The difference between the SSE corrections method 1 (based on the sample signal) and method 2 (based on the a weighted sample-ceramic signal) is here about 10 K, while the total SSE correction accounts for approximately 50, resp. 60 K. Due to the greater average

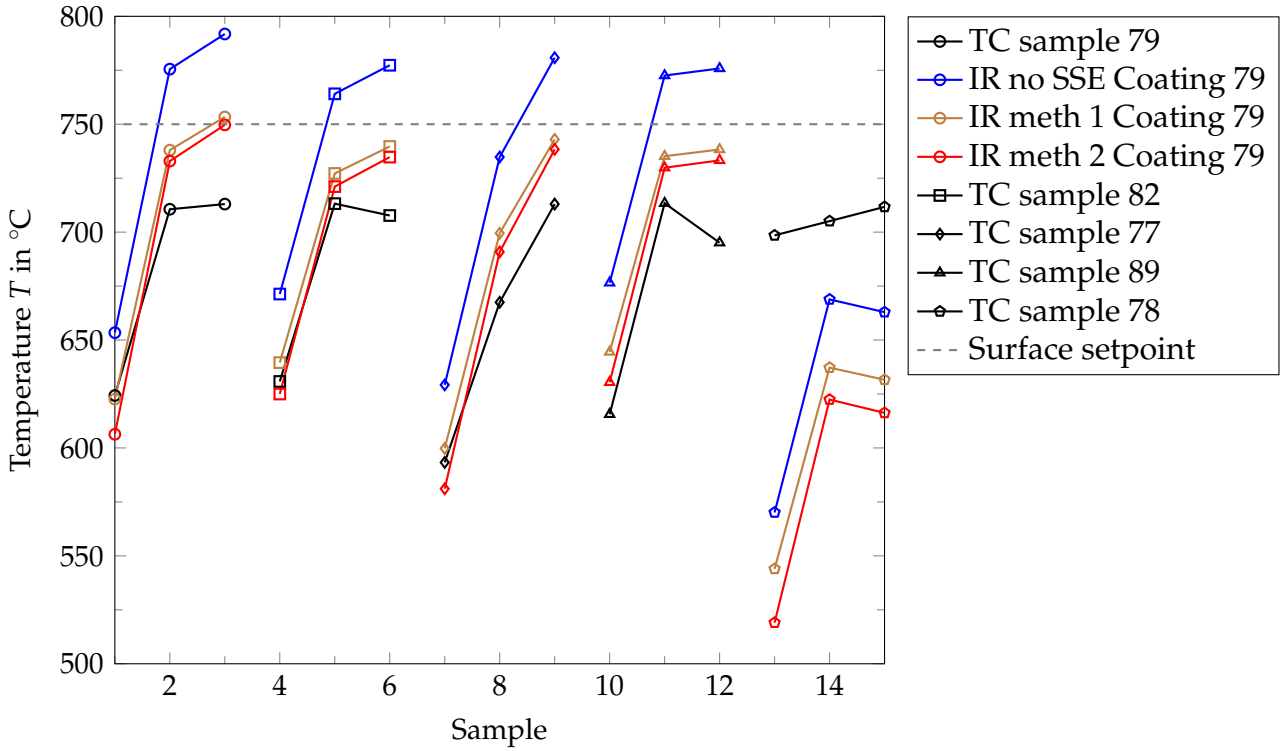

Figure 4.22.: Results of the dish campaign 1: Temperatures over the respective sample (substrate: Inconel 617) for the thermocouples (black), the IR measurement without SSE correction (blue), with method 1 (brown) and with method 2 (red). Sample enumeration follows figure 3.2. Samples 1-3, 4-6, 7-9, 10-12 and 13-15 each represent one string of samples, respective to the center samples 79, 82, 77, 89 and 78.

temperature of the ceramic, compared to the samples, the weighted signal in method 2 is increased, which causes a greater subtraction by the SSE correction. Generally method 1 is assumed to give an overestimation, while method 2 is assumed to give an underestimation. The real IR measured temperatures are therefore obtained in between and show reasonable results compared to the temperatures measured by the thermocouples.

Dish campaign 2

The evaluation of the dish campaign 2 is carried out analogous to the dish campaign 1. The analyzed samples, mounted on the solar test bench are shown in figure 4.23.

Figure 4.23.: Samples F2, 37, D532, RAI1169 and I+F2 of the dish campaign 2 mounted at the dish test bench.

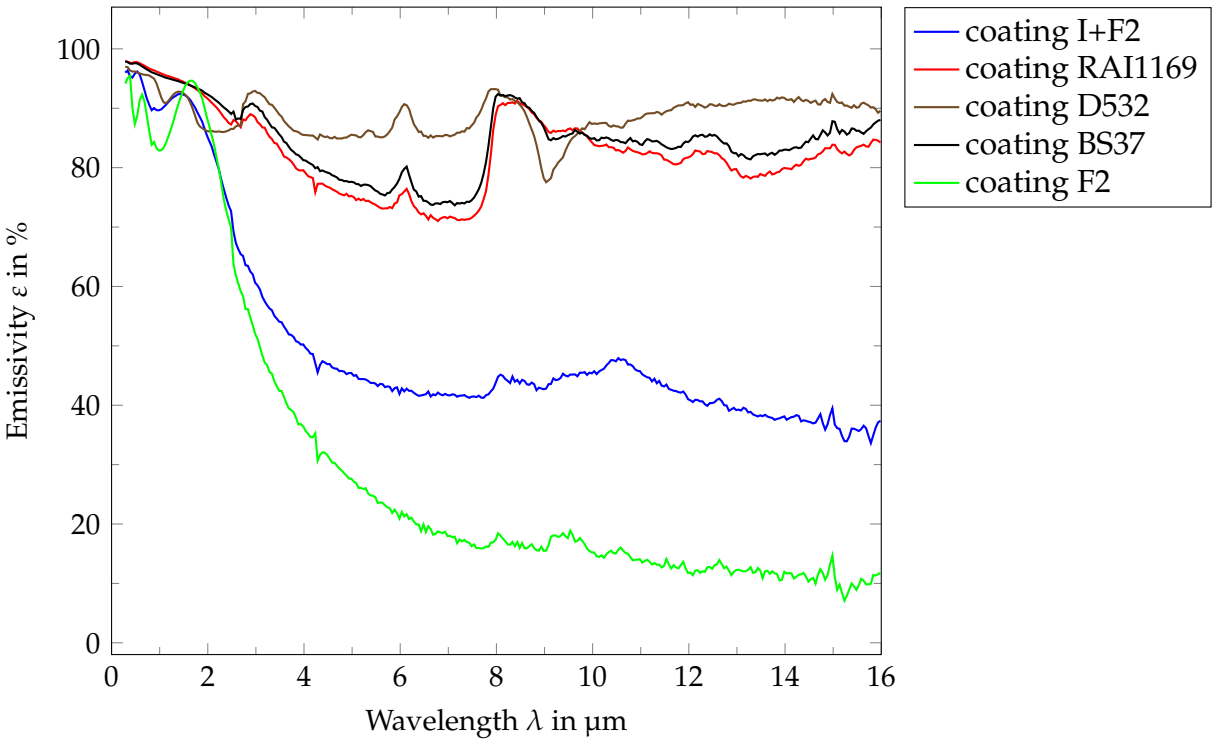

Figure 4.24.: Emissivity of center coatings I+F, RAI1169, D532, BS37 and F as a function of wavelength.

From the spectroscopy curves in figure 4.24 it is apparent that the coatings of the outside positioned sample strings, I+F2 and F2 show a selective behavior, with a great emissivity in the short wavelength band from 0 to 2 µm and a small emissivity in the long wavelength band from 8 to 16 µm. In between, the characteristic sigmoidal curve [47] is observed from 2 to 8 µm. The coatings RAI1169, D532 and BS37 can be characterized as grey bodies with emissivities in a range of $\varepsilon = 85\,\% \pm 10\,\%$. With a peak from 7.8 to 9 µm, their emissivity is increasing in the wavelength band of the IR camera from $\lambda = 7.55\,\mu m$ to $\lambda = 8.35\,\mu m$, shown in figure 4.25. The selective coatings I+F2 and F2 on the contrary behave in this wavelength band like grey bodies. The averaged results over the spectral range of the IR camera are shown for all samples in table 4.4.

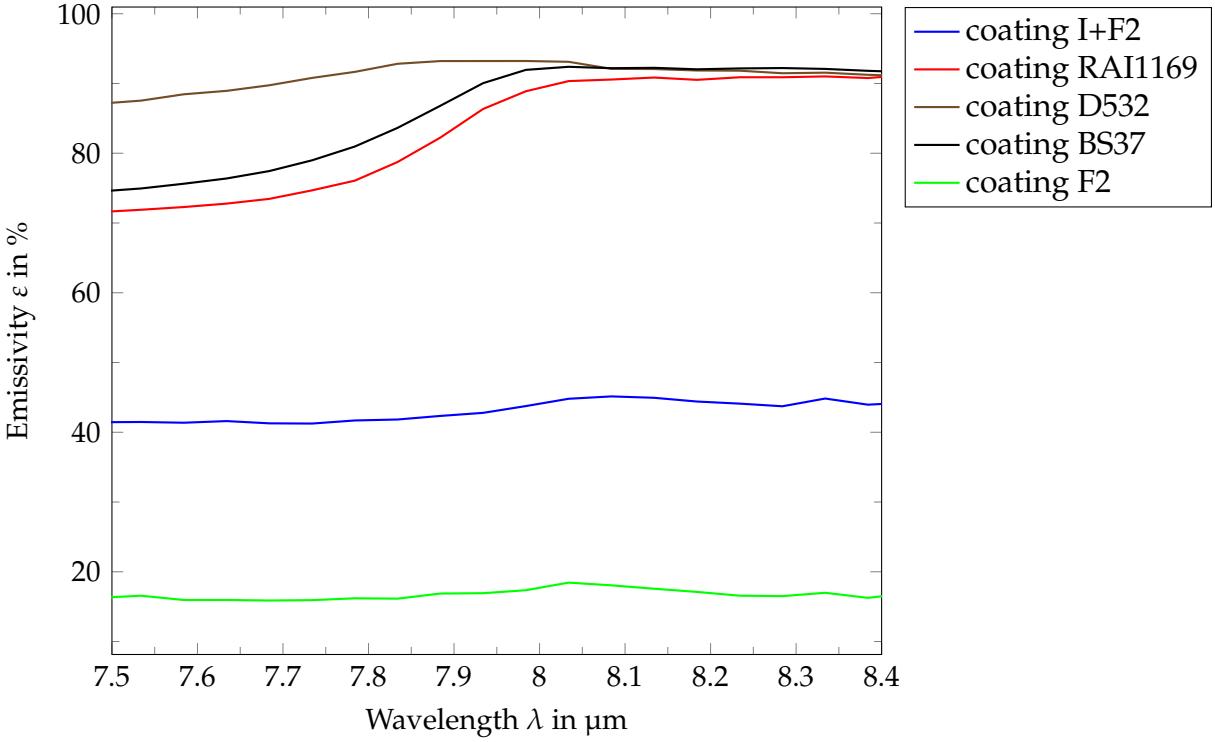

Figure 4.25.: Emissivity of center coatings I+F2, RAI1169, D532, BS37 and F2 over the wavelength range of the IR camera.

sample	1	2	3	4	5	6	7	8
Emissivity in %	22.27	18.19	16.39	88.01	86.31	86.92	91.89	91.20
sample	**9**	**10**	**11**	**12**	**13**	**14**	**15**	
Emissivity in %	89.61	82.39	83.08	81.82	41.24	43.07	44.36	

Table 4.4.: Photospectroscopic emissivity measurements of the dish campaign 2 samples from position 1 to 15, regarding figure 3.2.

While the deviations in emissivity between samples of one string, i.e. inlet, center and outlet, were found to be small for the grey body coatings (4...12) with $< 2\,\%$, the selective coatings reach higher deviations of $\approx 3\,\%$ (13,15) and $\approx 6\,\%$ (1,3). Generally a great degradation was observed for the selective coatings, as shown in figure 4.26. The deviations in emissivity might here result from spatial irregular degradations. Due to the lower resolution these deviations in

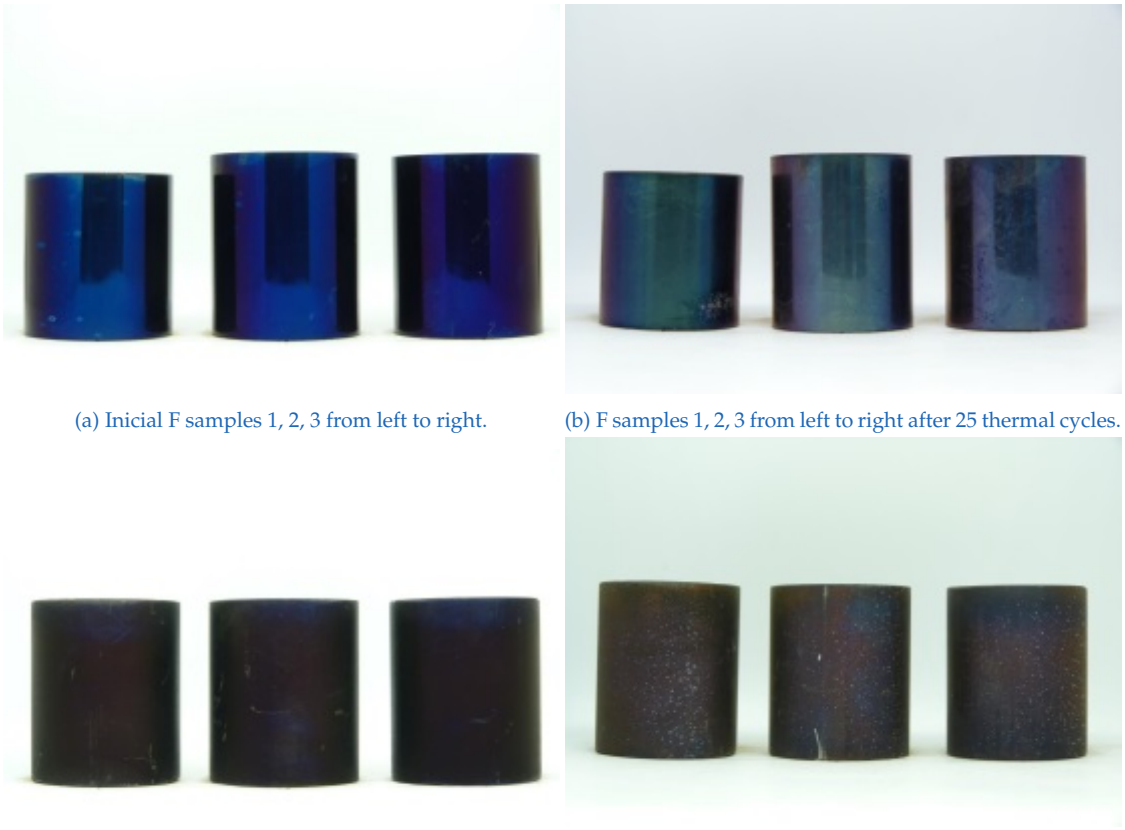

(a) Inicial F samples 1, 2, 3 from left to right.

(b) F samples 1, 2, 3 from left to right after 25 thermal cycles.

(c) Inicial F+I samples 13, 14, 15 from left to right.

(d) F+I samples 13, 14, 15 from left to right after 25 thermal cycles.

Figure 4.26.: Photographs of the selective samples at inicial state and after 25 thermal cycles.

degradations are not observed for the selective coatings in the thermal image (figure 4.27). However due to the small emissivity of the selective coatings in the wavelength band of the IR camera, they reflect most of their surrounding radiation. While the center of the samples reflect the ambient radiation, the curved edges mostly reflect the neighbor samples radiation. While this effect is well observed in figure 4.27 for the samples 1, 2, 3 on the left of the dish test bench, the samples 13, 14, 15 show a blurring of the radiations. Therefore the segmentation of these samples is made more difficult. Compared to figure

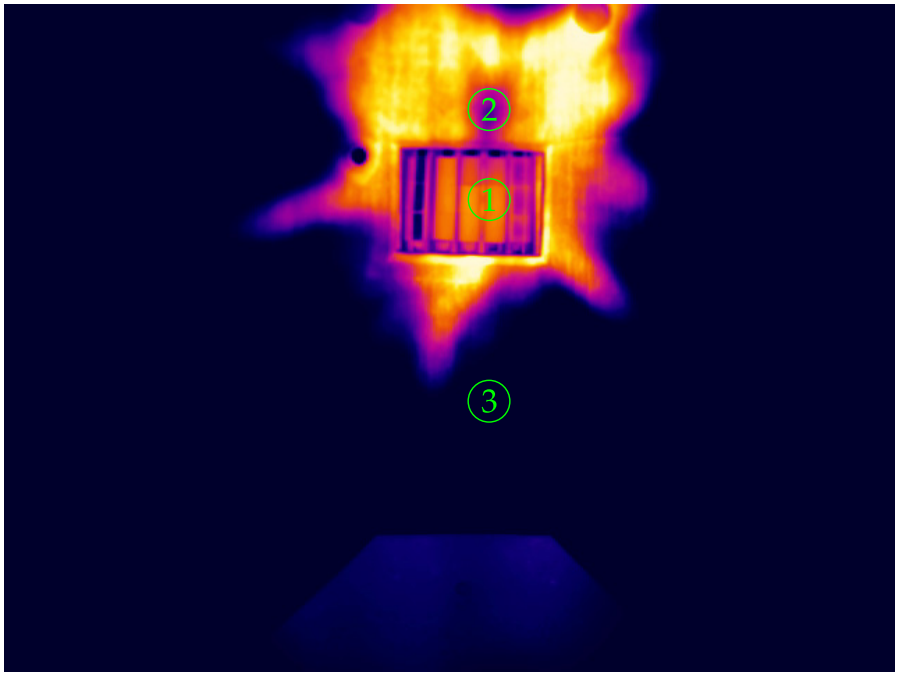

Figure 4.27.: Thermographic raw image at dish campaign 1. Tubular coated absorber samples (1) in the center, surrounded by heated ceramic (2). Remaining non heated ceramic and other environment (3) is not visible.

4.21, the illuminated area in figure 4.27 is segmented with 29714 ceramic pixel and 9017 sample pixel of similar size. Hereof a furthermore similar equivalent radiation source diameter of $X = 0.2185\,\mathrm{m}$ was calculated. Contrary to figure 4.21, with a mean ceramic temperature of 861 °C the mean ceramic temperature in figure 4.27 was only estimated to be 644 °C. The results of postprocessing the thermographic image are further shown in figure 4.28. Similarly to the dish campaign 1, a SSE correction of approximately 50 °C is observed. Since the mean ceramic temperature of 644 °C is very close to the temperature of the samples, the deviation between SSE method 1 and 2 becomes also very small. IR measurements of the grey body coatings (4-12) were found to be in the range of the thermocouples. Due to similar temperature differences between IR measurements and thermocouples, the center string with the samples 7, 8, 9, was assumed to be measured most accurately. The results of the strings with the samples 4, 5, 6 and 10, 11, 12 measure lower temperatures, which however still might be in the range of uncertainty. The selective coatings show irregularities in their temperature course and deviations of up to 100 °C. The temperatures of the samples 1 to 3 are underestimated by the IR measurements and the samples 13 to 15 are overestimated. The, due to the reflections of neighboring samples, reduced measuring area for the IR camera as well as the uncertainties in emissivity

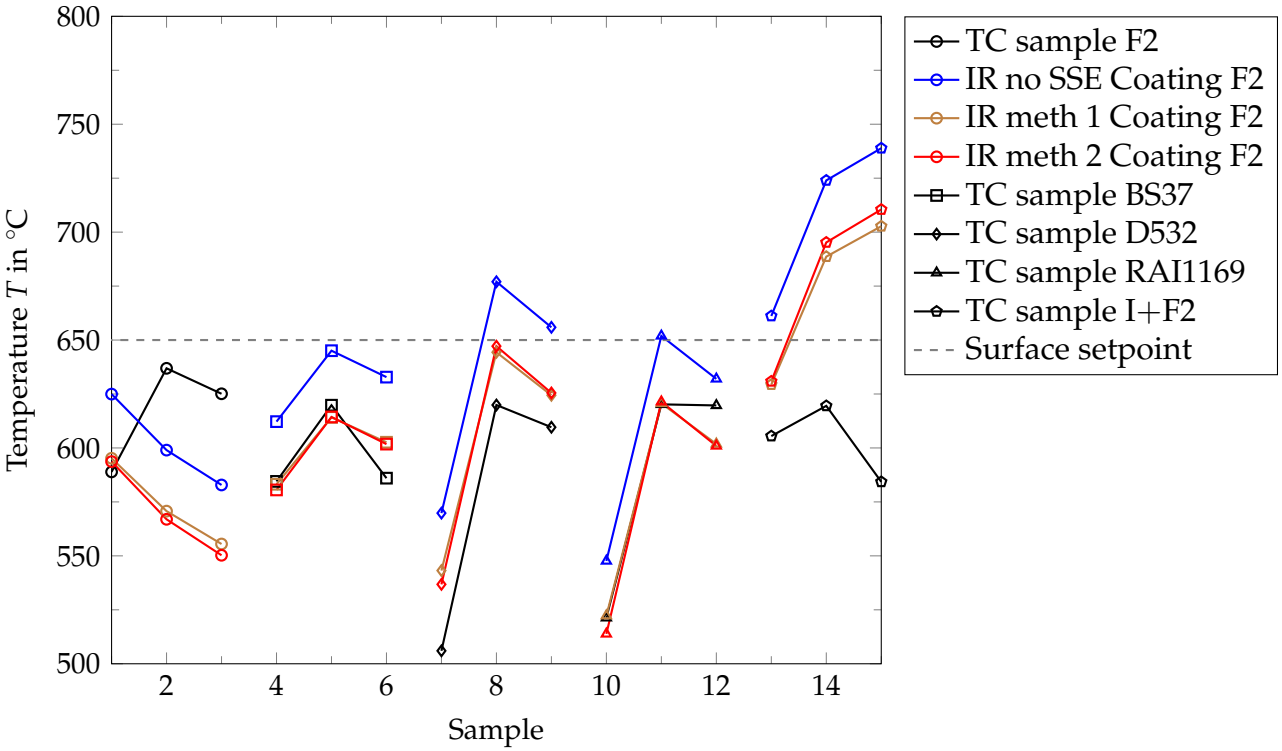

Figure 4.28.: Results of the dish campaign 2: Temperatures over the respective samples (Metal substrate: T91) for the thermocouples (black), the IR measurement without SSE correction (blue), with method 1 (brown) and with method 2 (red). Sample enumeration follows figure 3.2. Samples 1-3, 4-6, 7-9, 10-12 and 13-15 account for results of the strings of samples F2, BS37, D532, RAI1169 and I+F2.

measurement were assumed to be problematic for the utilized postprocessing. Slight shifts of the 3x3 pixel measuring area were tested and found to obtain great variances in the results, especially for the samples 13, 14 and 15.

5. Conclusion

Within the present work, infrared thermography is applied to measure high temperature receivers for CSP systems. Raw thermographic images were recorded with an IR camera (Optris PI640 G7) and its proprietary software. A postprocessing script, accounting for a major part of this work, was then used to process the images.
The basic parts of the postprocessing script are the sample segmentation, the radiometric model and the SSE correction. The sample segmentation finds evenly distributed samples and defines measuring areas for the respective thermocouples. These segmented areas are then processed by the radiometric model, which includes the radiometric chain and the radiation conversion in the IR camera. The radiometric chain concerns the outer-camera-influences on the object radiation, which are its emissivity, the ambiance, the protective window and the IR camera's enclosure. The influences were successfully determined from experiments, while the emissivity was obtained regarding the particular receiver coating with an infrared spectrophotometer. In this context the influences of the sun and atmosphere between IR camera and object were found to be neglectable. In the IR camera, the radiations are converted with the Sakuma-Hattori II equation, which was fitted prior to the IR camera's calibration curve. After applying the radiometric model on the raw images, theoretically exact temperatures are calculated.
Practically it was however found, that optical effects at the focusing lens, summarized as SSE cause a further impact. Since this SSE is not mentioned in the data, calibration or manual sheets by the IR manufacturing companies, it is very difficult to detect. With an recalibration of the IR camera, an analytical expression was fitted to represent the SSE. With further information from the segmentation tool, the SSE expression could be applied and the real object temperature could be estimated.
Beside with two validation experiments, the postprocessing script was also tested with two raw images from the solar dish facility. The first image consisted of one sandblasted and four gray body receiver coatings. Due to oxidation of the sandblasted sample between the spectrophotometry measurements, its emissivity and thus temperature could not be estimated. A sound temperature

difference to the thermocouples was measured for the gray bodies under stationary conditions at the center and outlet sample. SSE was here found to account for approximately 9 %. The second image included three gray body and two selective coatings. Here the selective coatings showed a greater degradation and variety in measured emissivities of up to 6 %. Moreover their segmentation was harder, due to their low emissivities in the IR camera bandwidth and reflections from neighboring samples. The difficulties with the selective samples were represented in great measurement variations. While too small temperature were measured for the samples F1, F2 and F3, the samples I+F1, I+F2 and I+F3 show too great temperatures compared to the thermocouples. The measurements of the samples neighboring to the selective coatings show slightly too small temperatures. Whether they are influenced by the selective coatings is not clear. A sound measurement, in agreement with the measurements of the first image, was obtained for the center samples D532 and D533.

Due to the implementation of the SSE, the postprocessing script is an improvement compared to the proprietary IR camera software. Besides the thermocouples, the IR camera provides an alternative way of measuring the receiver surface temperature. Here the postprocessing script may help to estimate a better temperature gradient calculation between thermocouple and surface, or estimate temperatures if thermal conductivities are uncertain. Compared to the thermocouple, the postprocessing script can measure the real spatial resolved surface temperature. This can be used to monitor temperature courses across the coatings.

Promising short term improvement should be the better estimation of the irradiated ceramic temperature and the spectrophotoscopic transmissivity measurement of the protective window. To validate the implemented SSE at the solar dish various experiments might be tested. First, the ceramic temperature might be measured from an solar test bench without receiver samples. Second, a sample equipped test bench ($\varepsilon_{\text{samples}} \approx \varepsilon_{\text{ceramic}}$) could be measured without blower cooling. SSE methods 1 and 2 should then measure similar temperatures. Finally the same setup with blower cooling should result in different temperatures for the SSE methods 1 and 2.
A long term improvement could be the online measurement and the implementation of a slit response function [48]. The slit response function could decrease blurring and improve the segmentation for selective coatings. Moreover another SSE method with annulus of varying temperatures presented in Saunders [49] could be implemented. Finally, an error calculation could be carried out with a statistically sound basis of images.

Bibliography

[1] M. Pfänder, "Pyrometrische temperaturmessung and an solarthermischen hochtemperatur-receivern," PhD thesis, Deutsches Zentrum and für Luft- und Raumfahrt, Institut für Technische Thermodynamik, 2006 (cit. on pp. 1, 16, 31–33).

[2] REN21, "Renewables 2018 global status report," annual overview, 2018 (cit. on p. 1).

[3] LAZARDS. (2018). Lazard's levelized cost of energy analysis - version 12.0, [Online]. Available: https://www.lazard.com/media/450784/lazards-levelized-cost-of-energy-version-120-vfinal.pdf (cit. on pp. 1, 2).

[4] SOLARGIS. (Apr. 25, 2019). Solar resource map direct normal irradiation, [Online]. Available: https://solargis.com/maps-and-gis-data/download/world (cit. on p. 2).

[5] IRENA, "Renewable energy technology: Cost analysis series," International Renewable Energy Agency, Tech. Rep., 2012 (cit. on pp. 1, 2).

[6] C. K. Ho, "Advances in central receivers for cencentrating solar applications," *Solar Energy*, 2017 (cit. on p. 2).

[7] C. K. Ho and J. E. Pacheco, "Levelized cost of coating (lcoc) for selective absorber materials," *Solar Energy*, vol. 108, pp. 315–321, Oct. 2014 (cit. on p. 2).

[8] RAISELIFE. (). Raising the lifetime of functional materials for concentrated solar power technology, [Online]. Available: http://raiselife.eu/ (cit. on p. 2).

[9] S. Caron, F. Sutter, N. Algner, M. Esteller, Y. Binyamin, M. Baidossi, A. Kenigsberg, A. Agüero, D. Fähsing, and C. Hildebrandt, "Accelerated ageing of solar receiver coatings: Experimental results for t91 and vm12 steel substrates," *AIP Conference Proceedings 2033, 230002 (2018)*, 2018 (cit. on pp. 2, 25, 27).

[10] M. Vollmer and K.-P. Möllmann, *Infrared Thermal Imaging*. 2018 (cit. on pp. 3, 4, 6, 7, 13–15, 17–19, 22, 23, 38).

[11] J. A. Duffie and W. A. Beckman, *Solar Engineering of Thermal Processes*. 2013 (cit. on pp. 3, 5, 6).

[12] Minkina and Dudzik, *Infrared thermography errors and uncertainties*, reality, 2009 (cit. on p. 3).

[13] J. C. Maxwell, "On physical lines of force," *The London, Edinburgh, and Dublin Philosophical Magazine and Journal of Science*, vol. 21, no. 141, pp. 338–348, May 1861 (cit. on p. 3).

[14] kalckar, "General introduction to volumes 6 and 7," *Elsevier*, 1985 (cit. on p. 3).

[15] G. Kirchhoff, "Ueber das verhältniss zwischen dem emissionsvermögen und dem absorptionsvermögen der körper für wärme und licht," *Annalen der Physik*, 1860 (cit. on p. 9).

[16] M. K. E. L. Planck, "Zur theorie des gesetzes der energieverteilung im normalspectrum," *Verhandl. Dtsc. Phys. Ges.*, 1900 (cit. on p. 10).

[17] W. Minkina and D. Klecha, "Atmospheric transmission coefficient modelling in the infrared for thermovision measurements," *Journal of Sensors and Sensor Systems*, vol. 5, no. 1, pp. 17–23, Jan. 2016 (cit. on pp. 15, 19).

[18] A. Berk, L. Bernstein, and D. Robertson, "Modtran: A moderate resolution model for lowtran," spectral sciences inc Burlington ma, Tech. Rep., 1987 (cit. on pp. 15, 36).

[19] X. P. Maldague, *Theory and Practice of Infrared Technology for Nondestructive Testing*. 2001 (cit. on p. 15).

[20] VDI/VDE, Temperature measurement in industry radiation thermometry, in *VDI/VDE-RICHTLINIEN*. 1995 (cit. on pp. 16, 19, 42).

[21] A. Rogalski, "Infrared detectors: Status and trends," *Progress in Quantum Electronics 27*, 2003 (cit. on p. 18).

[22] P. Saunders, "General interpolation equations for the calibration of radiation thermometers," *Metrologia*, vol. 34, no. 201, 1997 (cit. on p. 19).

[23] H. J. Kostkowski and R. D. Lee, *Theory and methods of optical pyrometry*. 1962 (cit. on p. 19).

[24] K. M. Sakuma F, "Interpolation equations of scales of radiation thermometers," *Proceedings of TEMPMEKO 1996, pp. 305–310*, 1996 (cit. on pp. 19, 42, 43).

[25] P. Saunders and R. White, "Physical basis of interpolation equations for radiation thermometry," *Metrologia*, 2003 (cit. on p. 19).

[26] J. W. Hahn and C. Rhee, "Interpolation equation for the calibration of infrared pyrometers," *Metrologia*, 1994 (cit. on p. 19).

[27] J.Fischer and H. J. Jung, "Determination of the thermodynamic temperatures of the freezing points of silver and gold by near-infrared pyrometry," *Metrologia*, 1989 (cit. on p. 19).

[28] F. Sakuma, H. Sakate, B. C. Johnson, C. Gibson, G. Machin, T. Ricolfi, M. Battuello, J. Fischer, and H.-J. Jung, "International comparison of radiation temperature scales among five national metrological laboratories using a transfer standard radiation thermometer," *Metrologia*, vol. 33, no. 241, 1996 (cit. on p. 19).

[29] J. Fischer, P. Saunders, M. Sadli, M. Battuello, C. W. Park, Y. Zundong, H. Yoon, W. Li, E. van der Ham, F. Sakuma, Y. Yamada, M. Ballico, G. Machin, N. Fox, J. Hollandt, M. Matveyev, P. Bloembergen, and S. Ugur, "Uncertainty budgets for calibration of radiation thermometers below the silver point," CCT-WG5 on Radiation and Thermometry, Tech. Rep., 2008 (cit. on p. 19).

[30] P. Saunders and D. R. White, "A focus effect in some thermal imaging systems," Measurement Standards Laboratory of New Zealand, Tech. Rep., 2013 (cit. on p. 20).

[31] G. Machin and M. Ibrahim, "Size of source effect and temperature uncertainty i - high temperature systems," *radiation thermometry*, 1999 (cit. on p. 20).

[32] P. Saunders and H. Edgar, "On the characterization and correction of the size-of-source effect in radiation thermometers," *Metrologia*, 2009 (cit. on pp. 20, 21).

[33] P. Saunders, "Msl technical guide 29: Focus effect in thermal imagers," Measurement Standards Laboratory of New Zealand, Tech. Rep., 2017 (cit. on pp. 20, 21, 44).

[34] P. Saunders, "Dealing with the size-of-source effect in the calibration of direct-reading radiation thermometer," Measurement Standards Laboratory of New Zealand, Tech. Rep., 2013 (cit. on p. 22).

[35] T. P. Jones and J. Tapping, "A precision photoelectric pyrometer for the realization of the ipts-68 above 1064.43 c," *18*, 1982 (cit. on p. 21).

[36] T. Ricolfi and L. Wang, "Experiments and remarks on the size-of-source effect in precision radiation thermometry," *Vol. 93.*, 1993 (cit. on p. 21).

[37] M. Ohtsuka and R. E. Bedford, "Measurement of size-of-source effects in an optical pyrometer," *Volume 7, Issue 1*, 1989 (cit. on p. 21).

[38] H. W. Yoon, D. W. Allen, and R. D. Saunders, "Methods to reduce the size-of-source effect in radiometers," *Metrologia*, 2005 (cit. on p. 22).

[39] S. Ulmer, "Messung der strahldichteverteilung von punktkonzentrierenden solarthermischen kraftwerken," PhD thesis, Institut für Thermodynamik und Wärmetechnik der Universität Stuttgart, 2003 (cit. on p. 26).

[40] M. Israel, "Entwicklung eines uav-basierten systems zur rehkitzsuche und methoden zur detektion und georeferenzierung von rehkitzen in thermalbildern," PhD thesis, Universität Osnabrück, 2016 (cit. on p. 30).

[41] ASTM. (Apr. 21, 2019). Standard tables for reference solar spectral irradiances: Direct normal and hemispherical on 37 degree tilted surface: Astm g173-03, [Online]. Available: https://www.astm.org/Standards/G173 (cit. on p. 31).

[42] A. M. Efimov, V. G. Pogareva, and A. V. Shashkin, "Water-related bands in the absorption spectra of silicate glasses," *Journal of Non-Crystalline Solids*, vol. 332, no. 1-3, pp. 93–114, Dec. 2003 (cit. on p. 31).

[43] I. O. for Standardization, Ed., *ISO 22975-3 Solar energy - Collector components and materials Part 3: Absorber surface durability*, 2014 (cit. on p. 34).

[44] P. Saunders, "Size-of-source effect in infrared thermometers," Measurement Standards Laboratory of New Zealand, Tech. Rep. be, 2017 (cit. on pp. 44, 45).

[45] P. Bloembergen, "Analytical representations of the size-of-source effect," *Metrologia*, vol. 46, no. 534, 2009 (cit. on pp. 45, 55, 56).

[46] MIKRON. (Apr. 25, 2019). Table of emissivity of various surfaces, [Online]. Available: http://www-eng.lbl.gov/~dw/projects/DW4229_LHC_detector_analysis/calculations/emissivity2.pdf (cit. on p. 70).

[47] M. Wirz, J. Petit, A. Haselbacher, and A. Steinfeld, "Potential improvements in the optical and thermal efficiencies of parabolic trough concentrators," *Solar Energy*, vol. 107, pp. 398–414, Sep. 2014 (cit. on p. 74).

[48] O. Riou, J. F. Durastanti, and V. Tortel, "Evaluation of error in temperature starting from the slit response function and calibration curve of a thermal focal plane array camera," in *Proceedings of the 2006 International Conference on Quantitative InfraRed Thermography*, QIRT Council, 2006 (cit. on p. 79).

[49] P. Saunders, "Correcting radiation thermometry measurements for the size-of-source effect," *International Journal of Thermophysics*, vol. 32, no. 7-8, pp. 1633–1654, May 2011 (cit. on p. 79).

Appendix A.

Listing of Errors

- Temperature input $T_{\text{input}}(\varepsilon = 1, \tau = 1) \pm 2\,\%$ [Data sheet IR camera]

- Emissivity $\varepsilon \pm 0.5\,\%$ [Spectrophotometer]
- Transmissivity $\tau \pm 0.37\,\%$ [Blackbody experiments]

- Size of Source Effect $SSE \pm 0.25\,\%$ [Least square fit]
  - Method 1 ($D \pm 0.1\,\text{m}$, $X \pm 0.05\,\text{m}$, $T_{\text{sample}} \pm 2\,\%$)
  - Method 2 ($D \pm 0.1\,\text{m}$, $X \pm 0.05\,\text{m}$, $T_{\text{sample}} \pm 2\,\%$, $T_{\text{ceramic}} \pm 2\,\%$, ψ)
- Sakuma-Hattori fit $S \pm 1.6\,\%$ [Least square fit]

- Thermocouple $T_{\text{TC}} \pm 1.0\,\%$ [K-type]

Rough estimations:
At $\approx 700\,^{\circ}\text{C}$
$1\,\%$ $(\varepsilon, \tau) \approx 4\,\text{K}$
5 Signalvalues $\approx 1\,\text{K}$

Appendix B.

Data sheets

B.1. IR camera Optris PI 640 G7

optris® PI 640 G7
TECHNICAL DATA

optris infrared sensing

High-resolution thermal imaging solution for the glass industry

Features:

- Line scan function through license-free analysis software optris® PIX Connect
- Compact in size: 46 x 56 x 76 - 100 mm (1.8 x 2.2 x 3.0 - 3.9 in)
- Frame rate of up to 125 Hz
- Max. scan angle of 111° with 800 pixels per line

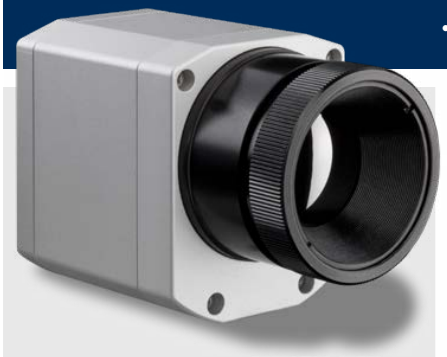

Infrared camera with line scan mode

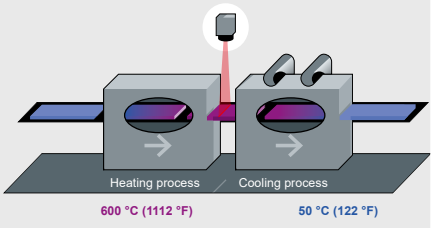

For further information on non-contact temperature measurement in the glass industry, please visit **www.optris.com/temperature-measurement-glass-industry**

Technical specifications	
Optical resolution	640 x 480 pixel
Detector	FPA, uncooled (17 µm x 17 µm)
Spectral range	7.9 µm
Temperature range	200 ... 1500 °C (392 ... 2732 °F)
Sighting range	0 ... 250 °C (32 ... 482 °F)
Frame rate	32 Hz / 125 Hz @ 640 x 120 pixels
Optics (FOV)	15° x 11° FOV / f=41.5 mm (f=1.6 in) or 33° x 25° FOV / f = 18.7 mm (f=0.7 in) or 60° x 45° FOV / f = 10.5 mm (f=0.4 in) or 90° x 66° FOV / f = 7.7 mm (f=0.3 in) max. FOV: 111° / 800 pixels (diagonal scan line / 90° lens)
Thermal sensitivity (NETD) at T_{Obj} = 650 °C (1202 °F)	130 mK
Accuracy	±2 °C or ±2 % (±3.6 °F or ±2 %), whichever is greater
PC interface	USB 2.0 / optional USB to GigE (PoE) interface
Process interface (PIF), standard	0 – 10 V input, digital input (max. 24 V), 0 – 10 V output
Process interface (PIF), industrial	2x 0 – 10 V input, digital input (max. 24 V), 3x 0 – 10 V output, 3x relay (0 – 30 V/ 400 mA), fail-safe relay
Cable length (USB)	1 (standard) / 5 m / 10 m / 20 m (3.3 / 16.4 / 32.8 / 65.6 ft) 5 and 10 m (16.4 and 32.8 ft) also as HT cable (180 or 250 °C [356 or 482 °F])
Ambient temperature	0 °C ... 50 °C (32 °F ... 122 °F)
Storage temperature	– 40 ... 70 °C (– 40 ... 158 °F)
Relative humidity	20 – 80 %, non-condensing
Enclosure (size / rating)	46 x 56 x 76 - 100 mm (1.8 x 2.2 x 3.0 - 3.9 in) (depending on lens + focus position) / IP 67 (NEMA 4)
Weight	320 g (11.3 oz), incl. lens
Shock / Vibration [1)]	IEC 60068-2
Tripod mount	¼ - 20 UNC
Power supply	USB powered
Scope of supply	• USB camera with 1 lens • USB cable (1 m [3.3 ft]) • Table tripod • Standard PIF with cable (1 m [3.3 ft]) and terminal block • Software package optris® PIX Connect • Rugged outdoor case

[1)] For more details see operator's manual

Optris Infrared Sensing, LLC · 200 International Drive, Suite 170 · Portsmouth · NH 03801 USA
Phone: 603-766-6060 · E-Mail: sales@optris-ir.com · www.optris.com

optris® PI 640 G7

Dimensions

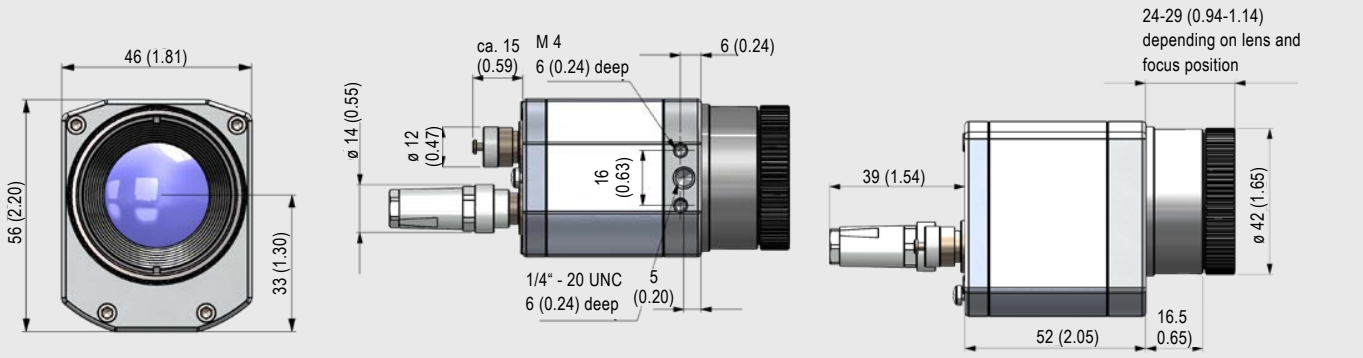

Dimensions in mm (in)

Process integration

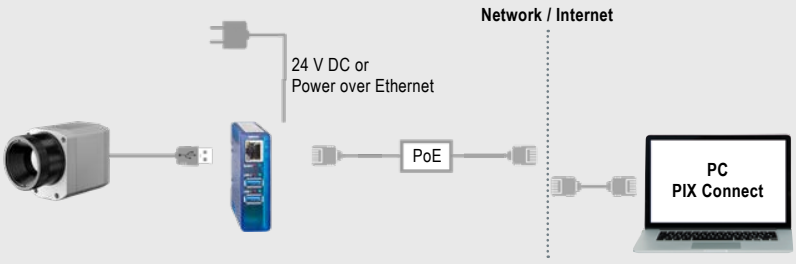

optris® USB-Server Gigabit 2.0

- Network connection via Gigabit Ethernet
- Full TCP/IP support incl. routing and DNS
- Two independent USB ports
- Power via PoE or external voltage supply at 24 – 48 V DC
- Galvanic isolation 500 V_{RMS}
- Remotely configurable via web based management

For further information please visit
www.optris.com/usb-server-industry-isochron

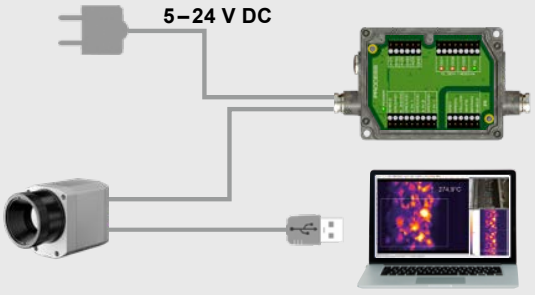

optris® Industrial process interface

- Use of camera for process monitoring in industrial environments
- Continous fail safe monitoring of imager, software and cable connections
- 3 analog/ alarm outputs,
  2 analog inputs,
  1 digital input,
  3 alarm relais
  1 fail-safe relay

For further information please visit
www.optris.com/industrial-process-interface

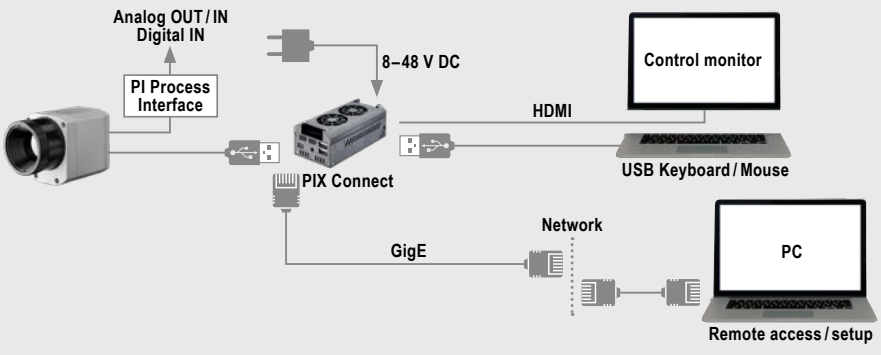

optris® PI NetBox

- Miniature PC as add-on to the PI series for stand-alone system
- Integrated hardware and software watchdog
- Connections: 2x USB 2.0, 1x USB 3.0, 1x Mini-USB 2.0, Micro-HDMI, Ethernet (Gigabit Ethernet), micro SDHC / SDXC card

For further information please visit
www.optris.com/pi-netbox

B.2. Calibration Blackbody MIKRON M305

LUMASENSE TECHNOLOGIES
An Advanced Energy Company

MIKRON Calibration Sources

Compact, general purpose blackbody calibration source for medium temperatures. Temperature range: 100 ... 1000 °C (212 ... 1832 °F).

M305

- Highly mobile due to small form factor and weight (only 25 kg or 55 lbs)
- High accuracy ± 0.2% of reading ±1 °C
- High emissivity 1.0 effective @ 0.7 ... 1.8 µm T > = 230 °C, 1.0 @ 8 ... 14 µm T < 230 °C
- Manufactured and tested to meet rigid quality control standards
- Furnished with certificate of calibration traceable to NIST
- RS232 (standard) or RS485 (option) serial communication output

Blackbody calibration sources are infrared radiators used for calibrating and verifying the output signals of infrared thermometers (pyrometers), thermal imaging systems, heat flux measurement systems, or spectrographic analysis systems. LumaSense supplies a unique selection of very precise calibration sources that are traceable to national standards.

The M305 blackbody calibration source uniquely combines portability with wide temperature range, high emissivity and high accuracy. It is an ideal calibration unit where portability is required or where installation space is limited. Its spherical, metal cavity design yields an emissivity of 0.995 over the temperature range of 100 to 1000 °C (212° to 1832 °F) with an aperture of 25 mm (1”). An integrally mounted PID controller adds to the unique versatility of this calibrator.

Quotations for custom designs and variations are available upon request.

LumaSense calibration sources have long been the gold standard to calibrate the instruments that keep your operations up and running. These blackbodies are superior because of the emissivity values, homogeneous emission areas, and a wide range of different sized apertures to adapt to the desired target area. In addition, fast heat-up times and high temperature stability are guaranteed. The quality of our calibration sources is guaranteed by tests, burn-in times, and radiometric calibrations. On most models, a certificate is provided to document the traceability to the international temperature scale ITS90 and NIST.

Typical Applications

- Sapphire Probe Optical Pyrometer Calibrations
- Infrared Temperature Sensors
- Infrared Thermal Imaging Systems
- Spectrographic Analyzers
- Radiometers
- Flux Meters

Technical Data

Measurement Specifications

Temperature Range:	100 ... 1000 °C (210 ... 1832 °F)
Temperature Uncertainty[1]:	± 0.2% of reading ± 1 °C
Temperature Resolution:	0.1 °C
Stability[2]:	1 °C per 8 hour period
Source Non-Uniformity:	± 0.2 °C typical @ T < 230 °C, ± 1 °C typical at T > 230 °C
Heated Cavity Shape:	Spherical
Exit Port Diameter:	25.4 mm (1.0")
Emissivity:	0.995 ± 0.0005 (calculated from cavity shape) Effective Emissivity: 1.00 @ 8 ... 14 µm T < 230 °C, 1.00 @ 0.7 ... 1.8 µm T > 230 °C
Standard Calibration Method:	Radiometric
Temperature Sensor:	Thermocouple
Warm-up Time:	60 minutes from ambient to 700 °C
Slew Rate to 1 °C Stability:	~ 11 °C / min for Amb < T < 200 °C ~ 20 °C / min for Amb < T < 800 °C ~ 10 °C / min for T > 900 °C
Slew Rate to 0.1 °C Stability:	1 hour between setpoints

[1] Accuracy calibration performed radiometrically, the uncertainty of emissivity and transfer standard are already included.
[2] Provided stable AC mains voltage and minimum air flow across the exit port or emitter plate.

Communications/Interface

Remote Set Point:	Via serial port
Method of Control:	Digital self tuning PID controller

Environmental Specifications

Operating Ambient Temp:	0 ... 44 °C (32 ... 110 °F)
Cooling:	Fan cooled, air inlet on rear panel
Operating Humidity:	90% RH max, non-condensing
Dimensions (H x W x D):	270 mm x 430 mm x 370 mm (10.6" x 16.9" x 14.6")
Weight:	25 kg (55 lbs.)
CE Certified:	Yes

Electrical

Power Requirements:	115 V AC @ 50 & 60 Hz or 230 V AC @ 50 & 60 Hz, 1000W

Reference Numbers

14430-1	M305, 100 ... 1000 °C, 25 mm, RS232, 115 V AC @ 50 & 60 Hz
14430-2	M305, 100 ... 1000 °C, 25 mm, RS232, 230 V AC @ 50 & 60 Hz

Accessories

14002-1	Cold aperture wheel assembly, 6 apertures 25.4 ... 2.54 mm, for M300, M305, M330, M335, M390
14002	Cold aperture wheel assembly, 6 apertures 50 ... 1.56 mm, for M300, M305, M330, M335, M390
19140-485	Optional: Serial Communication Output RS485 (built-in ex works) for M300, M305, M315X, M335, M345X, M360, M360A, M390
3840810	IGA 12-TSP, 1570 nm, 200" 1020 °C, through-lens-sighting, laser target., focus. Optics 2

LumaSense Technologies | An Advanced Energy Company — Temperature and Gas Sensing Solutions

Americas, Australia, Asia
Sales & Service
Santa Clara, CA
Ph: +1 800 631 0176
Fax: +1 408 727 1677

Europe, Middle East, Africa
Sales & Service
Frankfurt, Germany
Ph: +49 69 97373 0
Fax: +49 69 97373 167

India
Sales & Support Center
Mumbai, India
Ph: +91 22 67419203
Fax: +91 22 67419201

China
Sales & Support Center
Shanghai, China
Ph: +86 133 1182 7766
Ph: +86 21 5899 7915

info@lumasenseinc.com
www.lumasenseinc.com

B.3. Verification Blackbody MIKRON M330

LUMASENSE® TECHNOLOGIES
An Advanced Energy Company

MIKRON Calibration Sources

High Temperature Blackbody Calibration Source. Temperature Range: 300 ... 1700 °C (572 ... 3092 °F).

M330

- High effective emissivity 1.0 @ 0.65 ... 1.8 µm
- High accuracy
- Excellent stability +/-1 °C per 8 hour period
- Fast slew rate (limited to 20 °C / min)
- Wide temperature range
- Manufactured and tested to meet rigid quality control standards
- Furnished with certificate of calibration traceable to NIST
- RS232 (standard) or RS485 serial communication output

Blackbody calibration sources are infrared radiators used for calibrating and verifying the output signals of infrared thermometers (pyrometers), thermal imaging systems, heat flux measurement systems, or spectrographic analysis systems. LumaSense supplies a unique selection of very precise calibration sources that are traceable to national standards.

The M330 is a blackbody calibration source utilizing a digital indicating temperature controller that may be set to any temperature between 300 °C (572 °F) and 1700 °C (3092 °F). A precision thermocouple controls the blackbody cavity providing high accuracy and repeatability.

A closed-end tube with a 25 mm (1") aperture diameter is heated by specially manufactured elements. The temperature controller uses the industry standard PID algorithms to control the emitter temperature to within +/-0.5 °C.

The blackbody uses a resistive heater that provide long life. (Running at temperatures greater than 1600 °C for long periods will shorten heater life.) An independent over-temperature power cutout system is an added safety feature. An internal fan keeps the cabinet surfaces at a safe, comfortable temperature.

LumaSense calibration sources have long been the gold standard to calibrate the instruments that keep your operations up and running. These blackbodies are superior because of the emissivity values, homogeneous emission areas, and a wide range of different sized apertures to adapt to the desired target area. In addition, fast heat-up times and high temperature stability are guaranteed. The quality of our calibration sources is guaranteed by tests, burn-in times, and radiometric calibrations. On most models, a certificate is provided to document the traceability to the international temperature scale ITS90 and NIST

Typical Applications

- Infrared Temperature Sensors
- Infrared Thermal Imaging Systems
- Spectroradiometers
- High Energy Photon Generators
- Solar Radiance Simulation
- Optical Pyrometers

Technical Data

Measurement Specifications

Temperature Range:	300 ... 1700 °C (572 ... 3092 °F)
Temperature Uncertainty[1]:	± 0.25% of reading ± 1 °C
Temperature Resolution:	0.1 °C
Stability[2]:	± 1 °C per 8 hour period
Source Non-Uniformity:	± 1 °C within center 1/3 of ID
Heated Cavity Shape:	Closed end tube 41 mm ID X 255 mm long with ≈ 125 mm heated length (field replaceable)
Exit Port Diameter:	25 mm (1″)
Emissivity:	1.0 @ 0.65 ... 1.8 µm (lower at longer wavelengths - a correction table is supplied in the manual)
Standard Calibration Method:	Radiometric (pyrometric)
Temperature Sensor:	Type B thermocouple
Warm-up Time:	45 ... 50 min. from ambient to 300 °C 65 ... 80 min. from 300 ... 1600 °C
Slew Rate to 1 °C Stability:	~ 20 °C / minute
Slew Rate to 0.1 °C Stability[3]:	~ 30 min for T < 500 °C, ~ 20 min T > 500 °C

[1] Accuracy calibration performed radiometrically, the uncertainty of emissivity and transfer standard are already included.
[2] Provided stable AC mains voltage and minimum air flow across the exit port or emitter plate.
[3] For 100 °C setpoint change, typ.

Communications/Interface

Remote Set Point:	Via serial port
Method of Control:	Digital Self-Tuning PID Controller

Environmental Specifications

Operating Ambient Temp:	0 ... 44 °C (32 ... 110 °F)
Cooling:	Fan cooled, air inlet on rear panel
Operating Humidity:	90% RH max, non-condensing
Dimensions (H x W x D):	648 mm x 500 mm x 551 mm (25.52″ x 19.7″ x 21.7″)
Weight:	80 kg (175 lbs.)
CE Certified:	Yes

Electrical

Power Requirements:	208 ... 240 V AC, 50 & 60 Hz, 3000 VA Maximum (US) 230 V AC, 50 Hz (EU)

Reference Numbers

18670-1	M330-US, 300 ... 1700 °C, 25 mm, 208 ... 240 V AC, 50 & 60 Hz, (North America)
3801200	M330-EU, 300 ... 1700 °C, 25 mm, RS232, 230 V AC, 50 Hz (Manufactured in Germany)

Accessories

14002-1	Cold aperture wheel assembly, 6 apertures 25.4 ... 2.54 mm, for M300, M305, M330, M335, M390
14002	Cold aperture wheel assembly, 6 apertures 50 ... 1.56 mm, for M300, M305, M330, M335, M390
19140-485	Optional RS485 communications
3840820	IGA 12-TSP, 1570 nm, 250″ 1400 °C, through-lens-sighting, laser target., focus. Optics 2
3840700	IS 12-TSP, 940 nm, 530 ... 1900 °C, through-lens-sight., laser target., focus. Optics 2

LumaSense Technologies | An Advanced Energy Company — Temperature and Gas Sensing Solutions

Americas, Australia, Asia
Sales & Service
Santa Clara, CA
Ph: +1 800 631 0176
Fax: +1 408 727 1677

Europe, Middle East, Africa
Sales & Service
Frankfurt, Germany
Ph: +49 69 97373 0
Fax: +49 69 97373 167

India
Sales & Support Center
Mumbai, India
Ph: +91 22 67419203
Fax: +91 22 67419201

China
Sales & Support Center
Shanghai, China
Ph: +86 133 1182 7766
Ph: +86 21 5899 7915

info@lumasenseinc.com
www.lumasenseinc.com

B.4. Calibration Blackbody MIKRON M305

PIKE TECHNOLOGIES

Mid-IR IntegratIR – *Integrating Sphere*

Upward-looking IntegratIR

Features

- 3-inch sphere – gold-coated, Lambertian scatterer for high-performance measurements
- 12-degree hemispherical diffuse reflectance measurement with specular exclusion port
- Diffuse transmission station for measurement of highly scattering samples in transmission mode
- Choice of integrated, high-performance detector MCT or DTGS for ultimate configurability
- Upward- and downward-looking optical configurations to accommodate a wide range of sample sizes and types
- In-sample-compartment design to minimize laboratory space requirements
- Configurations available for most FTIR spectrometers

The integrating sphere is very often an accessory of choice when studying reflectance properties of solids, analyzing light-scattering and/or highly absorbing samples and collecting spectra difficult to obtain with standard sampling techniques. PIKE Technologies offers mid-IR integrating spheres, designed for research and standard applications that require sensitivity and the ability to collect high-quality data from difficult to analyze samples.

The PIKE IntegratIR™ spheres are available in upward- and downward-looking configurations and are suitable for the measurements of absolute and relative diffuse reflectance of solids, powders and opaque liquids. Each feature a 3-inch diameter highly reflective gold-coated sphere. The accessory mounts in the sample compartment of the FTIR spectrophotometer, and uses a dedicated detector for maximum performance.

Gold-coated Lambertian finish sphere

Both upward- and downward-looking mid-IR spheres feature a 12-degree illumination of the sample, and offers a specular exclusion port. For the upward-looking sphere, reflectance samples are placed directly onto the sample port located on the top of the sphere. This sphere is ideal for large and/or thick solid samples. For powder samples, a standard ZnSe window is available. If preferred, a KBr window can also be used with the sample plate to minimize the reflection loss compared to ZnSe.

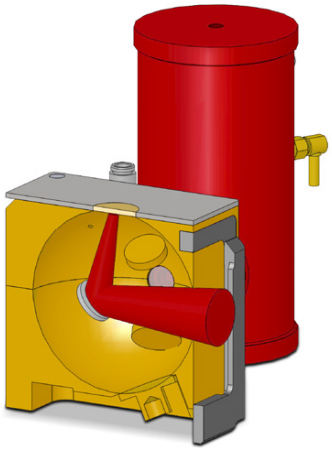

Optical diagram of the upward-looking IntegratIR Sphere.

The downward-looking Mid-IR IntegratIR allows the sample to be placed underneath the sphere. This configuration is desirable for measurements of powders and particulate materials because the incidence beam strikes the sample directly, without passing through an IR transparent window.

For all spheres, the selection of light illumination onto the sample or onto the reference surface is done via a flipper mirror. This allows the background to be collected using either the substitution method or the Taylor method.

Diffuse transmittance of partially transmitting materials can be measured with either sphere. This is done by placing the sample on a standard 2 x 3" sample holder and sliding it in the mount located in front of the transmission port.

Downward-looking IntegratIR

A selection of mercury cadmium telluride (MCT) or deuterated triglycine sulfate (DTGS) detectors is offered with the IntegratIR spheres. This allows the accessory to be optimized for the application and sample type. The wide-band MCT is the commonly configured detector while the less sensitive DTGS is an option for users who require the convenience of a room temperature detector. The MCT detector is approximately 50 times more sensitive compared to the DTGS detector. The accessory comes with built-in detector electronics and interfaces with most FTIR spectrometers. All detectors are pinned in place and interchangeable. For those with both mid- and near-IR spectral capabilities on the FTIR spectrometer an InGaAs detector may be purchased for sensitive NIR diffuse reflection or transmission measurements.

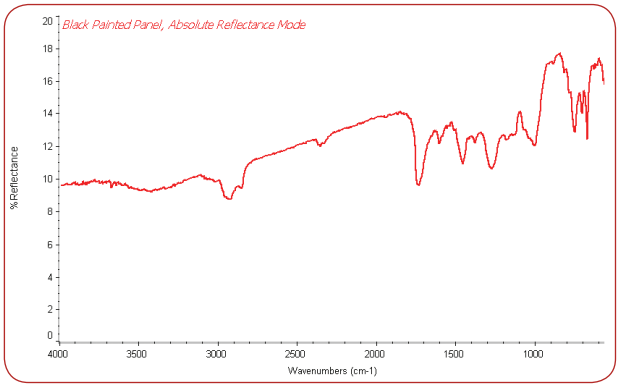

Absolute reflectance spectrum of a painted black panel measured using the PIKE Mid-IR IntegratIR.

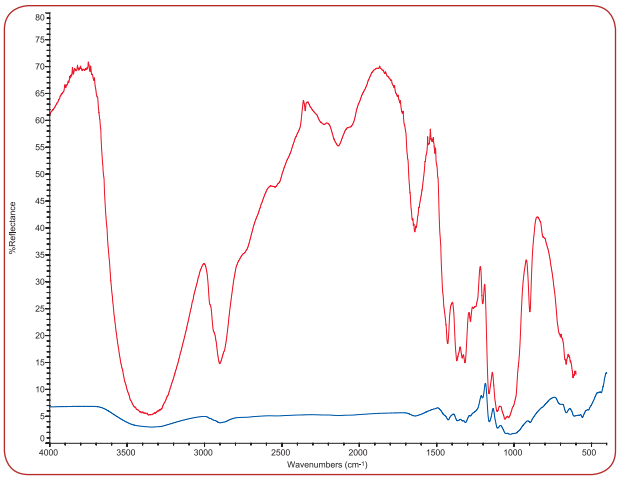

Comparison of transmission spectrum of paper collected using an integrating sphere (red) or in transmission mode without a sphere (blue).

Specifications

Optical Design	Upward- or downward-looking sample spheres
Angle of Incidence	12 degrees
Sphere Size and Surface	3" (76.2 mm) gold-coated Lambertian surface
Sample Port Size	20 mm
Specular Exclusion Port	Standard
Sphere Dimensions (W x D x H)	159 x 248 x 154 mm (excludes baseplate)
Sample Opening, Downward Sphere (W x D x H)	50.8 x 35.5 x 12.7 mm
Detector Choice	DTGS, MCT or InGaAs
Spectral Range, MCT Detectors	Wide-band: 5000–500 cm^{-1} Mid-band: 5000–650 cm^{-1} Narrow-band: 5000–800 cm^{-1}
Spectral Range, Extended DTGS Detector with CsI Window	5000–250 cm^{-1}
Spectral Range, InGaAs Detector	12,200–3850 cm^{-1}

Ordering Information

Part Number	Description
048-12XX	Mid-Infrared IntegratIR Integrating Sphere Accessory 12-Degree **Upward** Sample Positioning *Includes sphere, purge enclosure and tubing, diffuse gold reference and sample plate with ZnSe window*
048-11XX	Mid-Infrared IntegratIR Integrating Sphere Accessory 12-Degree **Downward** Sample Positioning *Includes sphere, purge enclosure and tubing, one diffuse gold reference and powder sample cup*

Notes: Replace XX with your spectrometer's Instrument Code. Click for List >
Your FTIR spectrometer must be capable of interfacing with an external detector.

Detector Choice for IntegratIR *(must select one)*

Part Number	Description
048-3350	Wide-band MCT Detector
048-3250	Mid-band MCT Detector
048-3150	Narrow-band MCT Detector
048-3450	DTGS Detector with CsI Detector Window
048-3550	InGaAs Detector

Notes: Detector includes preamplifier electronics. MCT detectors require liquid nitrogen for cooling.

Replacement Parts and Sampling Options

Part Number	Description
048-0108	Sample Plate with 20 x 2 mm ZnSe Window for Upward IntegratIR
048-0208	Sample Plate with 20 x 2 mm KBr Window for Upward IntegratIR
048-3000	Diffuse Gold Reference for Upward IntegratIR
048-3001	Diffuse Gold Reference for Downward IntegratIR
048-2020	Powder Sample Cup for Downward IntegratIR
048-2050	Sample Slide for Downward IntegratIR

PIKE
6125 Cottonwood Drive, Madison WI 53719 • (608) 274-2721 • info@piketech.com • www.piketech.com

B.5. Calibration certificate

optris infrared thermometers

Kalibrierzertifikat

Calibration Certificate

WKS 17050007
Zertifikat-Nr.
Certificate No.

Gegenstand *Object*	Infrarotkamera *Infrared Imager*
Typ Type	OPTPI640G7O15T1500
Serien-Nr. Kamera *Serial No. Camera*	17050070
Serien-Nr. Optik *Serial No. Optics*	17050001

Die Kalibrierung erfolgt durch Vergleich des Prüflings mit der Anzeige des Vergleichsgerätes, das durch den Deutschen Kalibrierdienst (DKD) bzw. der Physikalisch-Technischen Bundesanstalt (PTB) kalibriert wurde.

The calibration is performed by comparison with standards which are calibrated by the Deutscher Kalibrierdienst (DKD) or Physikalisch-Technische Bundesanstalt (PTB).

Vergleichsgeräte *Calibrated Standards*	Serien-Nr. *Serial No.*	Kalibrierzeichen *Calibration mark*	Kalibrierdatum *Calibration date*
OPTLS (8-14µm)	70101	73215 PTB 16	2016-06
OPTCTL2MHSF (1,6µm)	10067604	73114 PTB 16	2016-12
Exactus (0,9µm)	EXA2074	73113 PTB 16	2016-12

Die Kalibrierung der Temperaturquellen erfolgt nach ST-CAL[1)], die Kalibrierung des Gerätes nach CT-CAL[1)]. / *The calibration of the temperature sources fulfils ST-CAL[1)], the calibration of the product fulfils CT-CAL[1)].*

Messunsicherheit/*Measurement Uncertainty**) ±0,25°C oder ±0,25% (der jeweils größere Wert gilt)
±0.25°C or ±0.25% (whichever is greater)

Die Messergebnisse sind nur zum Zeitpunkt der Kalibrierung gültig! Alle genannten Anzeigewerte bescheinigen eine Genauigkeit von 2% oder +/-2°C (der jeweils größere Wert gilt) unter diesen Bedingungen. / *Each of the named indicated values certifies an accuracy of 2% or +/-2°C (whichever is greater) under the conditions mentioned here.*

Raumtemperatur/*Ambient Temperature* 26,8°C Messfeld/*measuring field:* 5x5

Emissionsgrad/*Emissivity* 1,0 Position Messfeld/*position measuring field:* 191,144

optris
infrared thermometers

Kalibrierzertifikat

Calibration Certificate

WKS 17050007
Zertifikat-Nr.
Certificate No.

Messergebnisse / *Results*

Temperaturpunkt / temperature point [°C]	Anzeigewert des Gerätes / indicated value of the unit [°C]	Blenden-durchmesser / aperture [mm]	Distanz/ distance [mm]	Temperatur-Bereich / temperature range [°C]	Mess-unsicherheit /uncertainty [°C]
200	200,6	50	1000	200...1500	0,6
500	499,3	50	1000	200...1500	1,8
1200	1197,9	50	1000	200...1500	2,3

*) Messunsicherheit der Kalibrierung
Measurement Uncertainty of calibration

Qualitätssicherung
Quality Control

Datum: 15.05.2017
Date:

Prüfer:
Inspector:

DIN ISO 9001:2008
(Registrier-Nr./ *Registration no.*: 068887 QM08)

[1] Werksnorm/ *Factory standard*

Optris GmbH Ferdinand-Buisson-Str. 14 D-13127 Berlin Tel.: +49(0)30 500197-0
Fax: +49(0)30 500197-10 Email info@optris.de Homepage www.optris.de